Some numerical issues in Chemistry-Transport Models - a comprehensive study with the POLYPHEMUS/POLAIR3D platform *

A. Pourchet, V. Mallet, D. Quelo and B. Sportisse

August 26, 2005

Abstract

We review in this report some numerical issues in Chemistry-Transport Models. We perform a comprehensive study with the POLYPHEMUS/POLAIR3D platform applied to air pollution modeling over Europe.

Introduction

Air Pollution Modeling is based on the so-called Chemistry-Transport Models (CTM in the sequel; [6, 1]). These three-dimensional models solve the Reaction-Diffusion-Advection Partial Differential Equations that describe the time and space evolution of reactive trace species in the atmosphere. They are now widely used for many applications: process study (in order to estimate the role of a given physical process), environmental forecast (similar to weather forecast), impact studies (long-term runs in order to evaluate the impact of different scenarios for emissions), inverse modeling of key parameters (on the basis of the coupling between observational data and model outputs), etc.

These models are characterized by a large dimension (up to hundreds of species), a wide range of spatial and time scales... As a result, the numerical simulation of those models is quite difficult (see [12] or [3]). A certain number of classical numerical issues have already been addressed ([10, 11, 5, 4, 2, 8]), but mostly with simplified gas-phase

*This technical report includes all the tests supporting the article "Numerical issues for Chemistry-Transport Models" submitted to Journal of Computational Physics

mechanisms or in 0D or 1D applications. We want to know if there is really an impact of different numerical strategies in 3D real cases.

The objective of this report is therefore to review numerical issues and to perform an extensive set of numerical tests with the POLYPHEMUS/POLAIR3D platform.

This report is organized as follows. The Chemistry-Transport Model is described in section 1. A CPU evaluation is briefly performed in section 2. The numerical algorithms used for operator splitting, advection and chemical kinetics are also given. We then perform some numerical tests and discuss the results in section 3 for operator splitting, section 4 for chemical kinetics, section 5 for advection algorithms and section 6 for horizontal diffusion.

1 The Chemistry-Transport Model

POLAIR3D is a 3D Eulerian Chemistry-Transport Model (CTM) developed by CEREA in order to solve the Reactive Dispersion Equation (or Chemistry-Transport Equation; [6] for instance) which gives the time and space evolution of some trace gases X_i (whose concentration is c_i) in the atmosphere:

$$\frac{\partial c_i}{\partial t} + \mathrm{div}(V(x,t)c_i) = \mathrm{div}(K_{diff}\nabla c_i) + \chi_i(c, T(x,t), t) + S_i(x,t) \quad (1)$$

where x in $\mathbb{R}^3$ and t are the space and time coordinates, c_i is the vector of concentration for species X_i, $V(x,t)$ is the wind field, $K_{diff}(x,t)$ is the eddy diffusivity matrix, $T(x,t)$ is the temperature field.

$S_i(x,t)$ represent the volumic emissions for species i and χ_i is the chemical production/loss for species i.

This dispersion equation mainly describes three processes:

- Advection by a wind field V:

$$\frac{\partial c_i}{\partial t} + \mathrm{div}(V(x,t)c_i) = 0 \quad (2)$$

- Turbulent diffusion:

$$\frac{\partial c_i}{\partial t} = \mathrm{div}(K_{diff}\nabla c_i) \quad (3)$$

- Chemical reactions:

$$\frac{\partial c_i}{\partial t} = \chi_i(c, T(x,t), t) \quad (4)$$

1.1 Splitting methods

The reactive dispersion equation can be viewed as an evolution equation under the form:

$$\frac{dc}{dt} = \sum_{i=1}^{i=n_p} f_i(c) \tag{5}$$

with a number n_p of processes $f_i(c)$.

At the physical level, these processes are of course coupled and the numerical algorithms should solve the processes simultaneously.

Usually, these processes are not solved in a coupled way, and "decoupling" methods are implemented in practice: the so-called operator splitting method or fractional step method ([3, 10, 8]).

These methods are motivated for at least three reasons:

1. As far as numerics is concerned, the coupled resolution can generate many difficulties. The processes can have different qualitative behaviors and the resulting algorithmic constraints can be difficult to satisfy; in the uncoupled case, one can make the choice of the "optimal" algorithm for each process without worrying about the other processes.
2. In the case of the reactive dispersion models, the reactive term is often characterized by a great complexity and a large dimension. An implication is then often the great dispersion of time scales ranging over several orders of magnitude. Implicit ODEs methods are therefore preferred to explicit ones. If the number of grid cells is n_m and the number of chemical species is n_s, the coupled resolution of the implicit system will lead to a complexity of $O([n_s \times n_m]^3)$.

   In the decoupled case, the implicit approach will only be used for the process with the largest timescales dispersion (the reactive term). Therefore, the complexity will then be $n_m \times O(n_s^3)$.
3. In terms of modularity of the resulting data-processing codes, one may prefer to use an approach implementing only the resolution of process taken independently from each other:

   $$\frac{dc}{dt} = f_i(c)\ ,\ c(0) = c_0 \tag{6}$$

   The codes implement thereafter the sequential resolution of systems such as (6).

   A clear advantage is the great modularity: the addition of a new process does not affect the whole program and is equivalent to adding a new "module" solving a system like (6); a process can thus be recovered or substituted from another team via the incorporation of the regarded module, etc.

Hence, splitting allows us to break down a complicated problem into smaller parts for the sake of time stepping, so that the different parts can be solved efficiently with suitable integration formulas. However, this method introduces errors (the so-called splitting errors) to be minimized.

Many algorithms are available in this framework. A and B are two linear operators. c_n is the current value of the solution at time $t_n = n\Delta t$ where Δt is the so-called splitting time step. The splitting algorithm computes an estimation c_{n+1} of the solution $c(\Delta t)$ at time $t_{n+1} = t_n + \Delta t$.

$$\frac{dc}{dt} = Ac + Bc\ ,\ c(0) = c_n \tag{7}$$

First-order method

In order to solve this problem, we follow two steps:

1. Step 1 - integration of process A:

$$\frac{dc^*}{dt} = Ac^* \text{ over } [0, \Delta t]\ ,\ c^*(0) = c_n \tag{8}$$

2. Step 2 - integration of process B:

$$\frac{dc^{**}}{dt} = Bc^{**} \text{ over } [0, \Delta t]\ ,\ c^{**}(0) = c^*(\Delta t) \tag{9}$$

$c^{**}(\Delta t)$ is then an approximation of c_{n+1}. Of course, if the two operators A and B commute, the splitting error will be equal to zero.

Second-order method

1. Step 1 - integration of process B over $[0, \Delta t/2]$:

$$\frac{dc^*}{dt} = Bc^* \text{ over } [0, \frac{\Delta t}{2}]\ ,\ c^*(0) = c_n \tag{10}$$

2. Step 2 - integration of process A over $[0, \Delta t]$:

$$\frac{dc^{**}}{dt} = Ac^{**} \text{ over } [0, \Delta t]\ ,\ c^{**}(0) = c^*(\frac{\Delta t}{2}) \tag{11}$$

3. Step 3 - integration of process B over $[\Delta t/2, \Delta t]$:

$$\frac{dc^{***}}{dt} = Bc^{***} \text{ over } [0, \frac{\Delta t}{2}]\ ,\ c^{***}(0) = c^{**}(\Delta t) \tag{12}$$

$c^{***}(\frac{\Delta t}{2})$ is then an approximation of c_{n+1}.

Source-splitting method

1. Step 1 - integration of process A:

$$\frac{dc^*}{dt} = Ac^* \text{ over } [0, \Delta t]\,,\ c^*(0) = c_n \tag{13}$$

2. Step 2 - integration of process B while taking into account a source term defined by step 1:

$$\frac{dc^{**}}{dt} = Bc^{**} + \frac{c(\Delta t) - c_n}{\Delta t} \text{ over } [0, \Delta t]\,,\ c^{**}(0) = c_n \tag{14}$$

$c^{**}(\Delta t)$ is then an approximation of c_{n+1}. This method is a first-order one. The advantage is that the initial condition of the second step is not modified. Therefore, if c_n had reached a stable state, it is not disturbed. This is the reference method in POLAIR3D.

Approximate Matrix Factorization Method (AMF)

If an implicit scheme is used for the resolution of (7), we get (for instance for Backward Euler):

$$\frac{c_{n+1} - c_n}{\Delta t} = Ac_{n+1} + Bc_{n+1} \tag{15}$$

leading to $(I - (A + B)\Delta t)c_{n+1} = c_n$. With the approximation:

$$I - (A + B)\Delta t \sim (I - A\Delta t)(I - B\Delta t) + O(\Delta t^2) \tag{16}$$

we have to solve successively:

$$(I - A\Delta t)c^* = c_n \tag{17}$$

and

$$(I - B\Delta t)c^{**} = c^* \tag{18}$$

1.2 Integration of chemical kinetics

Since chemistry often consumes the largest part of the CPU time, efficiency in terms of CPU time is a key property for chemistry solvers. This can be accomplished by using large timesteps, but this is only possible if the method has good stability properties.

Chemical reactions are described by:

$$\frac{dc_i}{dt} = \chi_i(c, T(x, t), t). \tag{19}$$

We suppose that the chemical mechanism is described by a set of n_r reactions among n_s species. For a species X_i, the chemical source term is:

$$\chi_i(c, T(x,t), t) = \sum_{j=1}^{j=n_r} S_{ij}\omega_j(c, T, L, I) \tag{20}$$

with S the stoichiometric matrix $(n_s * n_r)$ and ω_j the reaction rate for reaction j. Due to Mass Action Law, the reaction rate of reaction j is:

$$\omega_j = k_j \prod_{i=1}^{i=n_s} c_i^{S_{ij}} \tag{21}$$

where k_j is the kinetic rate to be computed. The resulting system of ordinary differential equations (ODE) can be written under the form:

$$\frac{dc}{dt} = f(c,t),\ c(0) = c_0,\ c \in \mathbb{R}^p \tag{22}$$

The scheme used in POLAIR3D is a second-order Rosenbrock (ROS2) method (see [11]) for the integration of the ODE. The scheme reads as:

$$c_{n+1} = c_n + (3k_1 + k_2)\frac{\Delta t}{2} \tag{23}$$

where

$$\left\{ \begin{array}{lcl} (1 - \gamma \Delta t A)k_1 & = & f(t_n, c_n) \\ (1 - \gamma \Delta t A)k_2 & = & f(t_{n+1}, c_n + \Delta t k_1) - 2k_1 \end{array} \right. \tag{24}$$

$\gamma = 1+1/\sqrt{2}$ and A denotes an approximation of the Jacobian matrix $A \simeq \partial f/\partial c$.

The stability function R is computed with the linearized source term $f(c,t) = -k(t) \cdot c$. We refer to the appendix for more details. The result is:

$$R(k_n \Delta t) = \frac{c_{n+1}}{c_n} = \frac{(2\gamma^2 - (3+\beta)\gamma + \beta)\lambda^2 + (4\gamma - 1 - \beta)\lambda + 2}{2(1+\gamma\lambda)^2} \tag{25}$$

with $\beta = \frac{k_{n+1}}{k_n}$.

1.3 Advection algorithms

The advection by wind $\mathbf{V}$ is given by:

$$\frac{\partial c}{\partial t} + \mathrm{div}(\mathbf{V}c) = 0. \tag{26}$$

If u, v et w are the wind velocities along directions x, y and z, one gets:

$$\frac{\partial c}{\partial t} + \frac{\partial (uc)}{\partial x} + \frac{\partial (vc)}{\partial y} + \frac{\partial (wc)}{\partial z} = 0 \tag{27}$$

For the 1D advection equation

$$\frac{\partial c}{\partial t} + \frac{\partial (uc)}{\partial x} = 0, \tag{28}$$

the conservative form of numerical schemes is:

$$c_i^{n+1} = c_i^n + F_{i-\frac{1}{2}}^n - F_{i+\frac{1}{2}}^n, \tag{29}$$

where c_i^n approximates the value of c at time $t_n = n\Delta t$ in the cell of bounds $x_{i-\frac{1}{2}} = (i - \frac{1}{2})\Delta x$ and $x_{i+\frac{1}{2}} = (i + \frac{1}{2})\Delta x$. $F_{i-\frac{1}{2}}^n$ and $F_{i+\frac{1}{2}}^n$ represent the inflow and outflow fluxes at the cell boundaries.

As a reference, POLAIR3D uses a third-order Direct Spatial Time scheme (DST), with a Sweby-type flux limiter ([10]). Let

$$d_0(\nu) = \frac{1}{6}(2 - \nu)(1 - \nu), \;\; d_1(\nu) = \frac{1}{6}(1 - \nu^2) \tag{30}$$

and

$$\theta_i = \frac{c_i - c_{i-1}}{c_{i+1} - c_i}. \tag{31}$$

The limiter function is

$$\psi(\nu, \theta) = \max\left(0, \min\left(1, d_0(\nu) + d_1(\nu)\theta, \frac{1 - \nu}{\nu}\theta\right)\right). \tag{32}$$

Then, $F_{i+\frac{1}{2}}$ is given by:

$$F_{i+\frac{1}{2}} = \begin{cases} \nu_{i+\frac{1}{2}} \left(c_i + \psi \left(\nu_{i+\frac{1}{2}}, \theta_i \right) (c_{i+1} - c_i) \right) & \text{if } u_{i+\frac{1}{2}} \geq 0 \\ -\nu_{i+\frac{1}{2}} \left(c_{i+1} + \psi \left(\nu_{i+\frac{1}{2}}, \frac{1}{\theta_{i+1}} \right) (c_i - c_{i+1}) \right) & \text{if } u_{i+\frac{1}{2}} < 0 \end{cases} \tag{33}$$

with $\nu_{i+\frac{1}{2}} = \left| u_{i+\frac{1}{2}} \right| \frac{\Delta t}{\Delta x}$ the CFL number.

For this scheme, the CFL condition is $\nu_{i+\frac{1}{2}} \leq 1$.

1.4 Turbulent diffusion

In the atmosphere, the molecular diffusion can be neglected. The diffusion term is actually related to a parameterization of turbulence (due to the widespread of spatial and time scales). We suppose that the fields can be splitted as:

$$\Psi = \langle \Psi \rangle + \Psi' \tag{34}$$

with $\langle \Psi \rangle$ an averaged quantity and Ψ' a fluctuation. The operator $\langle \rangle$ commutes with differential operators, and $\langle \Psi' \rangle = 0$.

The key point is to parameterize vertical turbulent fluxes. When applied to the concentration c_i, one gets

$$\langle c_i' V' \rangle \simeq -K_{diff} \nabla \langle c_i \rangle. \tag{35}$$

With $c_i = \rho m_i$, m_i being the mass fraction and ρ the density, the following approximation is usually made:

$$c_i' V' = \langle \rho \rangle m_i' V' + \langle m_i \rangle \rho' V' \simeq \langle \rho \rangle m_i' V'. \tag{36}$$

If the parameterization 35 is applied to m_i, we get:

$$\langle c_i' V' \rangle = -\langle \rho \rangle K_{diff} \nabla \frac{\langle c_i \rangle}{\langle \rho \rangle}. \tag{37}$$

Eq. 35 and 37 are two possible parameterizations for turbulent diffusion. As the averaged continuity equation is usually written:

$$\frac{\partial \langle \rho \rangle}{\partial t} + \mathrm{div}(\langle \rho \rangle \langle V \rangle) = 0 \tag{38}$$

it seems more coherent to apply the parameterization to the mass fraction. However, we can also suppose that air density does not vary a lot. We want to investigate the sensitivity to this choice of parameterization.

As a reference, POLAIR3D uses the c_i parameterization. POLAIR3D is based on the hypothesis that the horizontal part of K_{diff} be represented by $K_H \cdot I$ (the diffusion is isotropic and constant), I being the 2×2 identity matrix, where K_H is a scalar value to be chosen. Therefore, the horizontal diffusion is now modelized by:

$$\frac{\partial c_i}{\partial t} = \mathrm{div}(K_H \nabla_{x,y} c_i) \tag{39}$$

In our case, the reference value for K_H is 50000 $m^2 \cdot s^{-1}$ at continental scale. For the vertical part, K_Z is given by classical parameterization.

1.5 Analysis procedure

In order to evaluate the impact of numerics we have chosen to perform model-to-model comparisons. The reference configuration of POLAIR3D, is described below in more details.

POLAIR3D uses as a reference chemical mechanism the RACM mechanism ([9]) with 72 species. The timestep is 600 seconds. The reference splitting method is a source splitting method with boundary conditions taken into account in the diffusion. ROS2 is the scheme for time integration of chemical kinetics and diffusion; it is solved with $\gamma = 1 + \frac{\sqrt{(2)}}{2}$. The advection scheme is a third-order Direct Space

Time scheme with a Sweby-type flux limiter. Besides, the advection is solved without directional splitting. Finally, the diffusion is solved with a K_H taken equal to 50 000 $m^2 \cdot s^{-1}$ with a c_i parameterization. We assess thereafter for each issue the spread in the results due to other numerical choices.

As far as the results are concerned, for most tests, the species looked at are O_3, NO, NO_2, SO_2 and HO. Indeed, some of those species are slow whereas others are fast. We look at statistical values of concentrations for analysis (see appendix for definition) : minimum value, maximum value (most of the time, only the maximum value appears, as the minimum value os to small), mean value, standard deviation. We look both at spatial values and temporal values in order to see how species are distributed over the domain and how they evolve with time.

We also look at Probability Density Functions (PDF) of of the error between two simulations. Finally, a good indicator is the percentage of concentrations that show less than 5% of difference. This number is given on the PDF figures for each species.

2 CPU evaluation

Polair3D typical CPU time (PIV, 2.4 Gz) is about 5 minutes for a daily prevision at continental scale for the reference configuration. Time may be a stake for some applications. For example, in case of impact studies, the key point is to evaluate the influence of different scenarios (emission reductions) on air quality. In practice, the matter is to run simulations over several years and for numerous scenarios. In this case, computation time can easily reach several days.

In order to optimize Polair3D computation time, different levels can be investigated:

- the size of the system: number of grid cells (fineness of discretization) or number of species (simplified mechanism);
- the computer implementation;
- the numerical schemes used to solve the equation describing the physical processes (especially advection, diffusion and chemistry). We have to find a compromise between accuracy, stability and CPU requirements.

We want to find out how long Polair3D spends in each process, for typical configurations: a continental study over Europe, and a regional one over Lille. This will tell about the efficiency of the program, and reveal which functions to optimize.

Kcachegrind (`http://kcachegrind.sourceforge.net/cgi-bin/show.cgi/KcacheGrindIndex/`) is a profiling data visualization tool

that gives us these indications. POLAIR3D is compiled with ifort and the compilation options -O3 -g -axW -w -cm -assume byterecl.

2.1 Continental study

The program is runned with 7 iterations and with Kcachegrind.

Description of the domain

The study is held over Europe, between the meridians 10.25W and 21.75E, and the parallels 40.25N and 56.75N (as shown in figure 1) , during summer 2001.

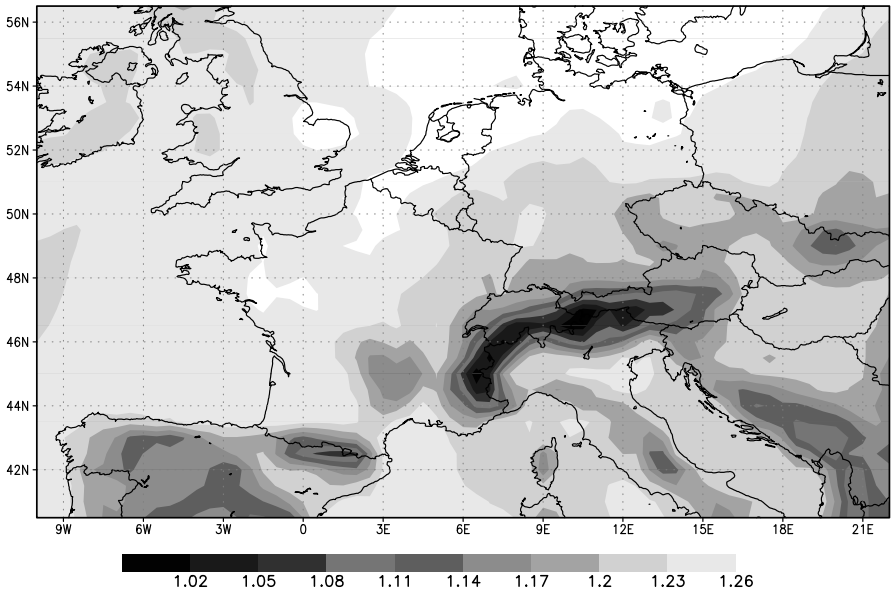

Figure 1: Air density on the domain

The domain is divided into:

- 65 grid cells along x;
- 33 grid cells along y;
- 5 grid cells along z.

Results

We get the following proportions (total is not exactly 100% because a part of the time is spent on initialization functions or post-treatment):

- 58.6% of the time is spent in chemistry;
- 15.2% in advection;
- 22% in diffusion (6,65% in diffusion along x; 6,75% in diffusion along y; 8,6% in diffusion along z.)

Figures 2–4 show how time is shared more precisely within each process (the figure 3 is representative of the diffusion along the 3 directions).

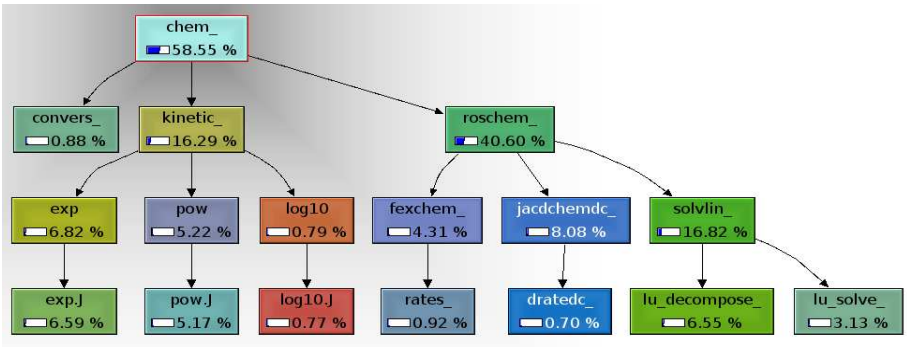

Figure 2: Distribution inside chemistry for the continental case.

- `convers` makes unit conversions for gas-phase concentrations and volumic emissions from $\mu g \cdot m^{-3}$ to $mol \cdot cm^{-3}$ (and vice versa);
- `kinetic` computes the kinetic rates;
- `roschem` computes one timestep for the gas-phase chemistry in one grid cell using the second-order Rosenbrock method (the linear systems to be solved are optimized);
- `jacdchemdc` computes the Jacobian matrix for the gas-phase;
- `solvlin` solves Ax = b where A is an input matrix and b is an input vector.

Chemistry takes the most time here. Indeed, we can see in figure 2 that the chemistry calls upon two functions: `kinetic` and `roschem`. The function `kinetic` computes the kinetic constants of the chemical scheme using power and exponential functions, which explains its importance in terms of CPU time (approximately 16%). As for the function `roschem`, it solves a system, which is also costly (the LU decomposition takes 16,8%).

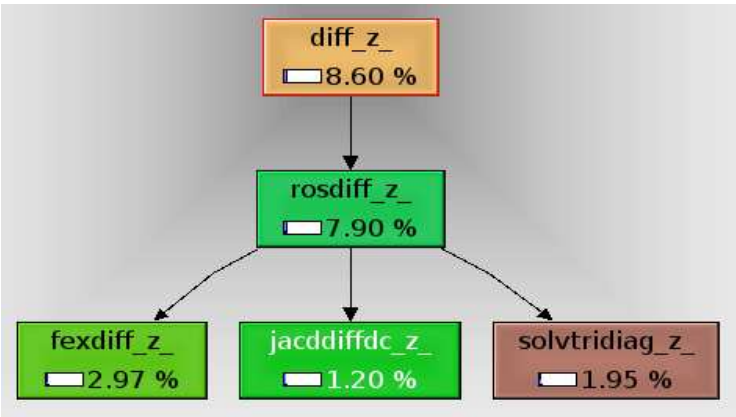

Figure 3: Distribution inside diffusion along z for the continental case.

- `rosdiff` solves diffusion along z for one timestep using a second-order Rosenbrock as numerical scheme;
- `fexdiff` computes $div\left(K_z \frac{\partial c}{\partial z}\right)$ with a three point scheme;
- `jacddiffdc` computes the Jacobian matrix of the diffusion scheme;
- `solvtridiag` solves Mx = b where M is an input tridiagonal matrix and b is an input vector.

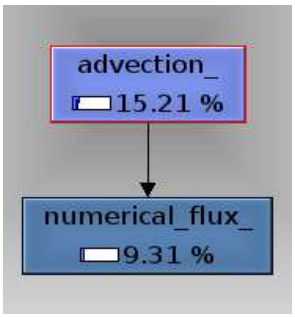

Figure 4: Distribution inside advection for the continental case.

- `advection` solves advection along x, y and z for one timestep;
- `numerical_flux` computes the numerical flux between two cells. It uses a third-order upwind-biased scheme with a Sweby-type flux limiter as described earlier.

2.2 Regional study

Description of the domain

The study takes place around Lille, with 1km × 1km cells.

The domain is divided into:

- 42 grid cells along x;
- 44 grid cells along y;
- 9 grid cells along z.

The grid cells are smaller. That leads us to take a smaller timestep due to the CFL condition. We can thus expect to have different results from the continental scale ones.

Results

We get the following proportions for CPU time:

- 10,2% in chemistry;
- 83,8% in advection;
- 4,8% in diffusion (1,3% in diffusion along x; 1,4% in diffusion along y; 2,1% in diffusion along z.)

Figures 5 and 6 show how time is shared within each process.

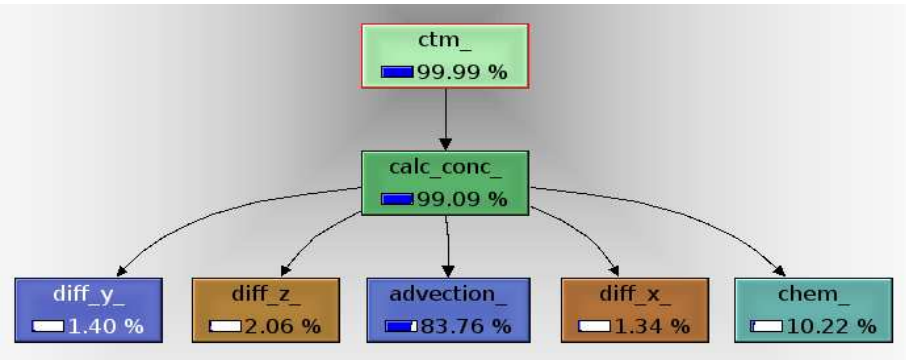

Figure 5: General distribution for the regional case

We can see in figure 5 the importance of advection, which supplants all the other functions. Indeed, the necessity to meet the *Courant-Friedrich-Lewy restriction* (CFL restriction):

$$\frac{V\Delta t}{\Delta x} \leq 1 \tag{40}$$

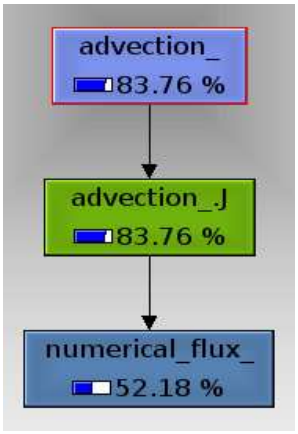

Figure 6: Distribution inside advection for the regional case

leads us to a small timestep (since the grid cells are small).

In particular, the figure 6 indicates that the function calculating the numerical flux takes 52% of total time. It is very significant to control the number of calls to this function.

First, we can investigate the impact of a change of advection scheme on the distribution of times. The advection scheme used in the code is a third-order DST (Direct Space Time) scheme with a flux limiter. The flux limiter can be a factor of complexity of the code. We will therefore test POLAIR3D with a third-order scheme without flux limiter and with a simple upwind scheme.

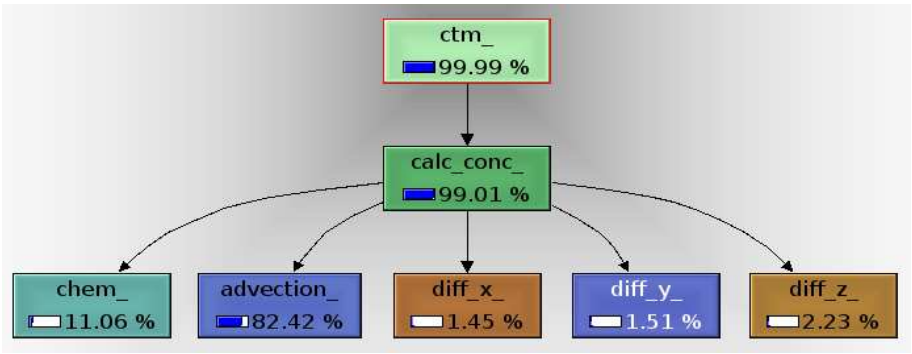

Figure 7: General distribution in the regional case with a third-order scheme without flux limiter

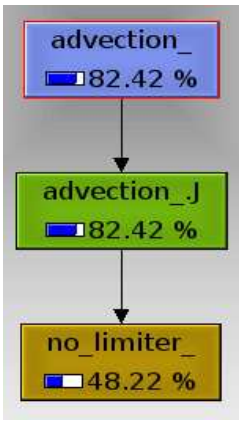

Figure 8: Distribution within advection in the regional case with a third-order scheme without flux limiter

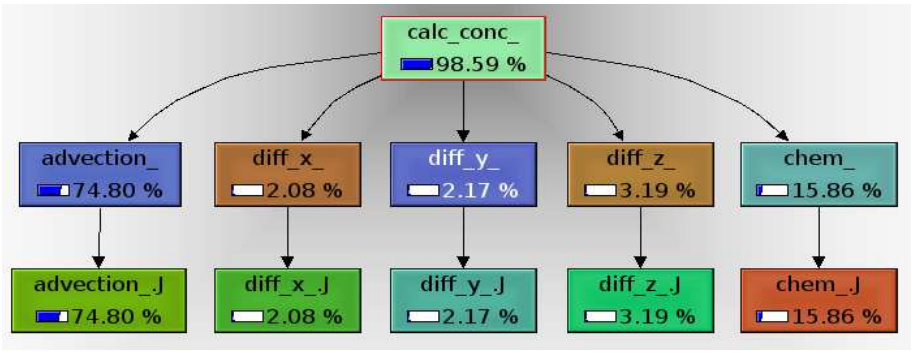

Figure 9: General distribution in the regional case with an upwind scheme

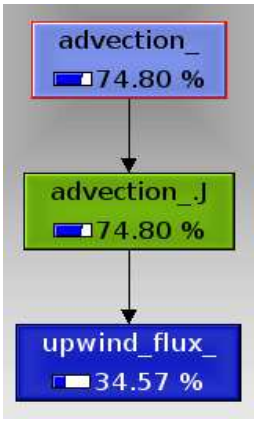

Figure 10: Distribution within advection in the regional case with an upwind scheme

The figures 7–10 indicate that the advection scheme has an impact in the distribution of times, especially for a regional simulation. For a continental simulation, a change of advection scheme does not influence excessively the CPU time; indeed, after 1008 iterations, the code using an upwind scheme gains only 35 seconds in computing time over a code using a third-order scheme with flux limiter.

On the other hand, the choice of the advection scheme is the crucial point with a regional simulation. For a simulation with only 24 iterations (that is to say over 4 hours), the computing times according to the advection schemes are as follows (see table 1):

- for a third-order DST scheme with a flux limiter: 294 seconds;
- for a third-order DST scheme without flux limiter: 276 seconds;
- for an upwind scheme: 217 seconds.

The results are summarized in Table 1:

	Upwind scheme	third-order without flux limiter	third-order with flux limiter
Total CPU time	217 seconds	276 seconds	294 seconds
CPU time for advection	162 seconds (74,80%)	227 seconds (82,42%)	246 seconds (83,76%)
CPU time for flux computation	75 seconds (34,57%)	133 seconds (48,22%)	153 seconds (52,18%)

Table 1: Comparison between CPU time needed for advection

2.3 Conclusion

The main results to remember are:

- for a continental simulation, solving chemistry requires the largest CPU time. This is due to exponential and power functions and to the need to solve linear systems (LU decomposition).
- for a regional simulation, the CPU related to advection becomes much more important than for the other processes, mainly because of the flux limiter.

3 Splitting methods

The objective of this section is to investigate the sensitivity to the splitting timestep to the scheme order and to the sequence. Besides, the boundary conditions (deposition and surface emissions) can be included in different processes and it may have an influence.

3.1 Splitting Timestep

The splitting timestep is important in terms of accuracy and stability. Indeed, as the splitting error is a power of Δt, the smaller the timestep is, the more precise the result should be. However, a small splitting timestep has a cost, due to the high number of iterations. On the other hand, a larger timestep may involve instability for some processes.

We test the influence of the splitting timestep on a continental simulation over one day with a source splitting. We test the accuracy brought by a time step of 0,6 seconds (144 000 iterations, which takes almost 4 days) compared to 6, 60 and 600 seconds (for a timestep of 600 seconds, 144 iterations are needed, and 7 minutes to run the simulation).

Figures 11–13 clearly indicate that the timestep does not have a strong influence on the results. When $\Delta t = 6$ seconds, 60 seconds or 600 seconds, the results are hardly discernible. Only the case with $\Delta t = 0{,}6$ seconds can be distinguished, but the difference is not so important. At least, such a difference does not justify the cost in terms of time spent on the simulation.

In order to make sure that the fact that we look at statistical values does not "hide" anything, we also look at the time evolution of the concentrations over Paris (which is a very polluted area; figure 15), and over Pontarlier (which is less polluted; figure 16). There does not seem to be a difference between the results obtained with differnt timesteps, even when we look on several stations.

In order to test the stability, we run the same simulation with three other timesteps: 1200, 1800 and 3600 seconds. Figures 17 to 19 indicate that a bigger timestep does not bring much instability. However, the spread of results is larger than for previous values.

We can see on figure 21 that plots the time evolution of the concentrations over Paris that NO is very much influenced by the value of Δt. The peak value is much lowered as the timestep increases.

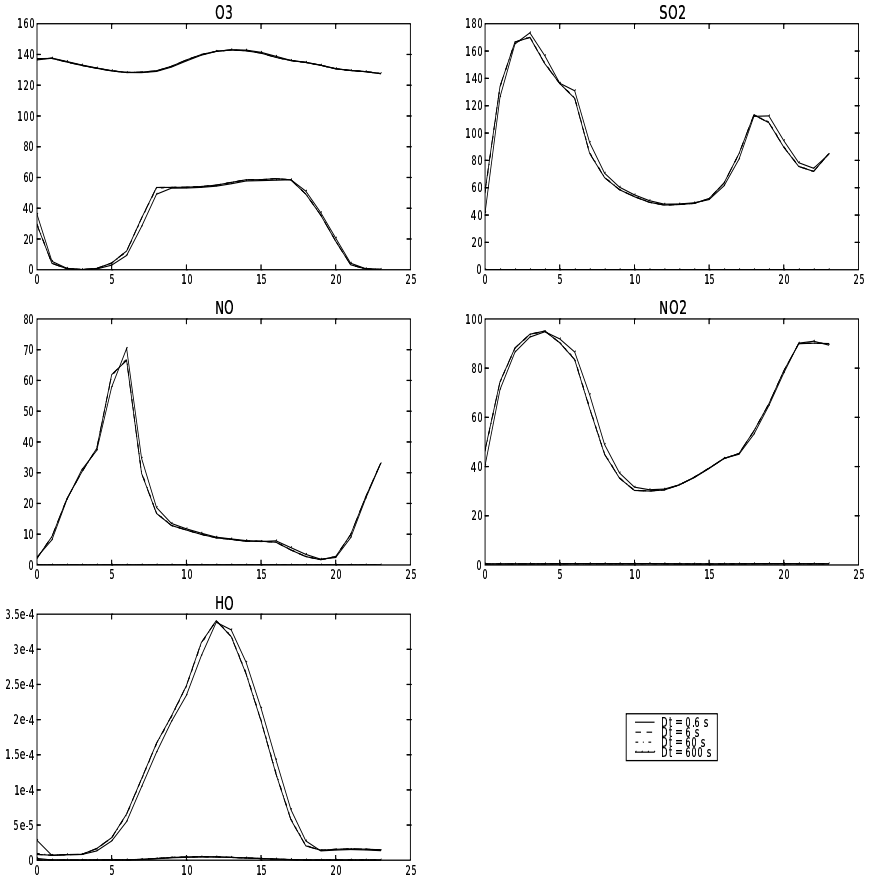

Figure 11: Time evolution of the spatial minimum and maximum ($\mu g \cdot m^{-3}$) for different timesteps: {0.6, 6, 60, 600}

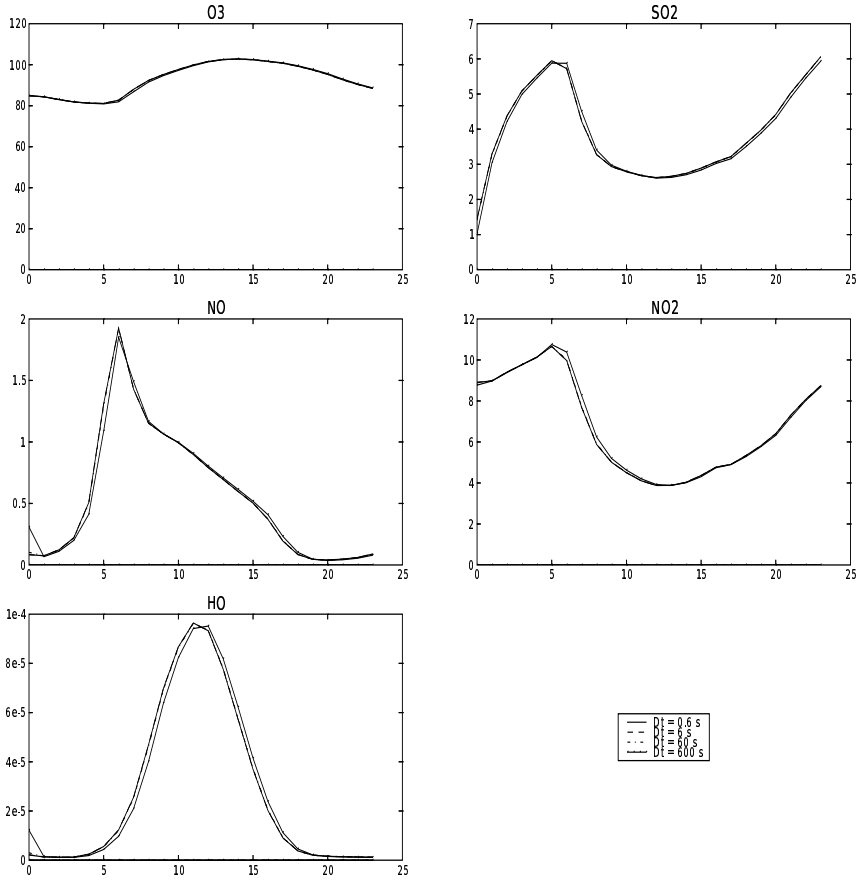

Figure 12: Time evolution of the spatial mean ($\mu g \cdot m^{-3}$) for different timesteps: {0.6, 6, 60, 600}

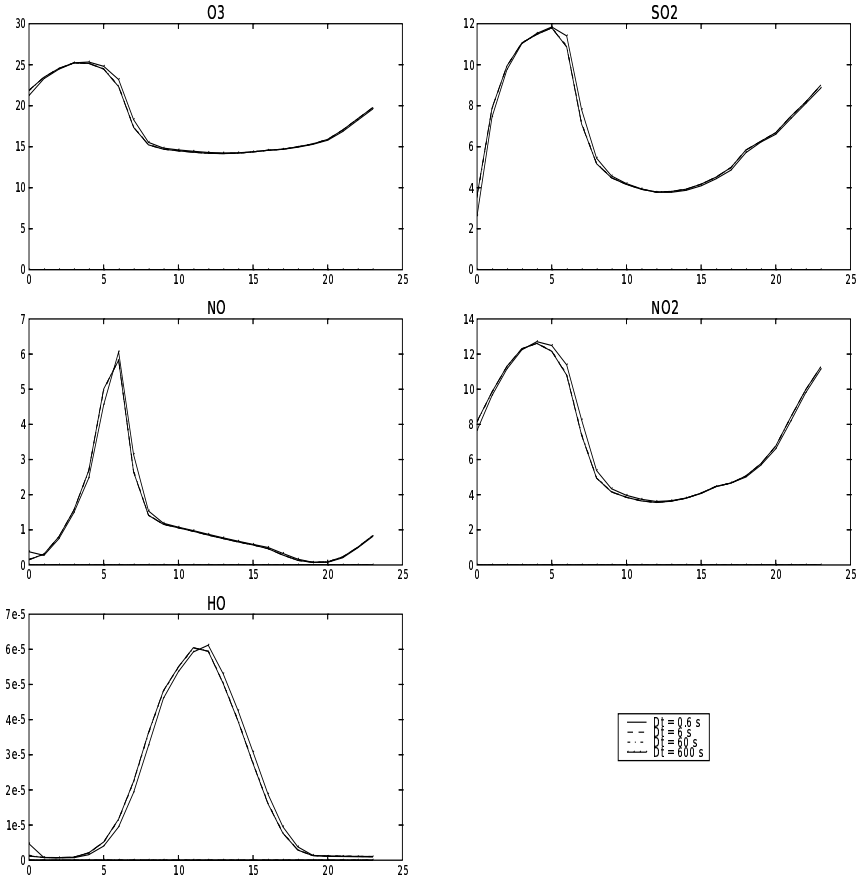

Figure 13: Time evolution of the spatial standard deviation ($\mu g \cdot m^{-3}$) for different timesteps: {0.6, 6, 60, 600}

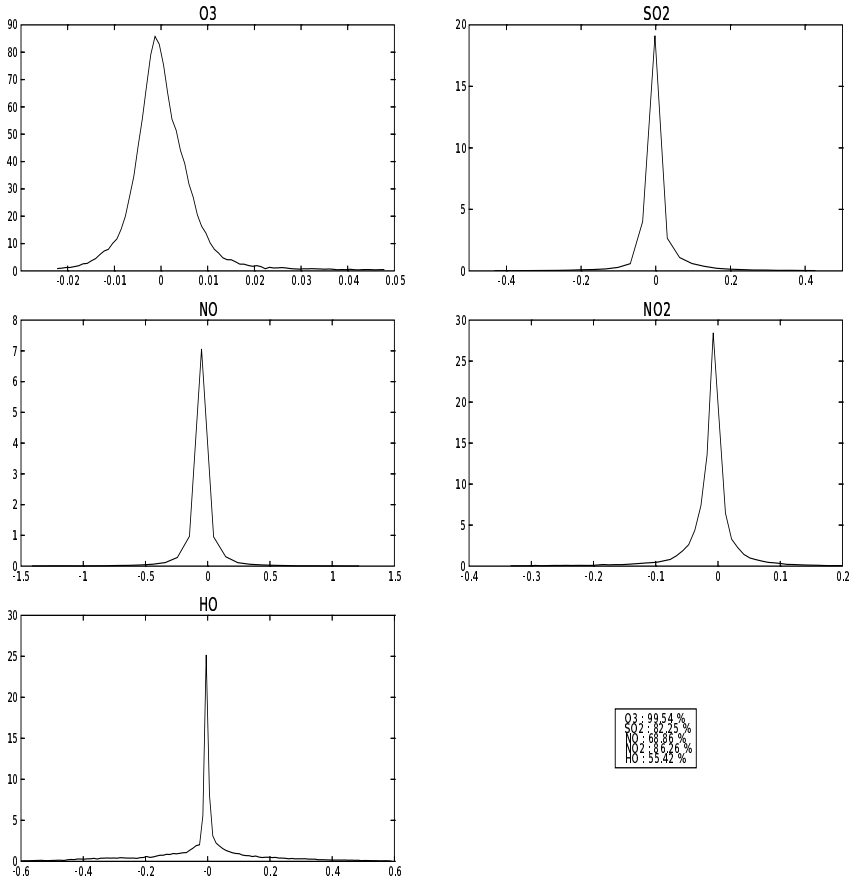

Figure 14: PDF of error between $\Delta t = 0.6$s and $\Delta t = 600$s

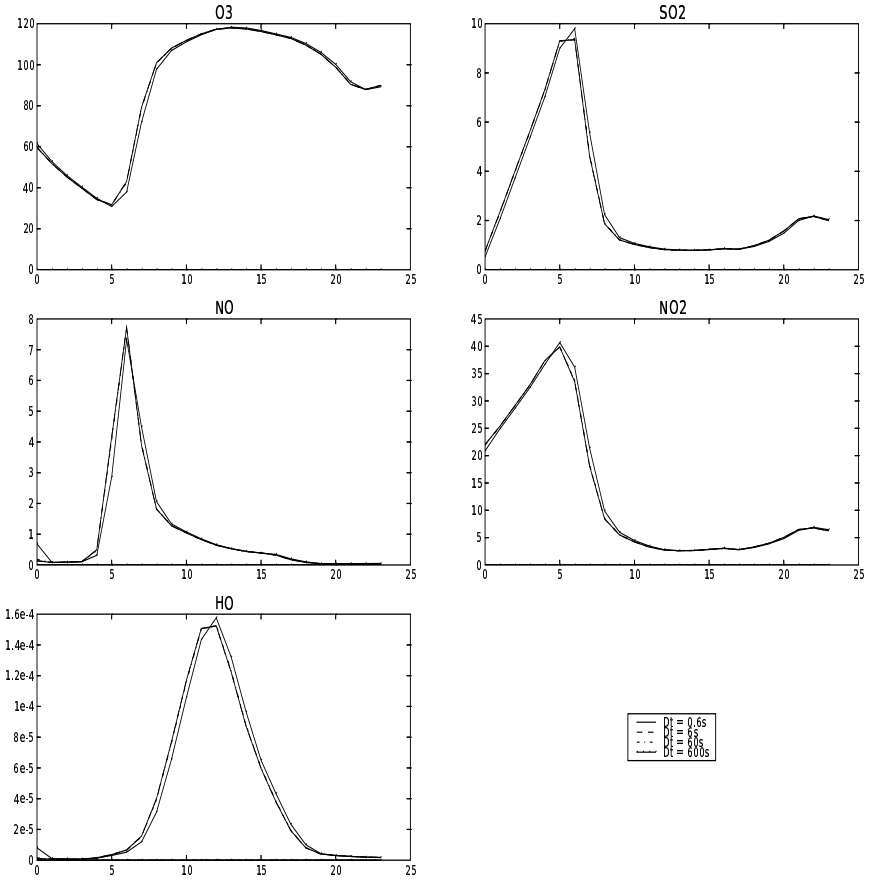

Figure 15: Time evolution of the concentrations ($\mu g \cdot m^{-3}$) over Paris for different timesteps: {0.6, 6, 60, 600}

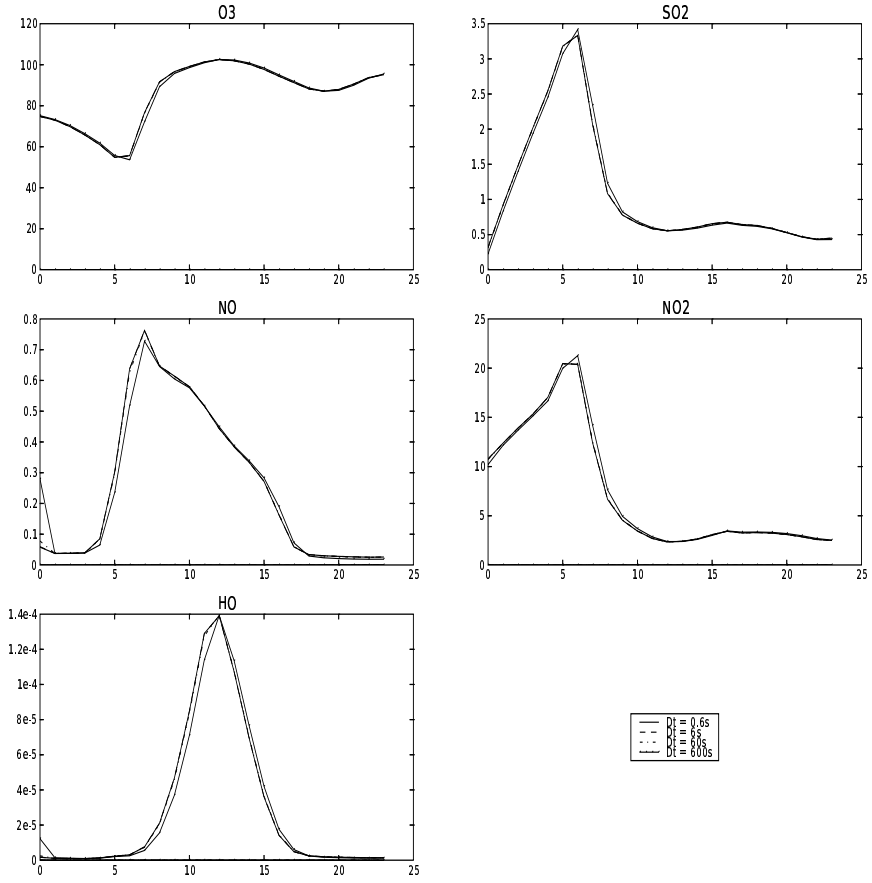

Figure 16: Time evolution of the concentrations ($\mu g \cdot m^{-3}$) over Pontarlier for different timesteps: {0.6, 6, 60, 600}

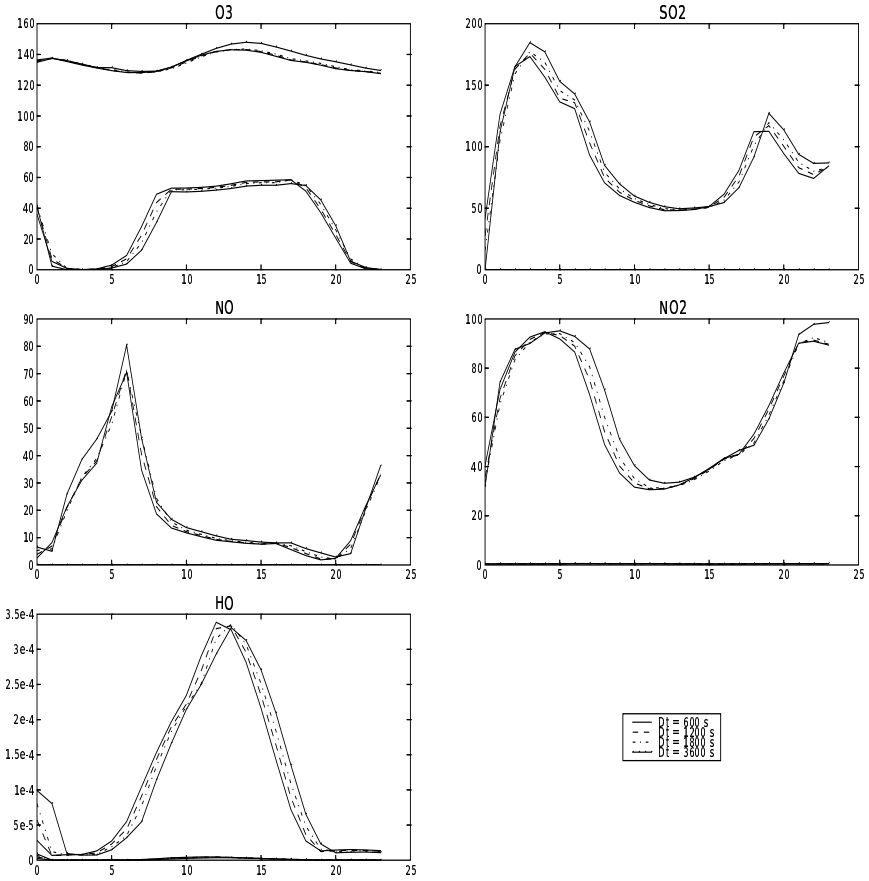

Figure 17: Time evolution of the spatial minimum and maximum ($\mu g \cdot m^{-3}$) for different timesteps: {600, 1200, 1800, 3600}

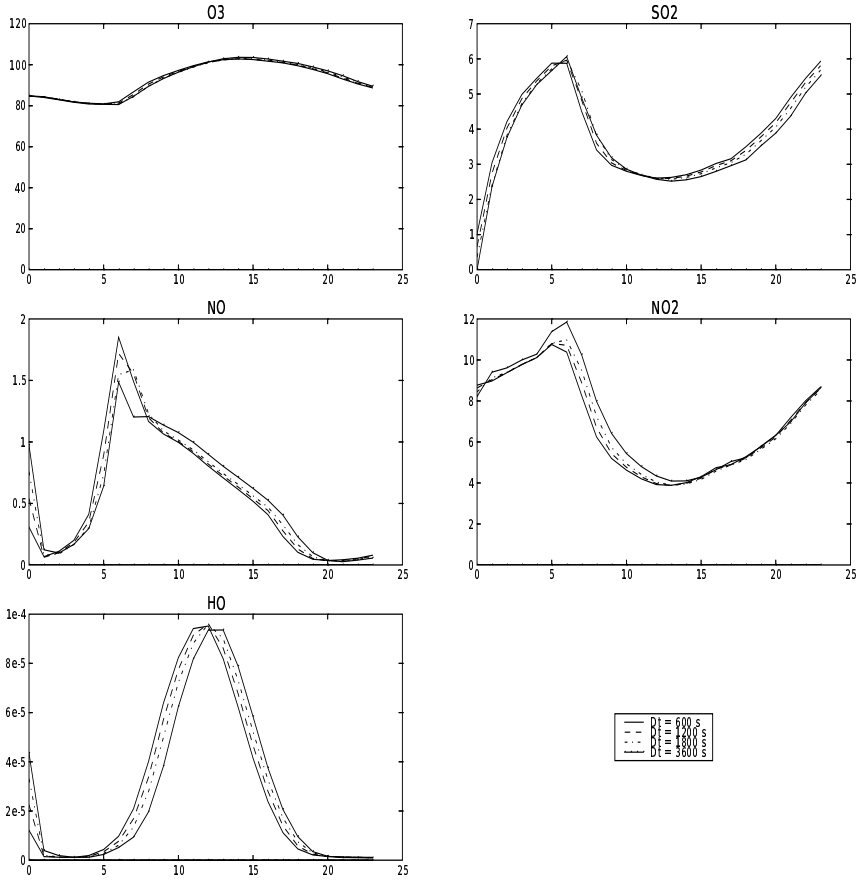

Figure 18: Time evolution of the spatial mean ($\mu g \cdot m^{-3}$) for different timesteps: {600, 1200, 1800, 3600}

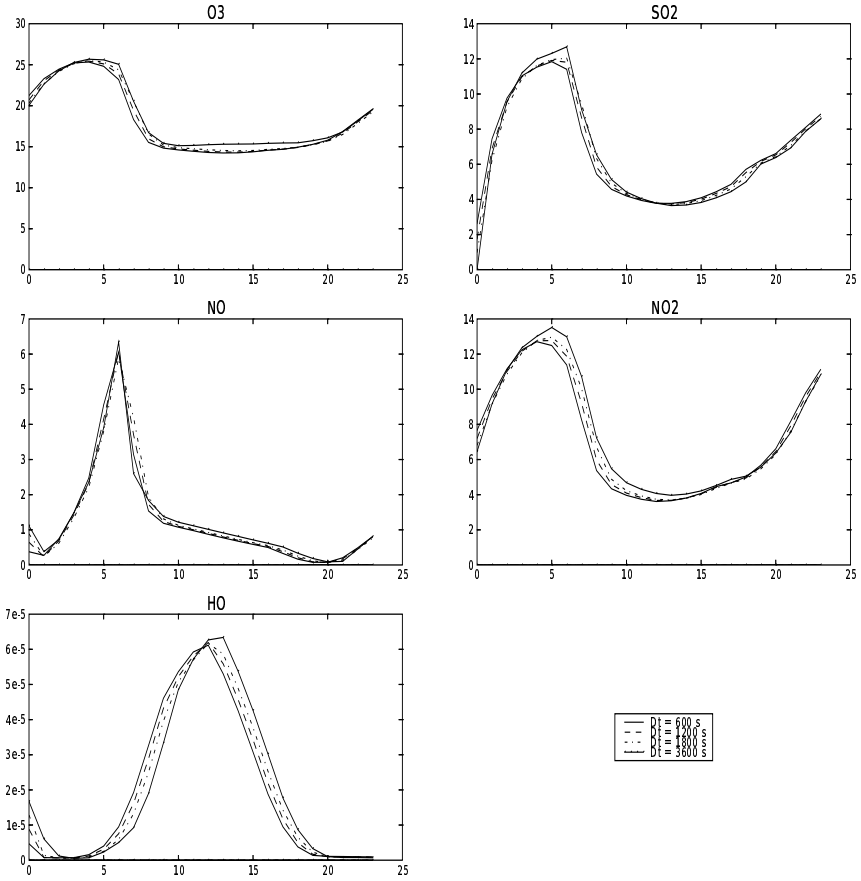

Figure 19: Time evolution of the spatial standard deviation ($\mu g \cdot m^{-3}$) for different timesteps: {600, 1200, 1800, 3600}

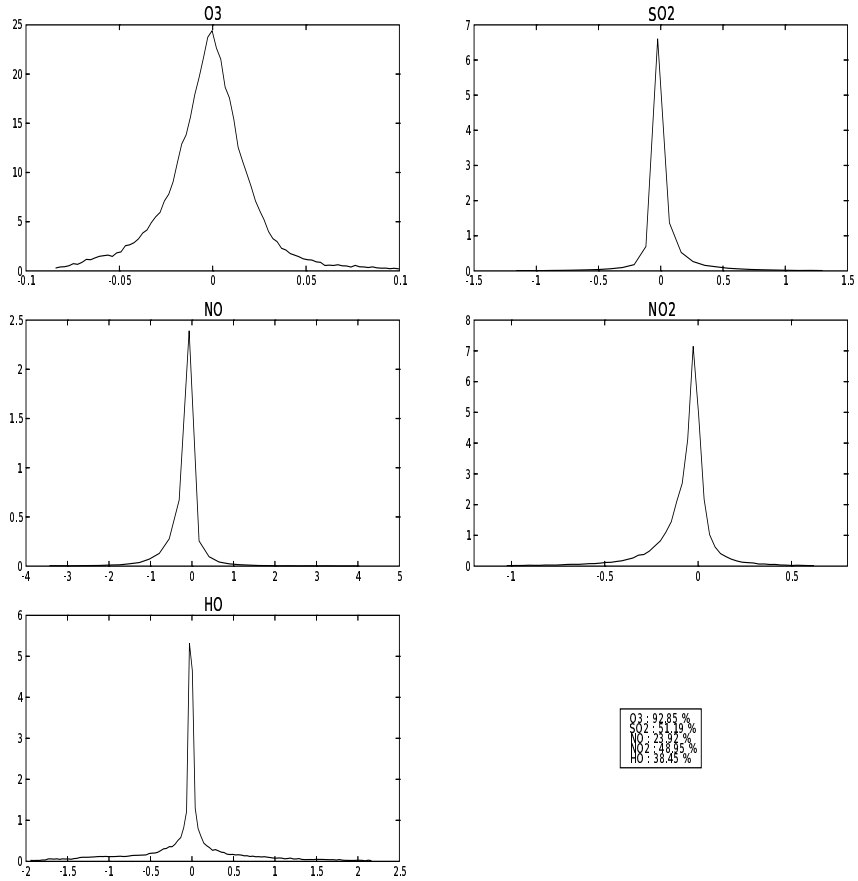

Figure 20: PDF of error between $\Delta t = 0.6$s and $\Delta t = 3600$s

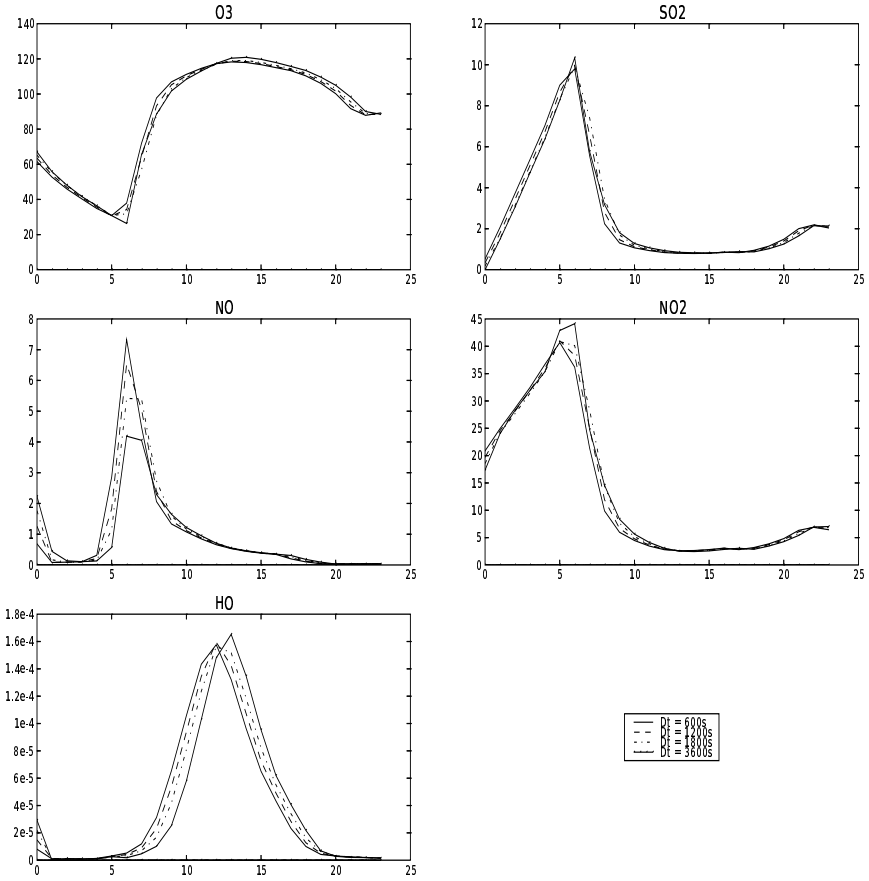

Figure 21: Time evolution of the concentrations ($\mu g \cdot m^{-3}$) over Paris for different timesteps: {600, 1200, 1800, 3600}

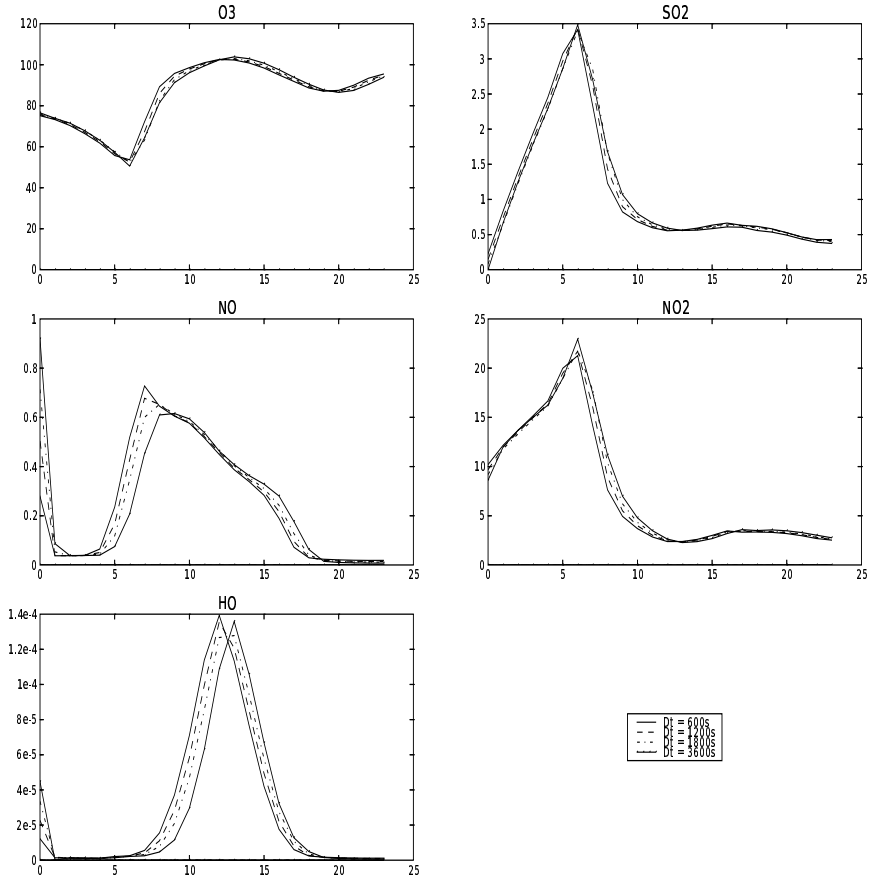

Figure 22: Time evolution of the concentrations ($\mu g \cdot m^{-3}$) over Pontarlier for different timesteps: {600, 1200, 1800, 3600}

3.2 Splitting scheme order

The scheme order is supposed to have an influence on the accuracy of the results. Once again, the key point is to choose the trade-off between the quality of the results and the running complexity. Therefore, we test POLAIR3D on a continental run over one day with different splitting schemes : first-order, second-order, source-splitting, AMF C-D (chemistry, then diffusion) and AMF D-C (diffusion, then chemistry). Besides, we compare the results to the reference run obtained with a timestep of 0,6 second.

According to figures 23–30, it seems that the scheme hardly makes a difference. NO and HO are only different at the beginning of the simulation. Thereafter, the concentrations are the same ones whatever the scheme is.

The first-order scheme and the source splitting are, as expected, the fastest ones in terms of CPU time.

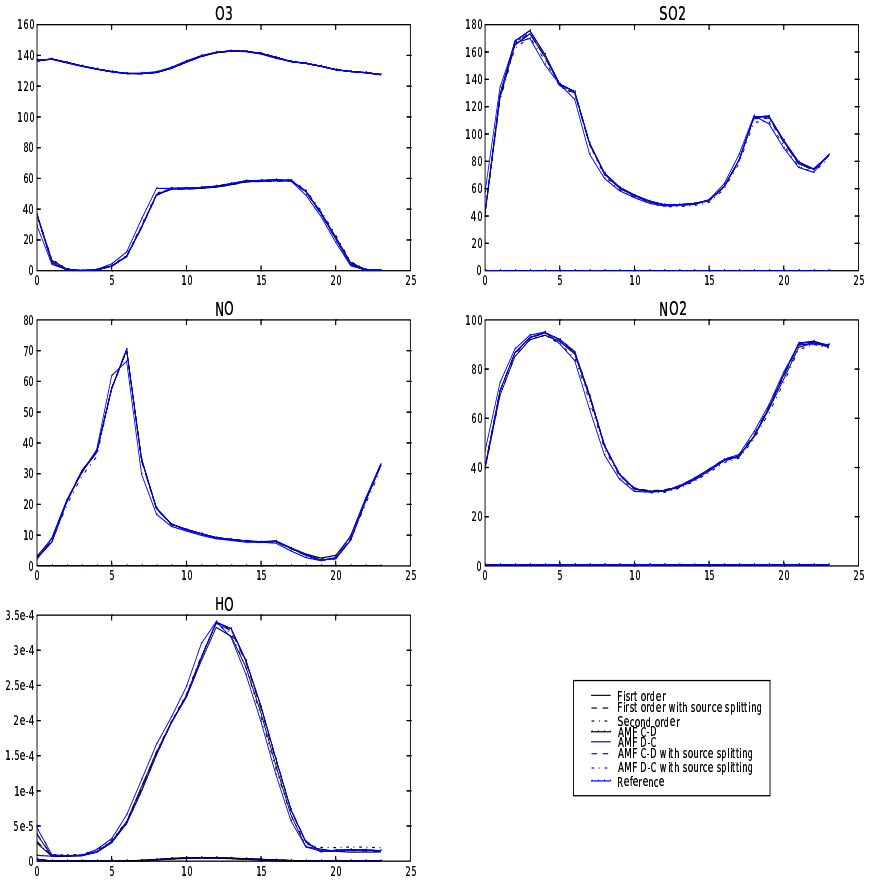

Figure 23: Time evolution of the spatial minimum and maximum ($\mu g \cdot m^{-3}$) for different algorithms

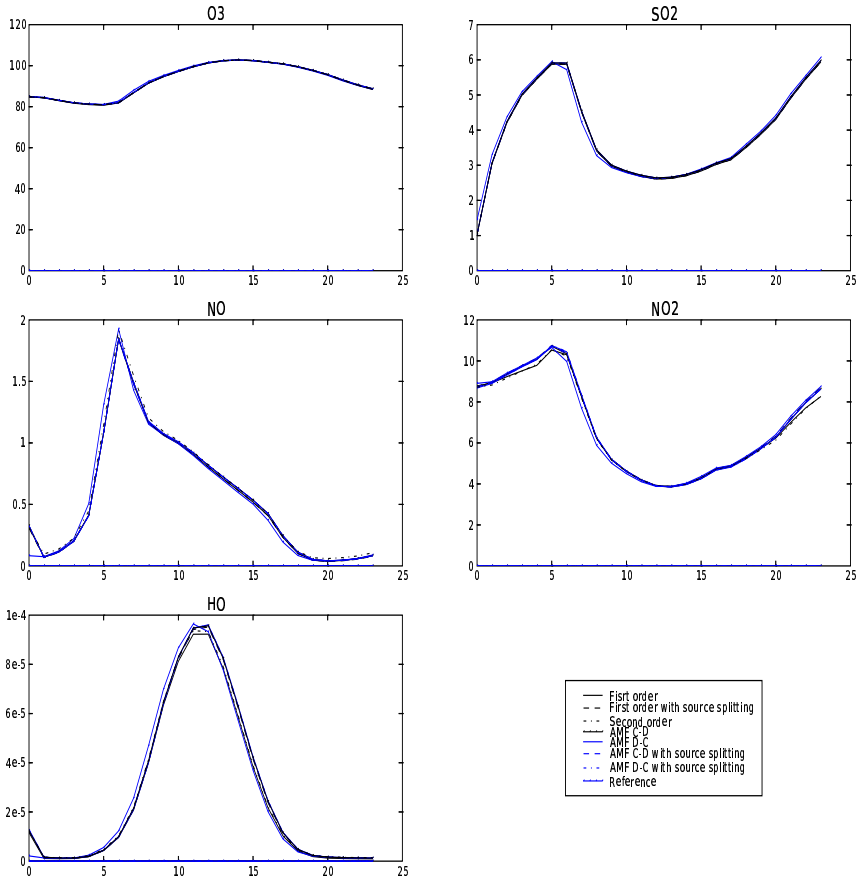

Figure 24: Time evolution of the spatial mean ($\mu g \cdot m^{-3}$) for different algorithms

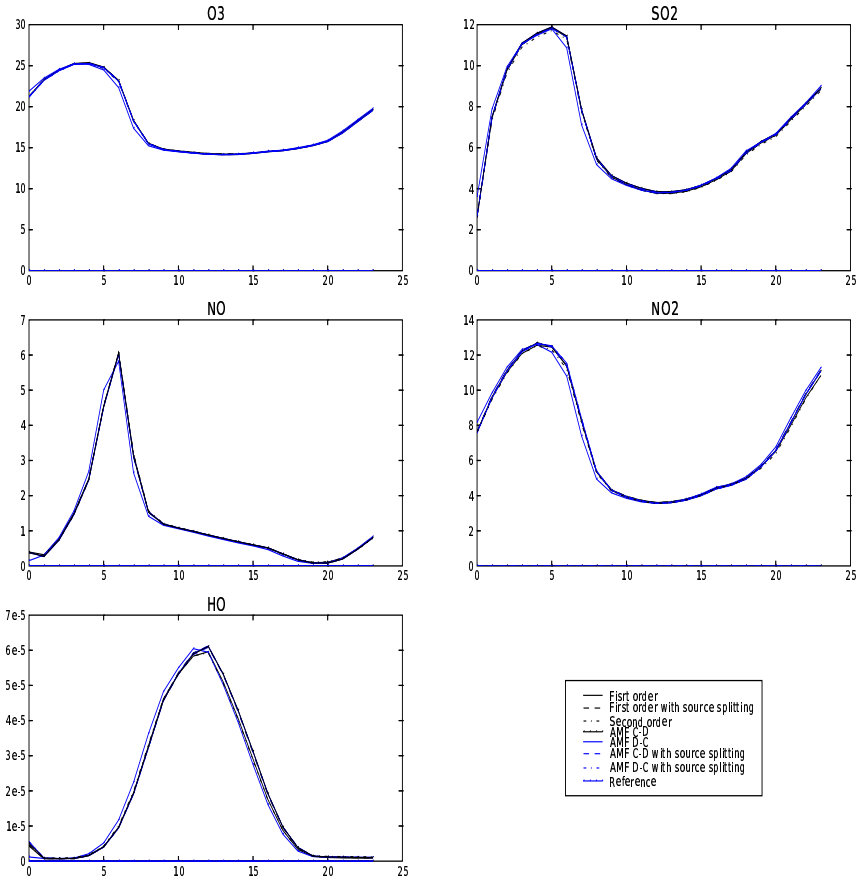

Figure 25: Time evolution of the spatial standard deviation ($\mu g \cdot m^{-3}$) for different algorithms

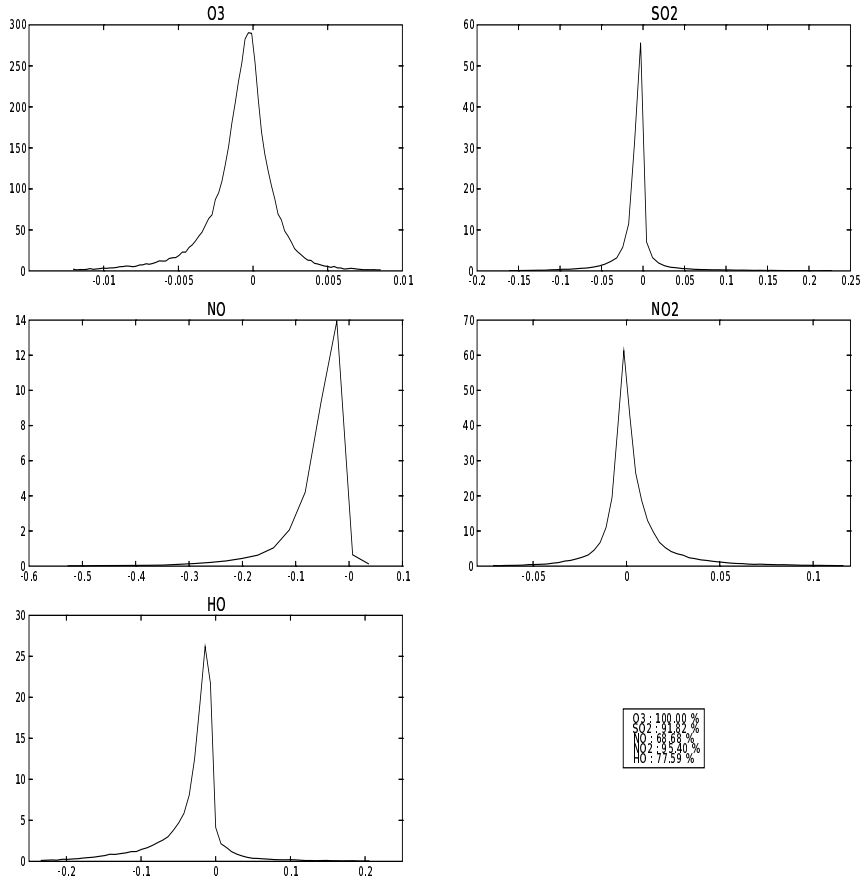

Figure 26: PDF of error between first-order and second-order schemes

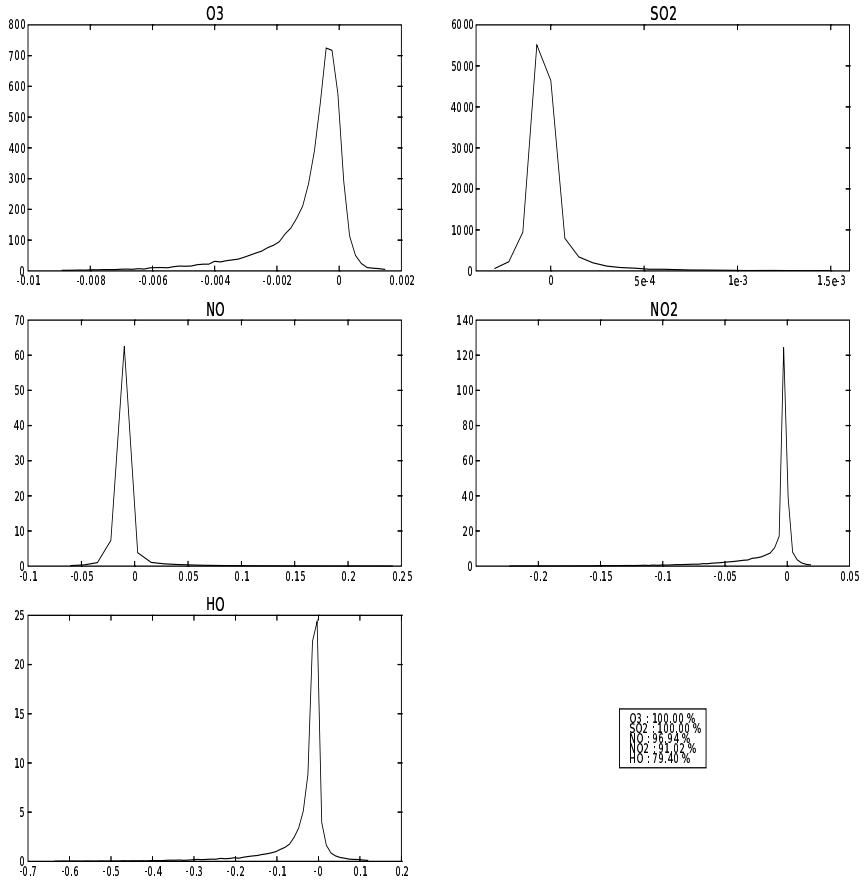

Figure 27: PDF of error between first-order and source-splitting

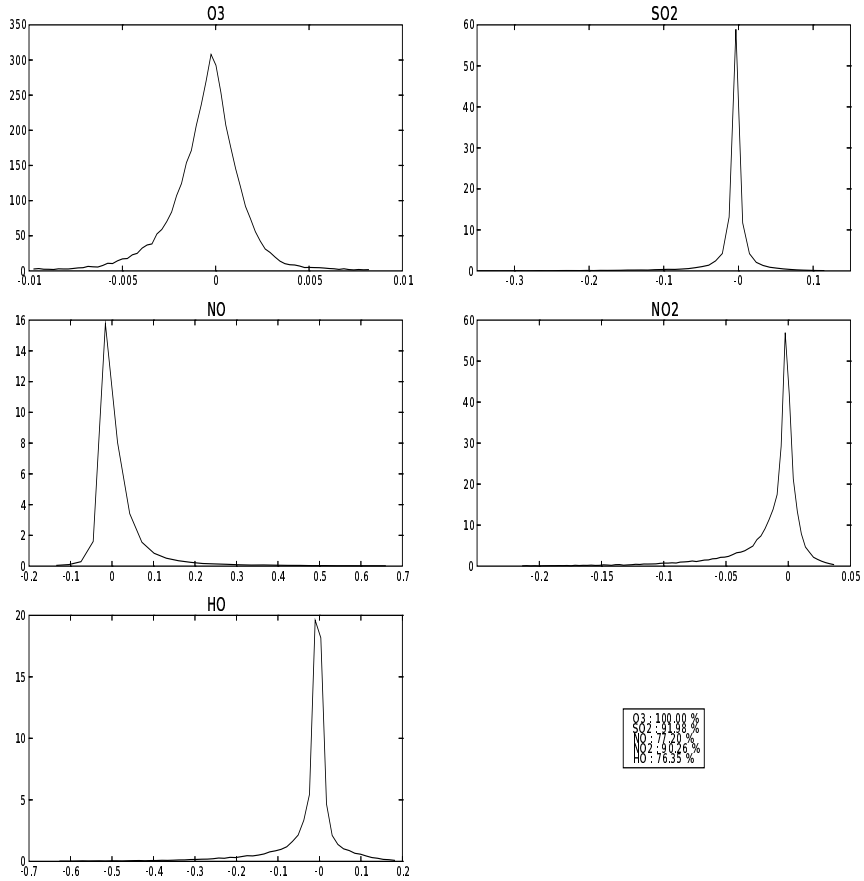

Figure 28: PDF of error between second-order and AMF C-D

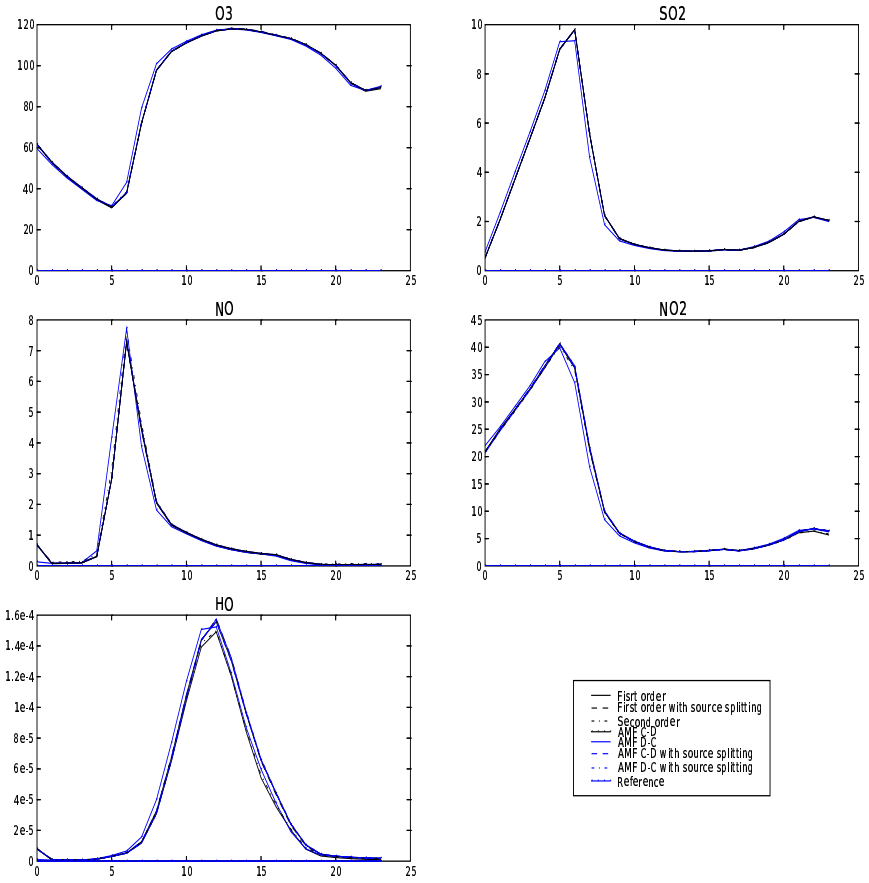

Figure 29: Time evolution of the concentrations ($\mu g \cdot m^{-3}$) over Paris for different algorithms

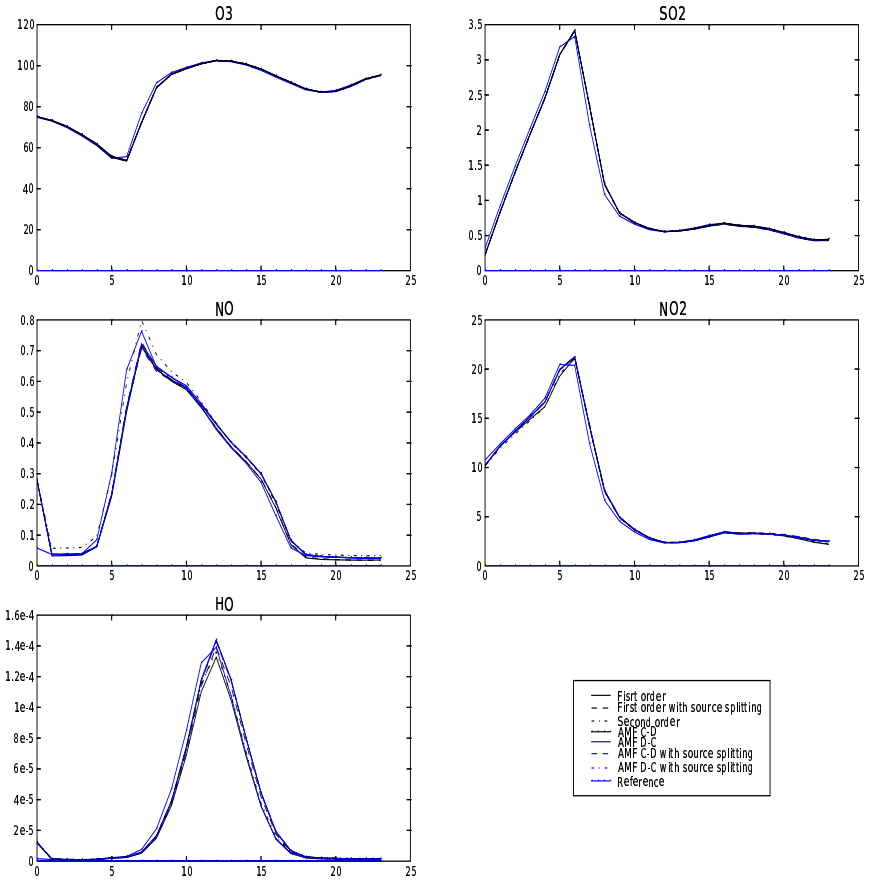

Figure 30: Time evolution of the concentrations ($\mu g \cdot m^{-3}$) over Pontarlier for different algorithms

3.3 Sequence of processes within the splitting

As seen in the introduction, we can choose to integrate the different processes following different sequences. In our case, with 3 processes, there are 6 different series. We want to know whether the choice of the sequence has an influence or not.

First of all, figures 31–33 indicate that species such as O_3 and SO_2 do not seem to be very much influenced by the sequence. As far as the other species are concerned, when a difference may be seen, we can notice that sequences Advection-Chemistry-Diffusion (ACD), CAD and CDA act the same way, while ADC, DAC and DCA act the same way. The key point is then the sequence between chemistry and diffusion (as explained in [8]).

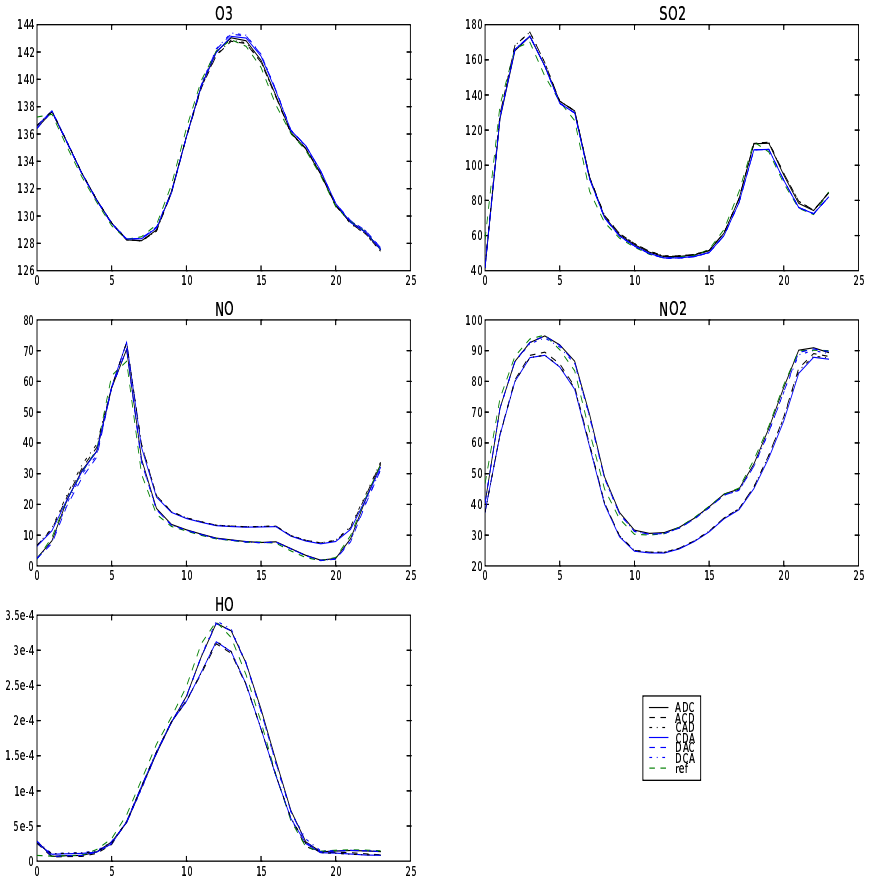

Figure 31: Time evolution of the spatial minimum and maximum ($\mu g \cdot m^{-3}$) for different sequences

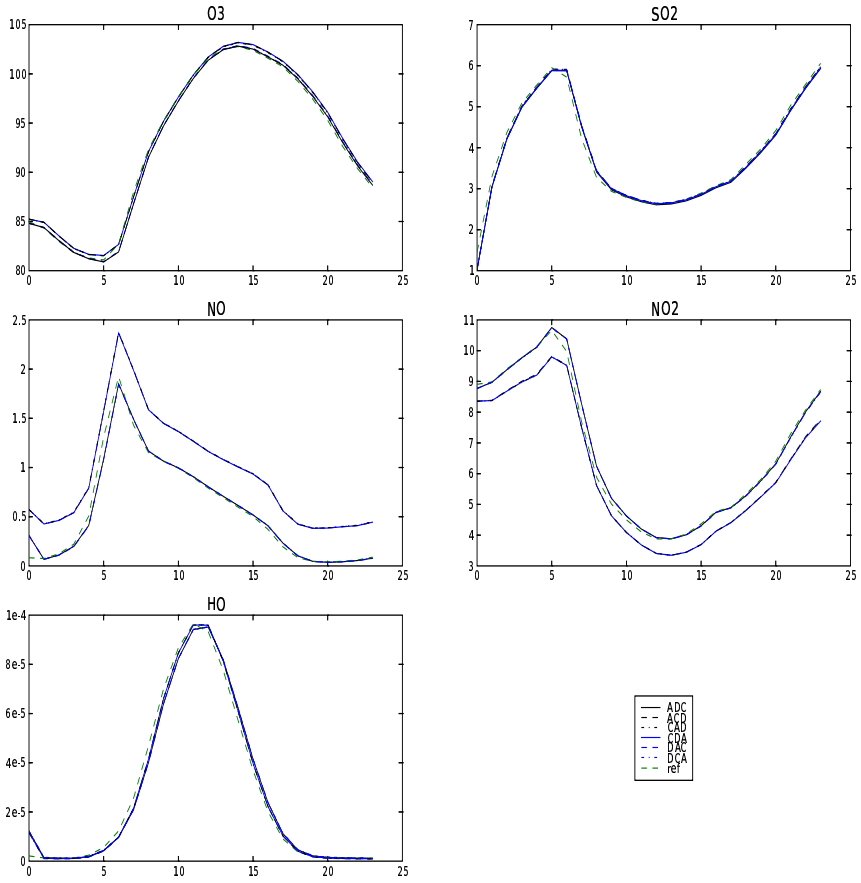

Figure 32: Time evolution of the spatial mean ($\mu g \cdot m^{-3}$) for different sequences

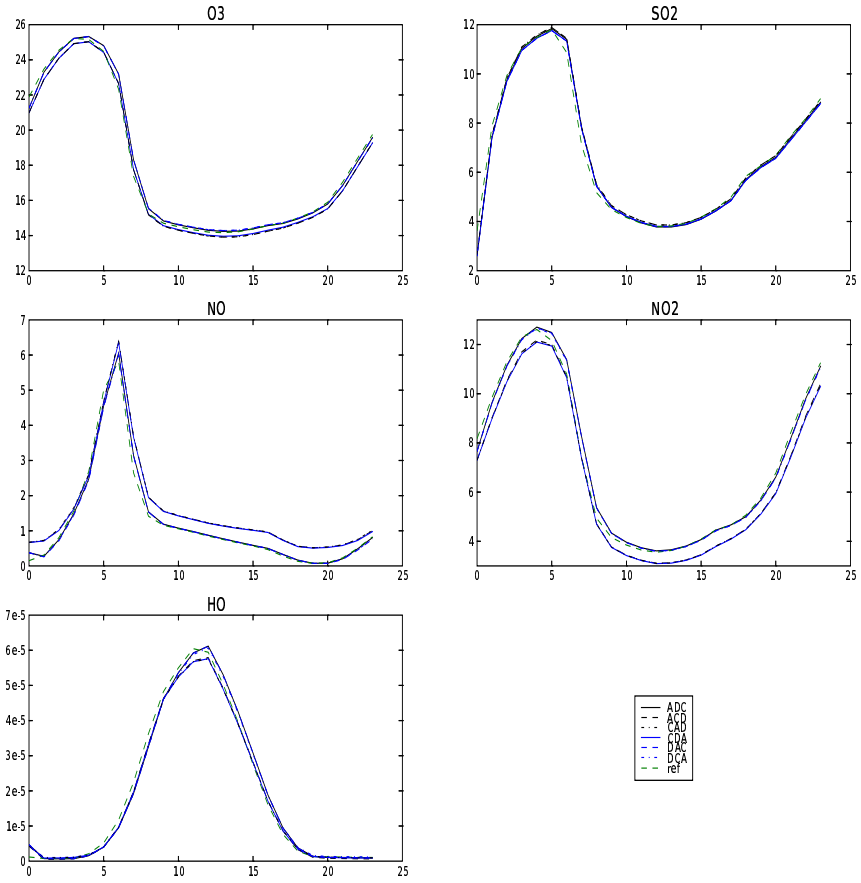

Figure 33: Time evolution of the spatial standard deviation ($\mu g \cdot m^{-3}$) for different sequences

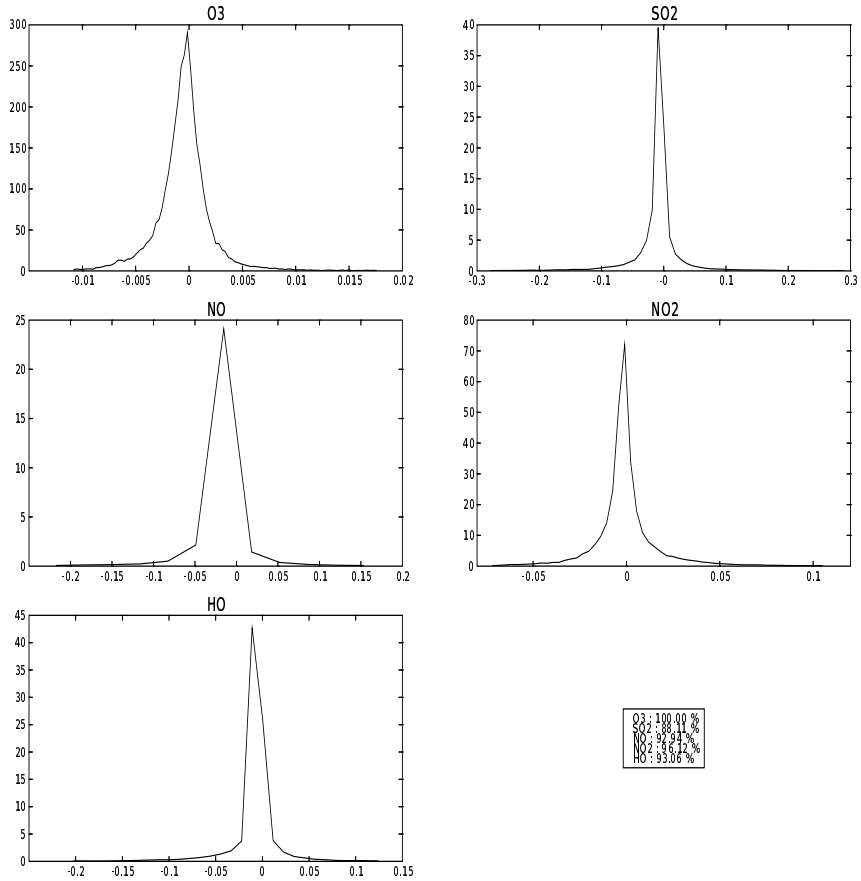

Figure 34: PDF of error between DCA and ADC

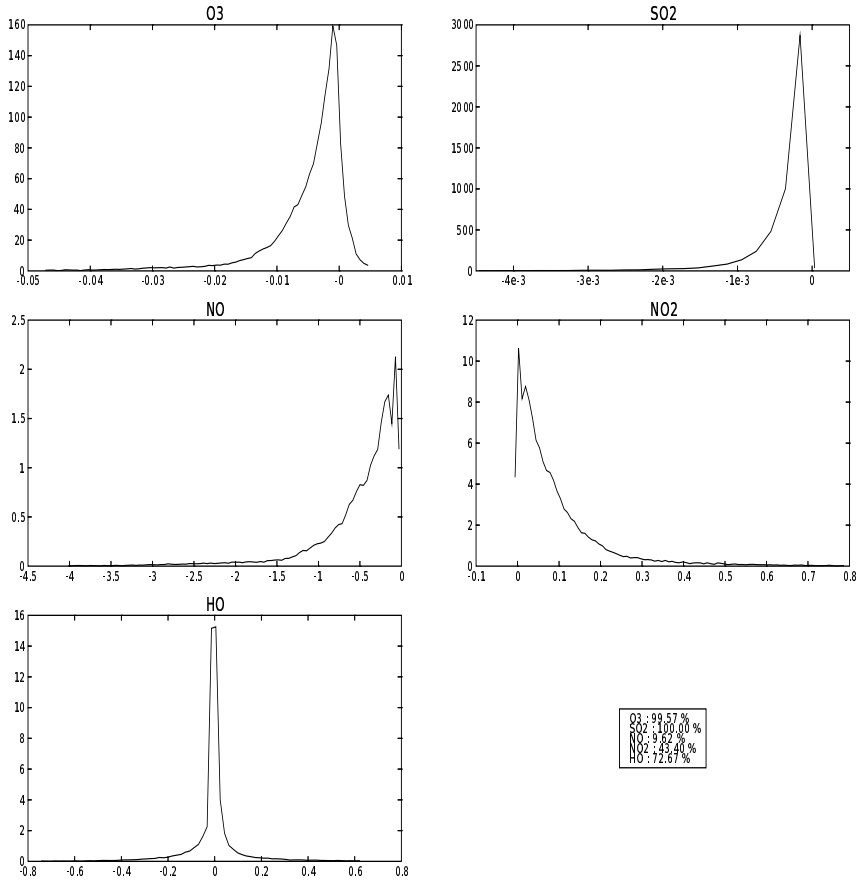

Figure 35: PDF of error between DCA and CDA

3.4 Boundary conditions

The key point about boundary conditions is to choose in which process include them. As a reference, POLAIR3D solves the boundary conditions in the diffusion, that is at the ground (i = 1):

$$K_z(z_{i-\frac{1}{2}})\frac{c(z_i) - c(z_{i-1})}{z_i - z_{i-1}} = E - v^{dep}c(z_i) \tag{41}$$

An alternative is to add the boundary conditions as sources for the chemistry.

In figures 36–38, the impact of boundary conditions is noticeable. This impact is however not so large on a longer simulation, as illustrated in figures 40, 41 and 42, with a weekly simulation.

3.5 Conclusion

The main conclusions are the following ones:

1. The splitting timestep or the scheme order do not make much of a difference. Using a first-order method with a splitting timestep of 600 seconds is then a good compromise between CPU requirements and accuracy.
2. The sequence of processes reveals the importance of the sequence between chemistry and diffusion;chemistry has to end the sequence.
3. As for the boundary conditions, the process in which they are taken into account does make a difference, but this difference does not grow with time, and stays limited.

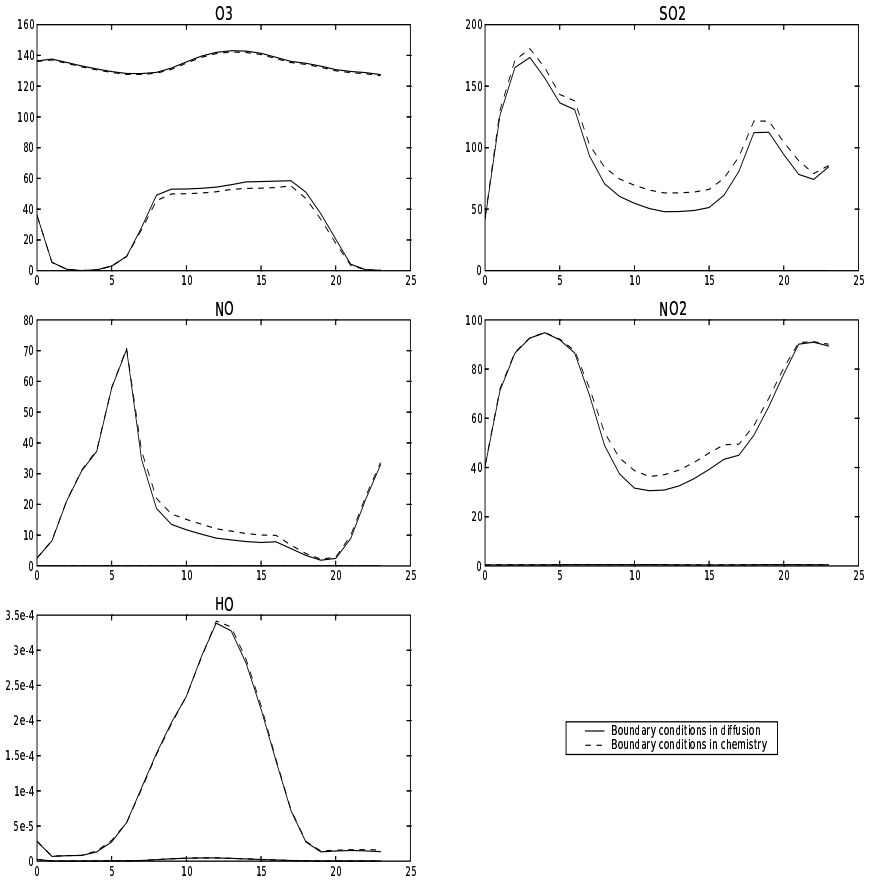

Figure 36: Time evolution of the spatial minimum and maximum ($\mu g \cdot m^{-3}$) for boundary conditions in chemistry or in diffusion

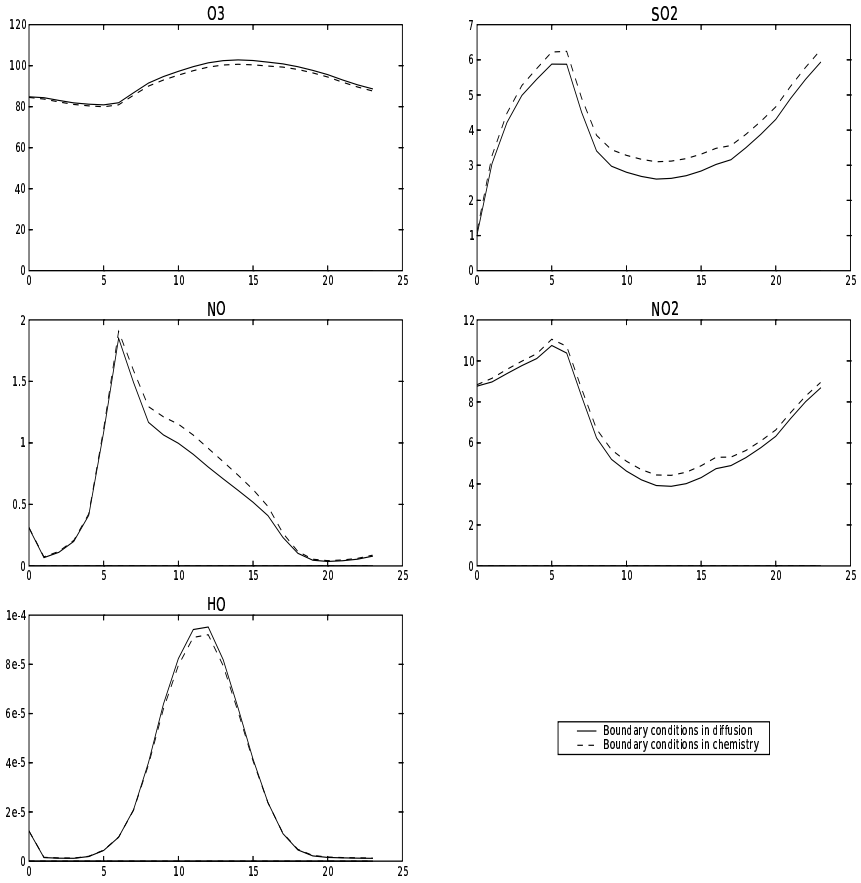

Figure 37: Time evolution of the spatial mean ($\mu g \cdot m^{-3}$) for boundary conditions in chemistry or in diffusion

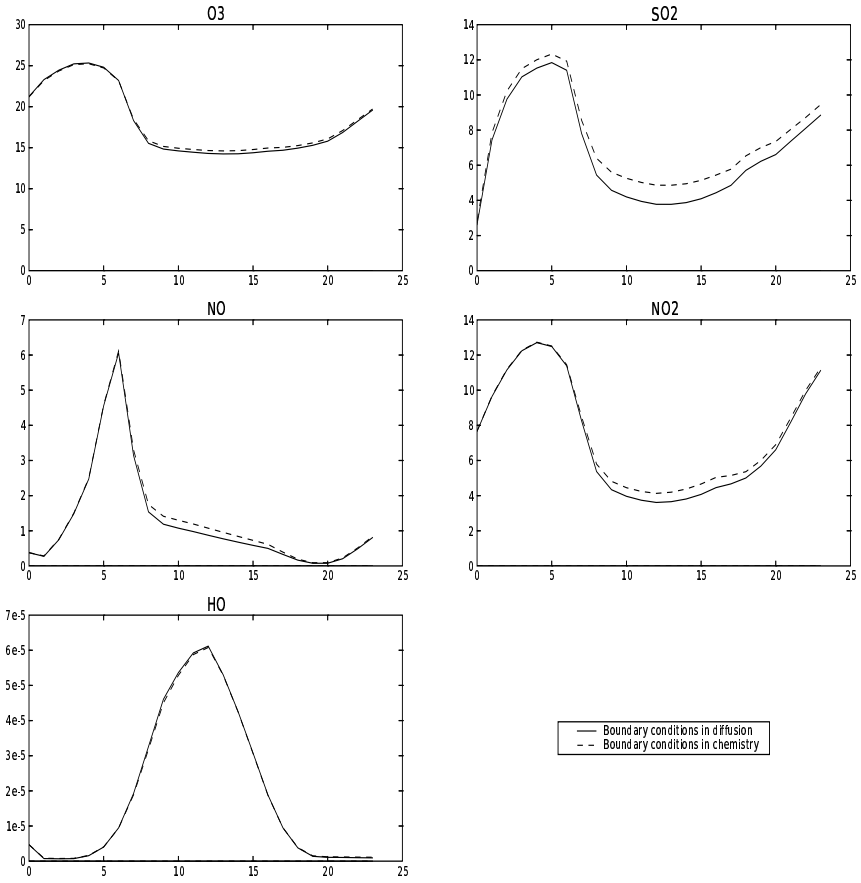

Figure 38: Time evolution of the spatial standard deviation ($\mu g \cdot m^{-3}$) for boundary conditions in chemistry or in diffusion

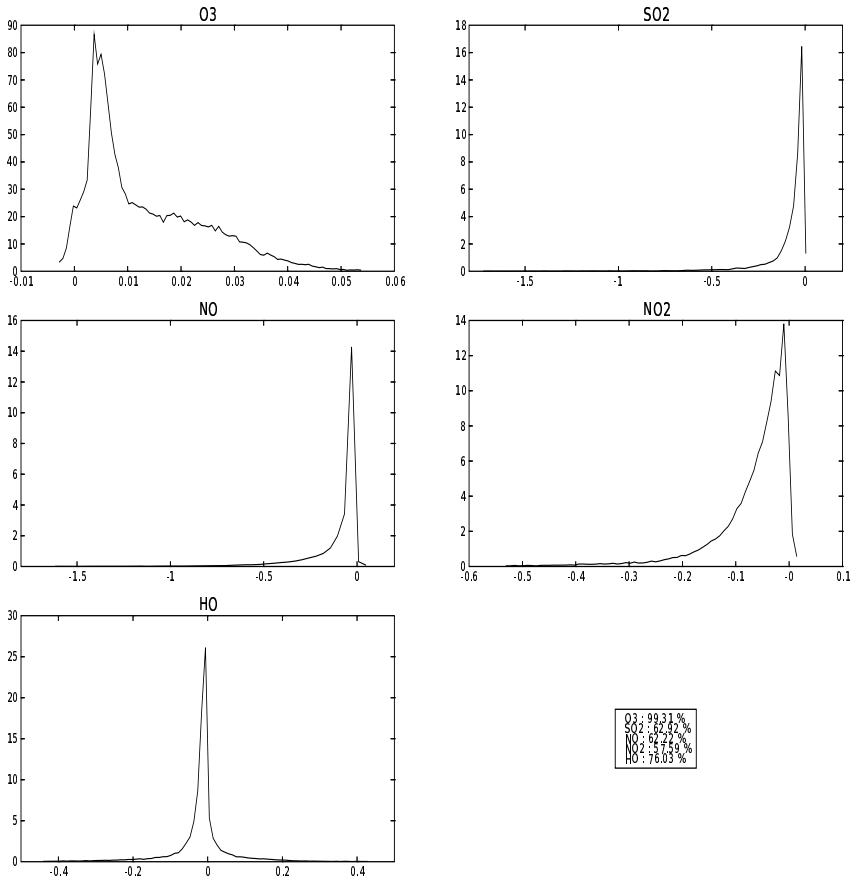

Figure 39: PDF of error between boundary conditions in chemistry and in diffusion

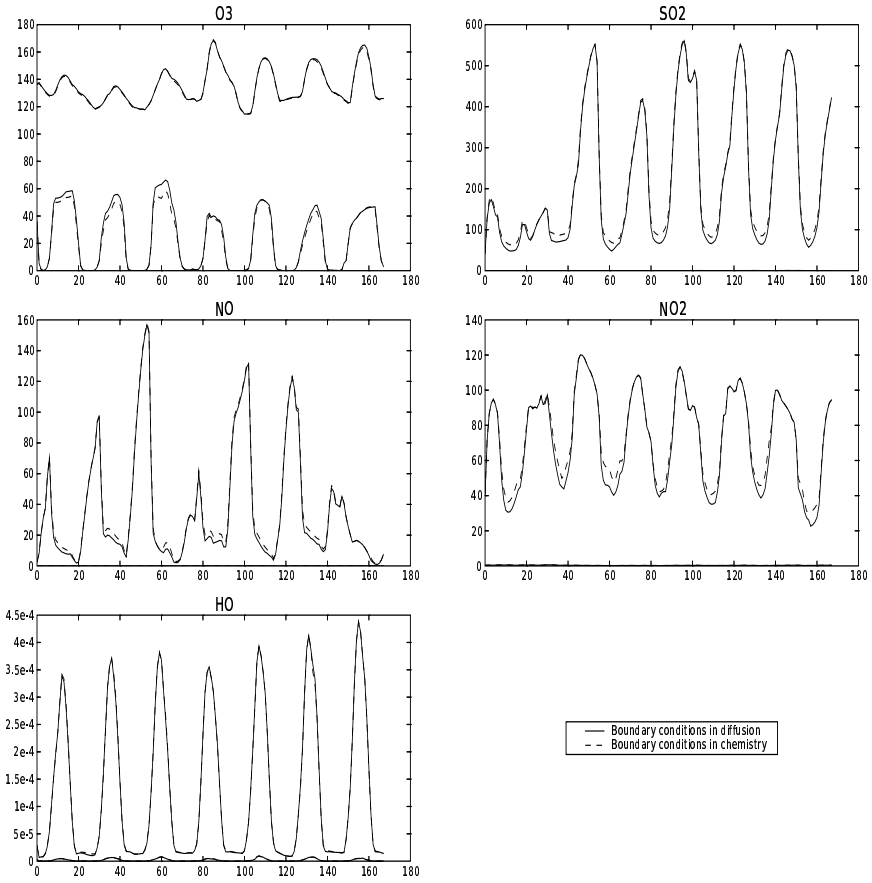

Figure 40: Time evolution of the spatial minimum and maximum ($\mu g \cdot m^{-3}$) for boundary conditions in chemistry or in diffusion for a weekly simulation

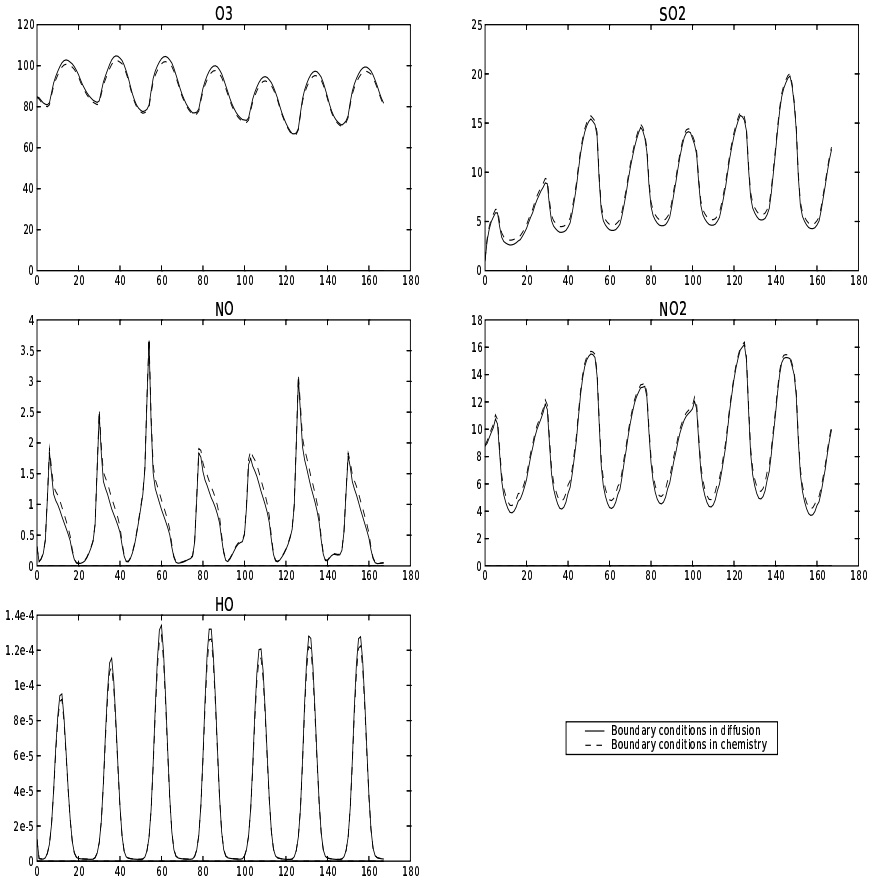

Figure 41: Time evolution of the spatial mean ($\mu g \cdot m^{-3}$) for boundary conditions in chemistry or in diffusion for a weekly simulation

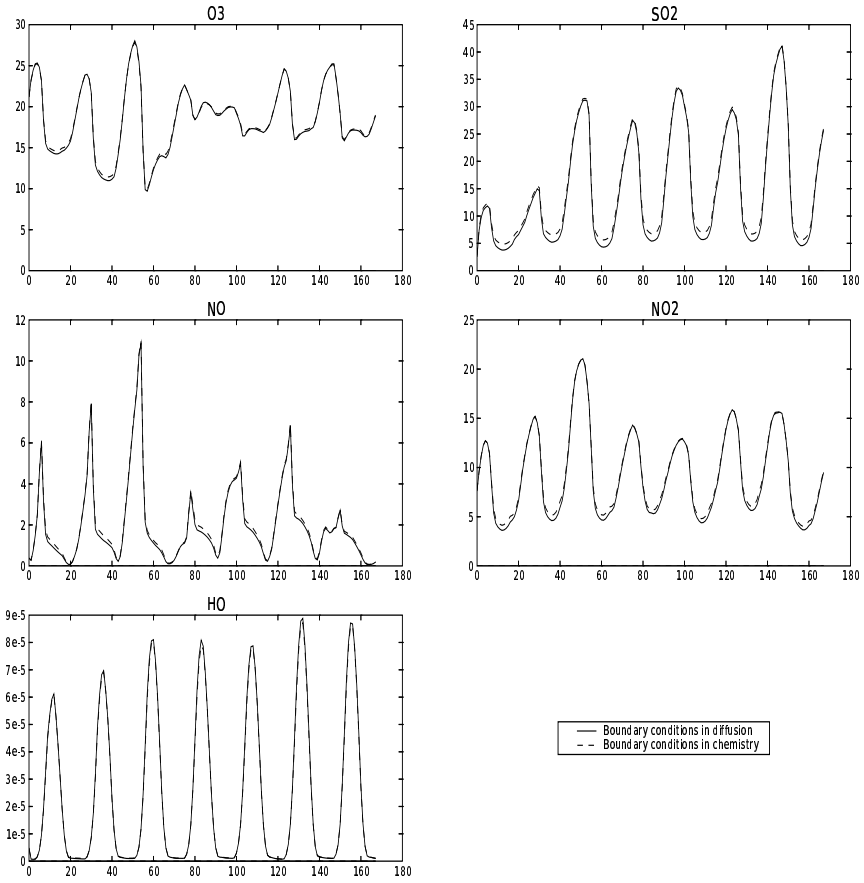

Figure 42: Time evolution of the spatial standard deviation ($\mu g \cdot m^{-3}$) for boundary conditions in chemistry or in diffusion for a weekly simulation

4 Integration of chemical kinetics

4.1 Influence of timestep

The chemistry has its own timestep, 60 seconds as a reference. Other values are tested on a weekly simulation : 30, 100, 200, 300 and 600 seconds. There are no differences, as shown on figures 43–45.

4.2 Clipping

With most chemistry solvers, positivity is not guaranteed. Because it is essential for stability, positivity is enforced by clipping: when a concentration is negative, it is set equal to zero. Clipping interferes with the property of mass conservation, which justifies to investigate its impact.

As shown in Table 2 and figure 47, there is little clipping. Most species are not even concerned, and for the ones that do need clip (38 out of 72 species), it is not very important (the highest factor between the concentrations mean and the clipping mean is 10^{-3} for HO_2).

Table 3 now indicates if the clipping takes place mostly during the morning or during the evening. We can see that it is mostly during the morning, except for API, ISO, O_P^3, ADDC and CSL.

Indeed, as seen in the introduction, the linearized system may be viewed as $\frac{dc}{dt} = -k(t) \cdot c$ where $k(t)$ is typically a photolytical rate (and as such time-dependent). The difficult case occurs when stifness is added, that is to say when $k(t)$ is growing (for instance at sunrise).

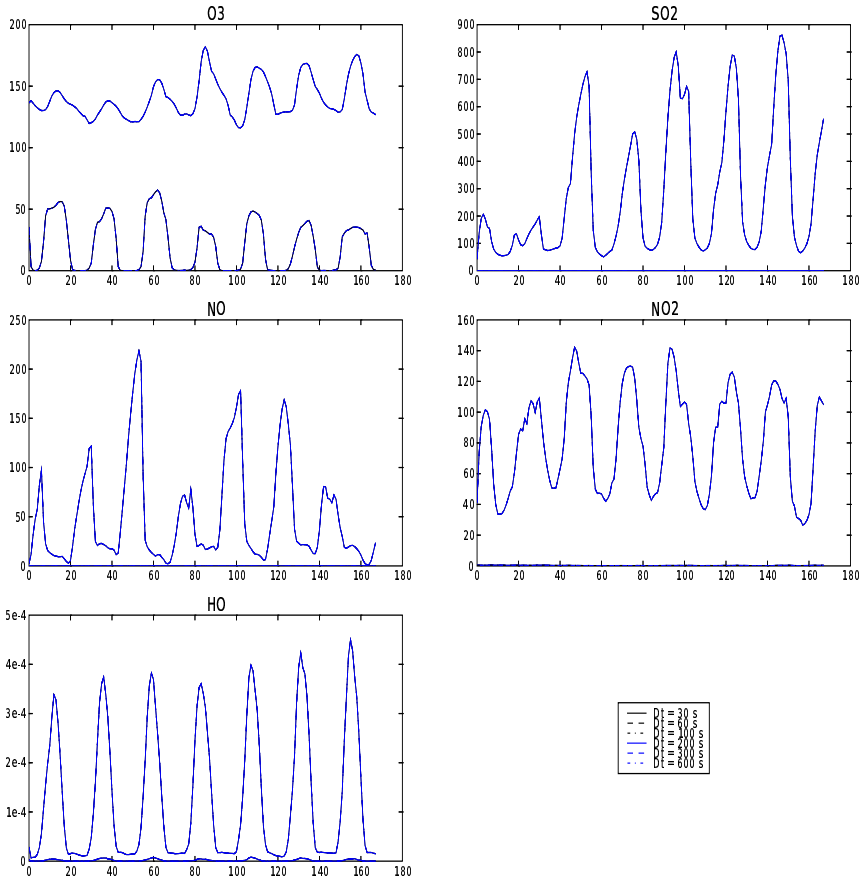

Figure 43: Time evolution of the spatial minimum and maximum ($\mu g \cdot m^{-3}$) for different timesteps in the chemistry

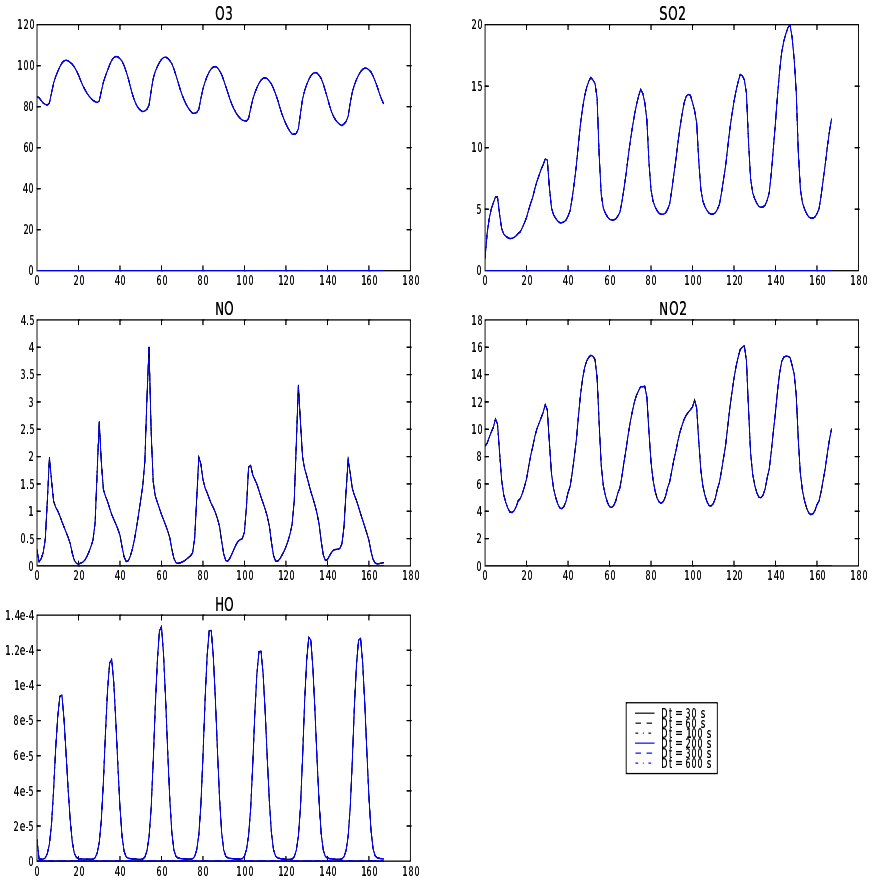

Figure 44: Time evolution of the spatial mean ($\mu g \cdot m^{-3}$) for different timesteps in the chemistry

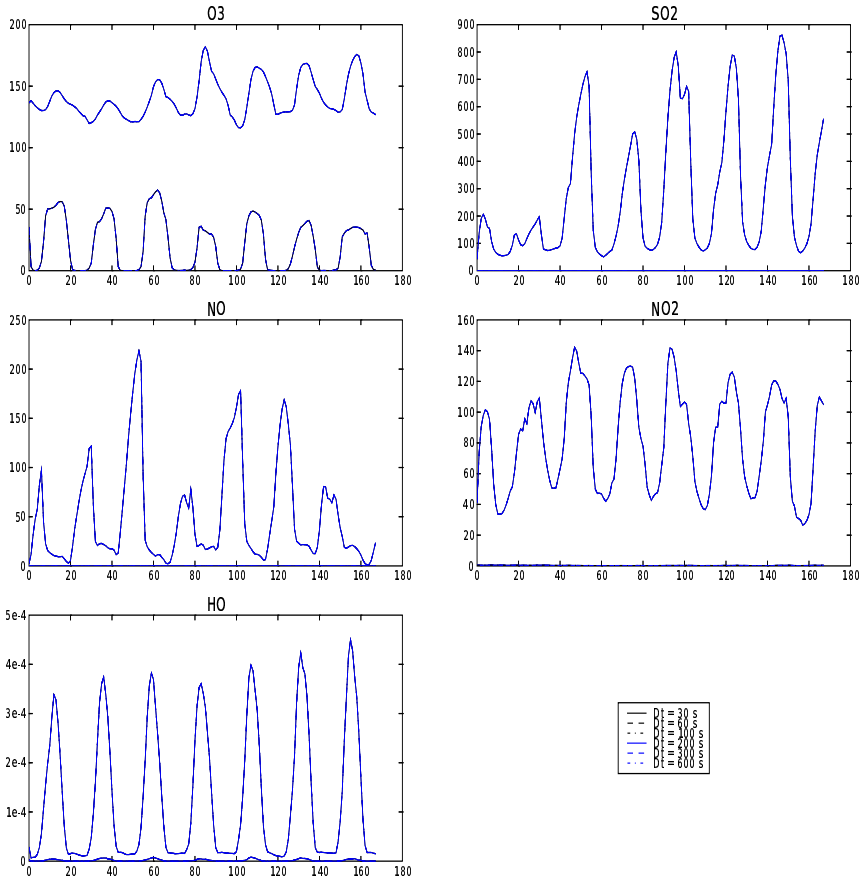

Figure 45: Time evolution of the spatial standard deviation ($\mu g \cdot m^{-3}$) for different timesteps in the chemistry

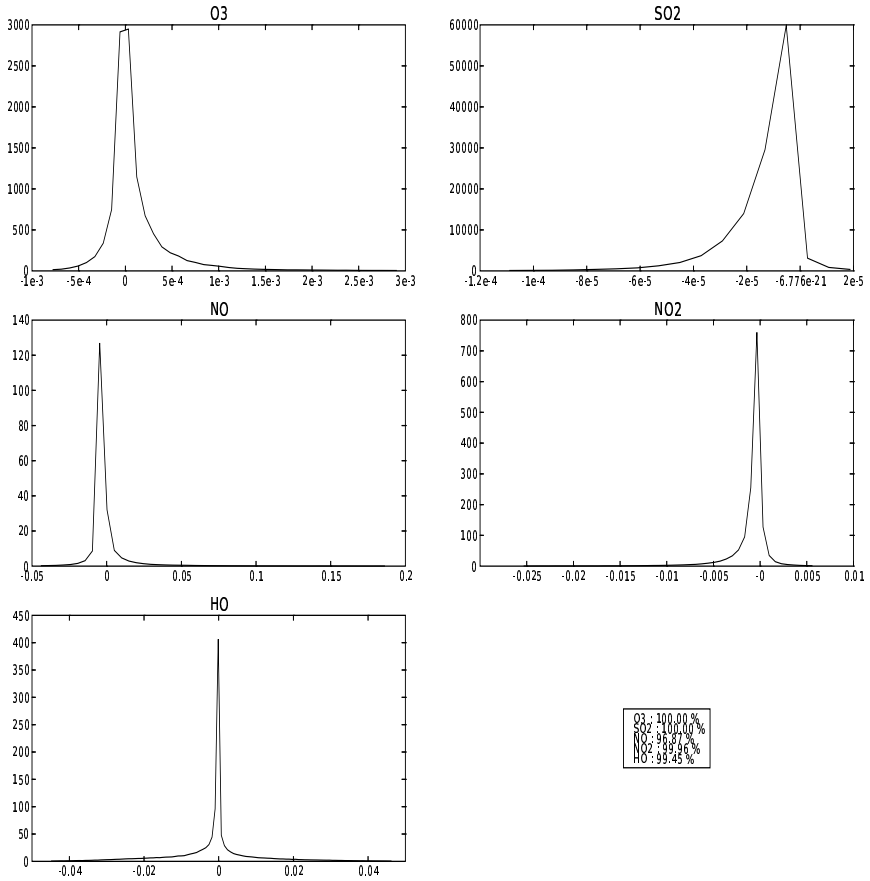

Figure 46: PDF of error between Dt=30s and Dt=600s in chemistry

Species	Mean	Clipping mean	Species	Mean	Clipping mean
SO2	$8.27 \cdot 10^{+00}$	$0.00 \cdot 10^{+00}$	HC3	$4.88 \cdot 10^{+00}$	$0.00 \cdot 10^{+00}$
HC5	$1.17 \cdot 10^{+00}$	$0.00 \cdot 10^{+00}$	HC8	$2.11 \cdot 10^{+00}$	$0.00 \cdot 10^{+00}$
TOL	$6.50 \cdot 10^{-01}$	$0.00 \cdot 10^{+00}$	XYL	$6.22 \cdot 10^{-01}$	$0.00 \cdot 10^{+00}$
O1D	$1.28 \cdot 10^{-13}$	$2.40 \cdot 10^{-21}$	SULF	$7.17 \cdot 10^{-01}$	$0.00 \cdot 10^{+00}$
N2O5	$3.60 \cdot 10^{-01}$	$0.00 \cdot 10^{+00}$	UDD	$1.44 \cdot 10^{-03}$	$6.91 \cdot 10^{-09}$
ETE	$3.46 \cdot 10^{-01}$	$0.00 \cdot 10^{+00}$	DIEN	$0.00 \cdot 10^{+00}$	$0.00 \cdot 10^{+00}$
API	$1.24 \cdot 10^{-01}$	$4.18 \cdot 10^{-14}$	LIM	$0.00 \cdot 10^{+00}$	$0.00 \cdot 10^{+00}$
HNO4	$3.62 \cdot 10^{-02}$	$0.00 \cdot 10^{+00}$	OP1	$3.96 \cdot 10^{-01}$	$0.00 \cdot 10^{+00}$
ADDT	$9.51 \cdot 10^{-10}$	$1.81 \cdot 10^{-16}$	ADDX	$2.95 \cdot 10^{-09}$	$6.66 \cdot 10^{-16}$
ISO	$4.56 \cdot 10^{-01}$	$6.01 \cdot 10^{-09}$	CH4	$1.14 \cdot 10^{+03}$	$0.00 \cdot 10^{+00}$
ETH	$2.15 \cdot 10^{+00}$	$0.00 \cdot 10^{+00}$	ADDC	$8.88 \cdot 10^{-11}$	$8.46 \cdot 10^{-17}$
HONO	$4.43 \cdot 10^{-02}$	$1.34 \cdot 10^{-06}$	HKET	$9.43 \cdot 10^{-02}$	$1.57 \cdot 10^{-07}$
TPAN	$1.36 \cdot 10^{-01}$	$5.15 \cdot 10^{-08}$	PAN	$3.02 \cdot 10^{+00}$	$0.00 \cdot 10^{+00}$
H2O2	$7.33 \cdot 10^{-01}$	$0.00 \cdot 10^{+00}$	PAA	$6.10 \cdot 10^{-02}$	$2.88 \cdot 10^{-10}$
PHO	$3.24 \cdot 10^{-07}$	$6.97 \cdot 10^{-12}$	CSL	$3.88 \cdot 10^{-03}$	$2.00 \cdot 10^{-10}$
TOLP	$1.04 \cdot 10^{-04}$	$0.00 \cdot 10^{+00}$	XYLP	$2.98 \cdot 10^{-04}$	$0.00 \cdot 10^{+00}$
CSLP	$6.66 \cdot 10^{-06}$	$0.00 \cdot 10^{+00}$	ORA1	$4.66 \cdot 10^{-02}$	$2.64 \cdot 10^{-08}$
O3P	$1.02 \cdot 10^{-07}$	$2.90 \cdot 10^{-15}$	HC5P	$1.11 \cdot 10^{-04}$	$0.00 \cdot 10^{+00}$
HC8P	$7.24 \cdot 10^{-04}$	$1.69 \cdot 10^{-07}$	ETEP	$8.32 \cdot 10^{-05}$	$1.66 \cdot 10^{-08}$
ISOP	$4.63 \cdot 10^{-03}$	$5.13 \cdot 10^{-08}$	OLT	$2.83 \cdot 10^{-01}$	$0.00 \cdot 10^{+00}$
OLTP	$4.66 \cdot 10^{-04}$	$2.84 \cdot 10^{-08}$	APIP	$5.61 \cdot 10^{-04}$	$1.27 \cdot 10^{-08}$
LIMP	$0.00 \cdot 10^{+00}$	$0.00 \cdot 10^{+00}$	OLI	$1.83 \cdot 10^{-02}$	$0.00 \cdot 10^{+00}$
OLIP	$3.79 \cdot 10^{-05}$	$0.00 \cdot 10^{+00}$	OLND	$5.55 \cdot 10^{-03}$	$2.26 \cdot 10^{-05}$
OLNN	$2.28 \cdot 10^{-03}$	$3.12 \cdot 10^{-05}$	DCB	$2.12 \cdot 10^{-02}$	$0.00 \cdot 10^{+00}$
MACR	$1.26 \cdot 10^{-01}$	$4.23 \cdot 10^{-07}$	O3	$8.81 \cdot 10^{+01}$	$0.00 \cdot 10^{+00}$
GLY	$4.83 \cdot 10^{-02}$	$2.28 \cdot 10^{-07}$	CO	$1.98 \cdot 10^{+02}$	$0.00 \cdot 10^{+00}$
OP2	$6.74 \cdot 10^{-01}$	$3.82 \cdot 10^{-07}$	MGLY	$7.32 \cdot 10^{-02}$	$1.25 \cdot 10^{-07}$
HNO3	$2.44 \cdot 10^{+00}$	$0.00 \cdot 10^{+00}$	TCO3	$2.56 \cdot 10^{-05}$	$5.86 \cdot 10^{-11}$
ORA2	$2.22 \cdot 10^{-01}$	$0.00 \cdot 10^{+00}$	KETP	$9.45 \cdot 10^{-04}$	$1.90 \cdot 10^{-08}$
KET	$6.37 \cdot 10^{+00}$	$0.00 \cdot 10^{+00}$	ETHP	$2.21 \cdot 10^{-04}$	$2.00 \cdot 10^{-07}$
ALD	$5.81 \cdot 10^{-01}$	$0.00 \cdot 10^{+00}$	HO	$3.54 \cdot 10^{-05}$	$5.56 \cdot 10^{-09}$
MO2	$1.16 \cdot 10^{-03}$	$2.64 \cdot 10^{-07}$	HC3P	$5.01 \cdot 10^{-04}$	$3.15 \cdot 10^{-08}$
XO2	$2.89 \cdot 10^{-04}$	$2.71 \cdot 10^{-08}$	HCHO	$9.59 \cdot 10^{-01}$	$0.00 \cdot 10^{+00}$
NO	$8.17 \cdot 10^{-01}$	$1.37 \cdot 10^{-05}$	NO3	$9.13 \cdot 10^{-03}$	$3.00 \cdot 10^{-06}$
ACO3	$3.14 \cdot 10^{-04}$	$3.00 \cdot 10^{-09}$	ONIT	$8.17 \cdot 10^{-01}$	$1.64 \cdot 10^{-06}$
HO2	$3.14 \cdot 10^{-03}$	$4.02 \cdot 10^{-07}$	NO2	$8.59 \cdot 10^{+00}$	$0.00 \cdot 10^{+00}$

Table 2: Comparison between concentrations mean and clipping mean ($\mu g \cdot m^{-3}$) over a week with $\Delta t = 600$ s

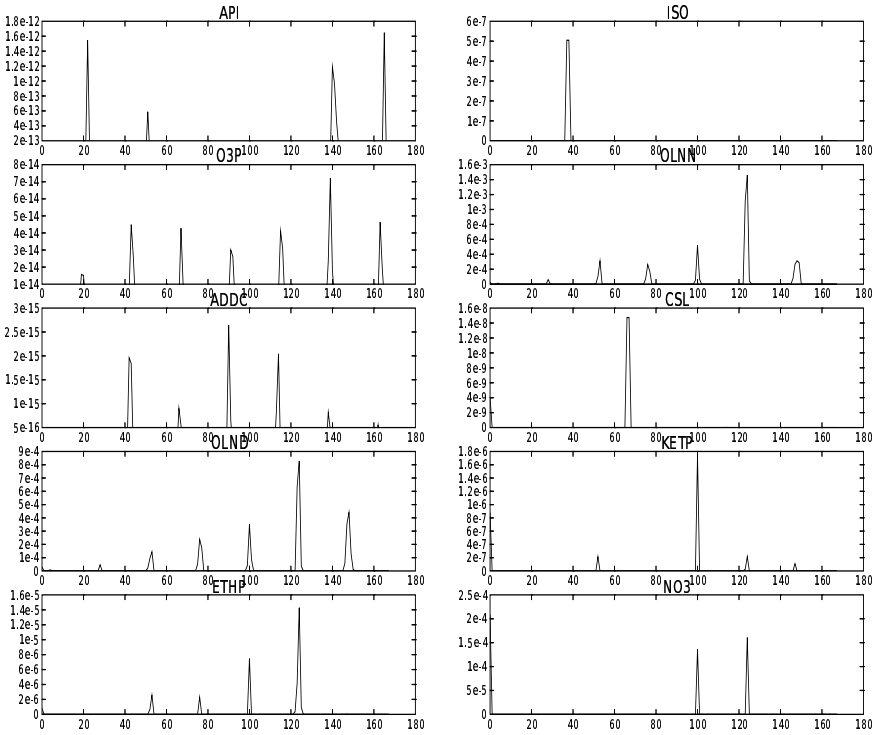

Figure 47: Clipping concentrations mean ($\mu g \cdot m^{-3}$) as a function of time (in hours)

Species	Morning clipping	Evening clipping	Species	Morning clipping	Evening clipping
O1D	$2.38 \cdot 10^{-21}$	$1.97 \cdot 10^{-23}$	UDD	$6.91 \cdot 10^{-09}$	$0.00 \cdot 10^{+00}$
API	$5.10 \cdot 10^{-15}$	$3.67 \cdot 10^{-14}$	ADDT	$1.81 \cdot 10^{-16}$	$0.00 \cdot 10^{+00}$
ADDX	$6.66 \cdot 10^{-16}$	$0.00 \cdot 10^{+00}$	ISO	$0.00 \cdot 10^{+00}$	$6.01 \cdot 10^{-09}$
ADDC	$1.82 \cdot 10^{-18}$	$8.28 \cdot 10^{-17}$	HONO	$1.34 \cdot 10^{-06}$	$0.00 \cdot 10^{+00}$
HKET	$1.57 \cdot 10^{-07}$	$0.00 \cdot 10^{+00}$	TPAN	$5.15 \cdot 10^{-08}$	$0.00 \cdot 10^{+00}$
PAA	$2.88 \cdot 10^{-10}$	$0.00 \cdot 10^{+00}$	PHO	$6.97 \cdot 10^{-12}$	$0.00 \cdot 10^{+00}$
CSL	$2.40 \cdot 10^{-11}$	$1.75 \cdot 10^{-10}$	ORA1	$2.64 \cdot 10^{-08}$	$0.00 \cdot 10^{+00}$
O3P	$1.54 \cdot 10^{-17}$	$2.89 \cdot 10^{-15}$	HC8P	$1.69 \cdot 10^{-07}$	$0.00 \cdot 10^{+00}$
ETEP	$1.66 \cdot 10^{-08}$	$0.00 \cdot 10^{+00}$	ISOP	$5.07 \cdot 10^{-08}$	$5.56 \cdot 10^{-10}$
OLTP	$2.84 \cdot 10^{-08}$	$0.00 \cdot 10^{+00}$	APIP	$1.27 \cdot 10^{-08}$	$0.00 \cdot 10^{+00}$
OLND	$2.26 \cdot 10^{-05}$	$0.00 \cdot 10^{+00}$	OLNN	$3.12 \cdot 10^{-05}$	$0.00 \cdot 10^{+00}$
MACR	$4.23 \cdot 10^{-07}$	$0.00 \cdot 10^{+00}$	GLY	$2.28 \cdot 10^{-07}$	$0.00 \cdot 10^{+00}$
OP2	$3.82 \cdot 10^{-07}$	$0.00 \cdot 10^{+00}$	MGLY	$1.25 \cdot 10^{-07}$	$0.00 \cdot 10^{+00}$
TCO3	$5.86 \cdot 10^{-11}$	$0.00 \cdot 10^{+00}$	KETP	$1.90 \cdot 10^{-08}$	$0.00 \cdot 10^{+00}$
ETHP	$2.00 \cdot 10^{-07}$	$0.00 \cdot 10^{+00}$	HO	$5.56 \cdot 10^{-09}$	$0.00 \cdot 10^{+00}$
MO2	$2.64 \cdot 10^{-07}$	$0.00 \cdot 10^{+00}$	HC3P	$3.15 \cdot 10^{-08}$	$0.00 \cdot 10^{+00}$
XO2	$2.71 \cdot 10^{-08}$	$0.00 \cdot 10^{+00}$	NO	$1.37 \cdot 10^{-05}$	$0.00 \cdot 10^{+00}$
NO3	$3.00 \cdot 10^{-06}$	$0.00 \cdot 10^{+00}$	ACO3	$3.00 \cdot 10^{-09}$	$0.00 \cdot 10^{+00}$
ONIT	$1.64 \cdot 10^{-06}$	$0.00 \cdot 10^{+00}$	HO2	$4.02 \cdot 10^{-07}$	$0.00 \cdot 10^{+00}$

Table 3: Comparison between morning clipping and evening clipping ($\mu\ g\ \cdot\ m^{-3}$) over a week with $\Delta t = 600$ s

4.3 Influence of γ value

As seen in section 1, γ has been chosen equal to $1 + \frac{\sqrt{2}}{2}$, but it can be different. We want to test the influence of γ value, with respect to stability and to clipping. The method is A-stable for $\gamma \geq \frac{1}{4}$ and L-stable for $\gamma = 1 \pm \frac{\sqrt{2}}{2}$. We test the method with different values of γ: $1 - \frac{\sqrt{2}}{2}$, 0.5, 1, 1.5, $1 + \frac{\sqrt{2}}{2}$, 2, 3, 4, 5 and 10 for a continental run with $\Delta t = 600s$.

The stability function is:

$$qR(\lambda) = \frac{(2\gamma^2 - (3+\beta)\gamma + \beta)\lambda^2 + (4\gamma - 1 - \beta)\lambda + 2}{2(1+\gamma\lambda)^2} \tag{42}$$

with $\beta = \frac{k_{n+1}}{k_n}$. One way to get the L-stability (ie $\lim_{\lambda \to +\infty} R(\lambda) = 0$) is to take $\gamma(\beta)$ solution of:

$$2\gamma^2 - (3+\beta)\gamma + \beta = 0. \tag{43}$$

Since $\Delta = (3+\beta)^2 - 8\beta > 0 \quad \forall \beta$, there are two solutions:

$$\gamma^+ = \frac{3 + \beta + \sqrt{\beta^2 - 2\beta + 9}}{4} \quad \text{and} \quad \gamma^- = \frac{3 + \beta - \sqrt{\beta^2 - 2\beta + 9}}{4} \tag{44}$$

By taking γ^+, the stability function becomes:

$$R(\lambda) = \frac{\left(2 + \sqrt{\beta^2 - 2\beta + 9}\right)\lambda + 2}{2(1+\gamma\lambda)^2} \tag{45}$$

Since λ is positive, we have $R(\lambda) \geq 0$, and the scheme is therefore positive. We shall note γ_{BS} this value of γ that guarantees positivity and L-stability. In practice, γ_{BS} is computed by calculating the Jacobian at time n+1 with the same concentrations but with updated photolytic constants. The value of γ_{BS} is then taken equal to the maximum ratio of the values on the diagonals.

As seen in figures 48, 50 and 52, the concentrations' mean is not much influenced by the value of γ; the only value that seems to bring instability is $\gamma = 10$, for example with PHO that jumps from about $3.20 \cdot 10^{-7}$ to $8.30 \cdot 10^{-6}$. Notice that a large value of γ may also be seen as a large Δt, leading to instability.

However, as far as the clipping is concerned, we can see in figures 49, 51 and 53 that it is much more unstable. It seems that the clipping concentrations mean finds a minimum, at least for the species we are looking at, for a γ between $1 + \frac{\sqrt{2}}{2}$ and 4. As far as γ_{BS} is concerned, we do not get better results as compared to $\gamma = 1 + \frac{\sqrt{2}}{2}$. In order to know if there is an influence with another timestep, we run simulations

with $\Delta t = 1800$ seconds. Figures 54–59 indicate that γ_{BS} is not better than $\gamma = 1 + \frac{\sqrt{2}}{2}$. For some species, it is even worse. Therefore, $1 + \frac{\sqrt{2}}{2}$ seems to be the best value to give to γ.

4.4 Conclusion

The clipping takes place mostly during the morning, is not so important and does not affect all species. As for the value of γ, the classical choice made in POLAIR3D seems to be a good compromise.

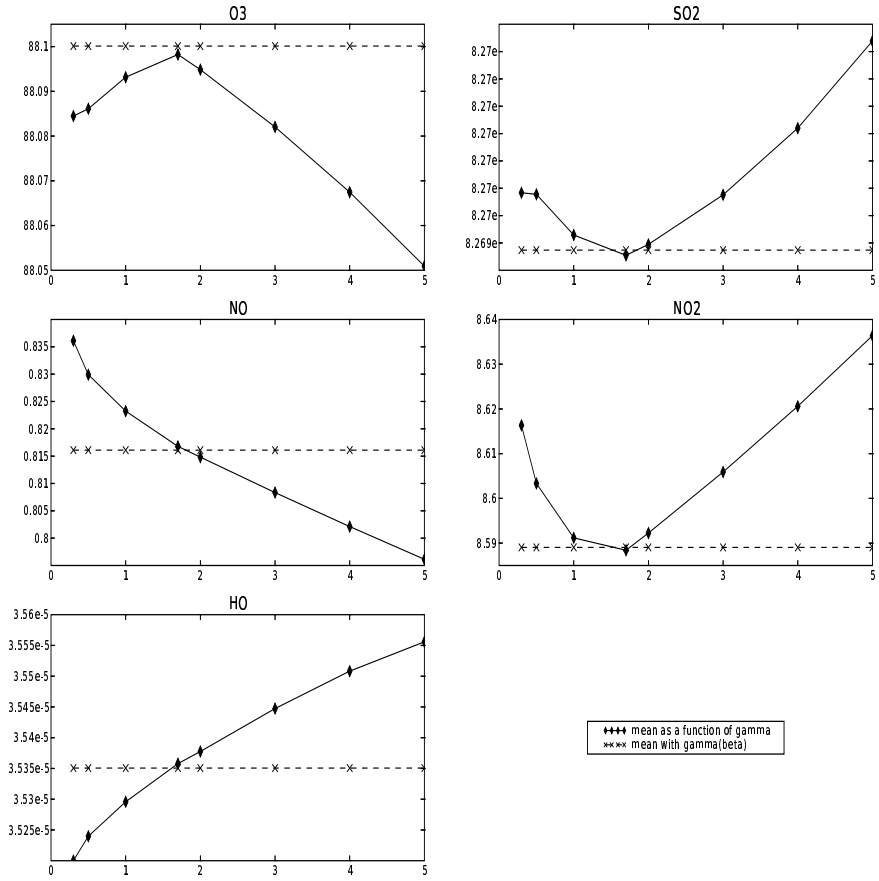

Figure 48: Concentrations mean ($\mu g \cdot m^{-3}$) as a function of γ for O_3, SO_2, NO, NO_2 and HO with $\Delta t = 600$ s

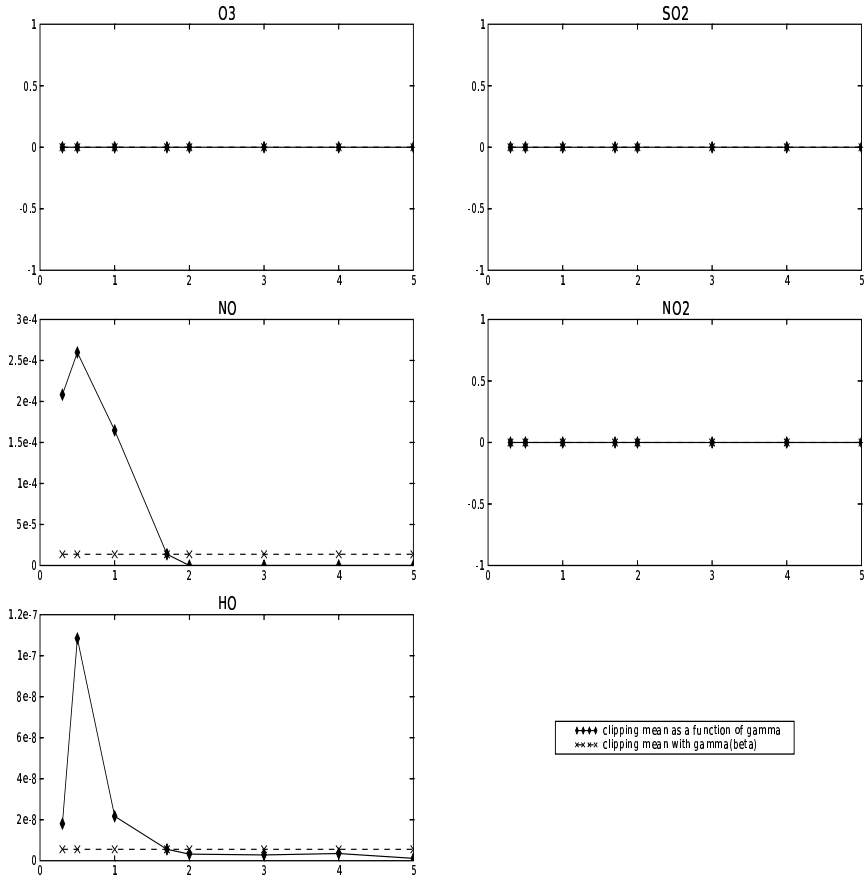

Figure 49: Clipping concentrations mean ($\mu g \cdot m^{-3}$) as a function of γ for O_3, SO_2, NO, NO_2 and HO with $\Delta t = 600$ s

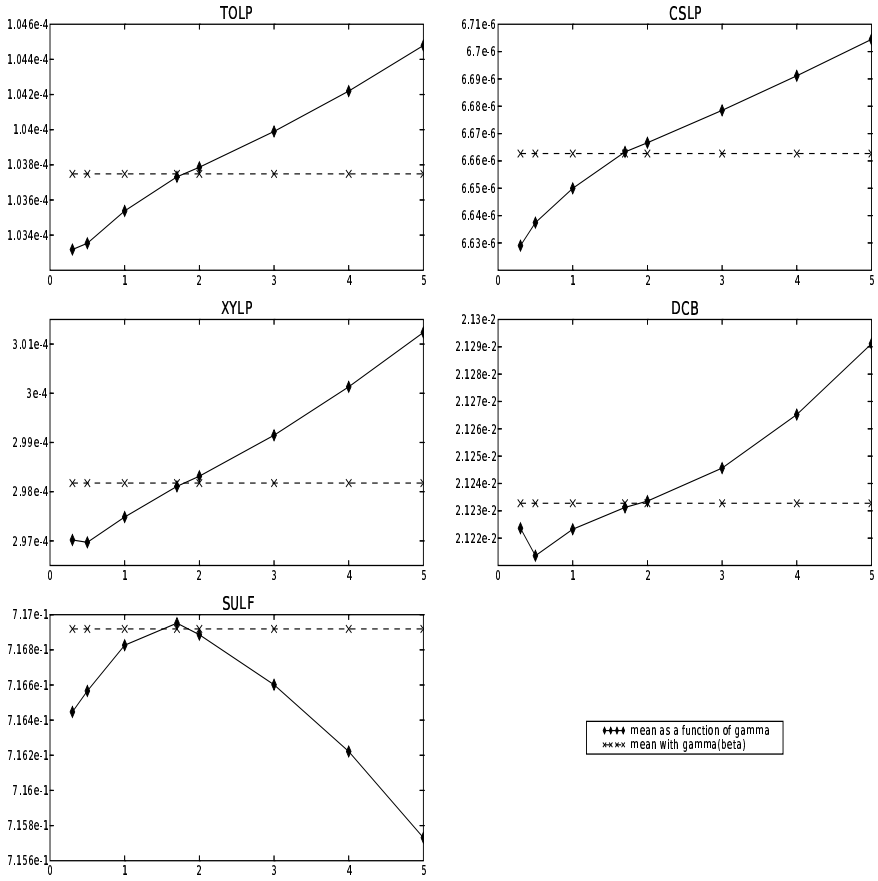

Figure 50: Concentrations mean ($\mu g \cdot m^{-3}$) as a function of γ for TOLP, CSLP, XYLP, DCB and SULF with $\Delta t = 600$ s

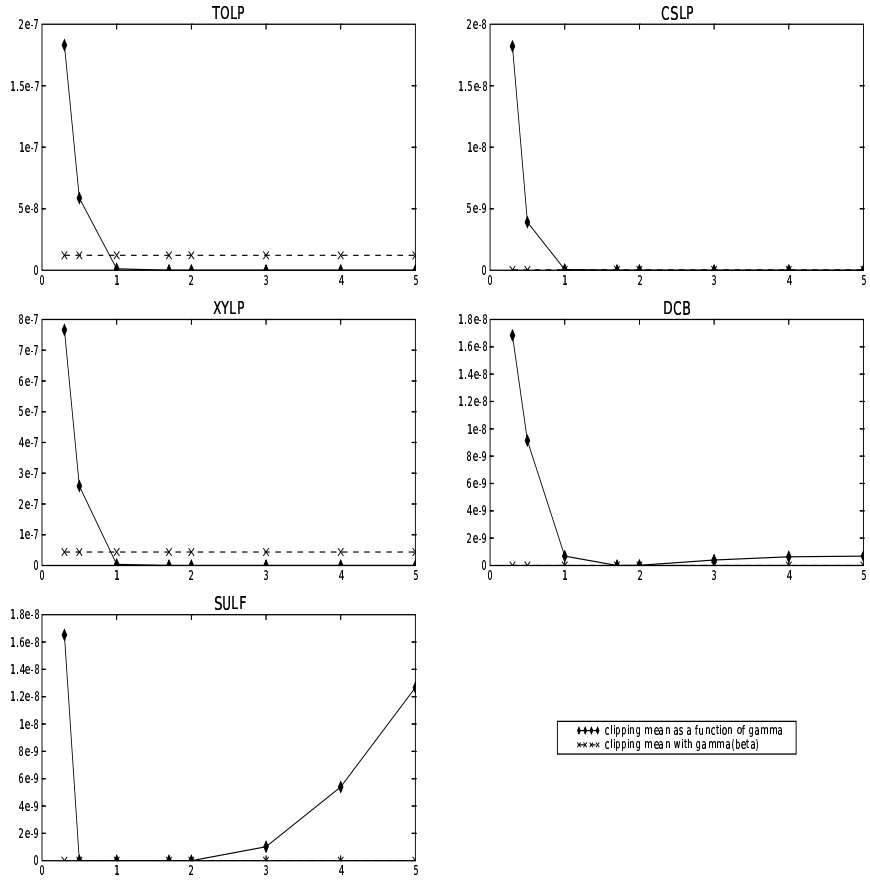

Figure 51: Clipping concentrations mean ($\mu g \cdot m^{-3}$) as a function of γ for TOLP, CSLP, XYLP, DCB and SULF with $\Delta t = 600$ s

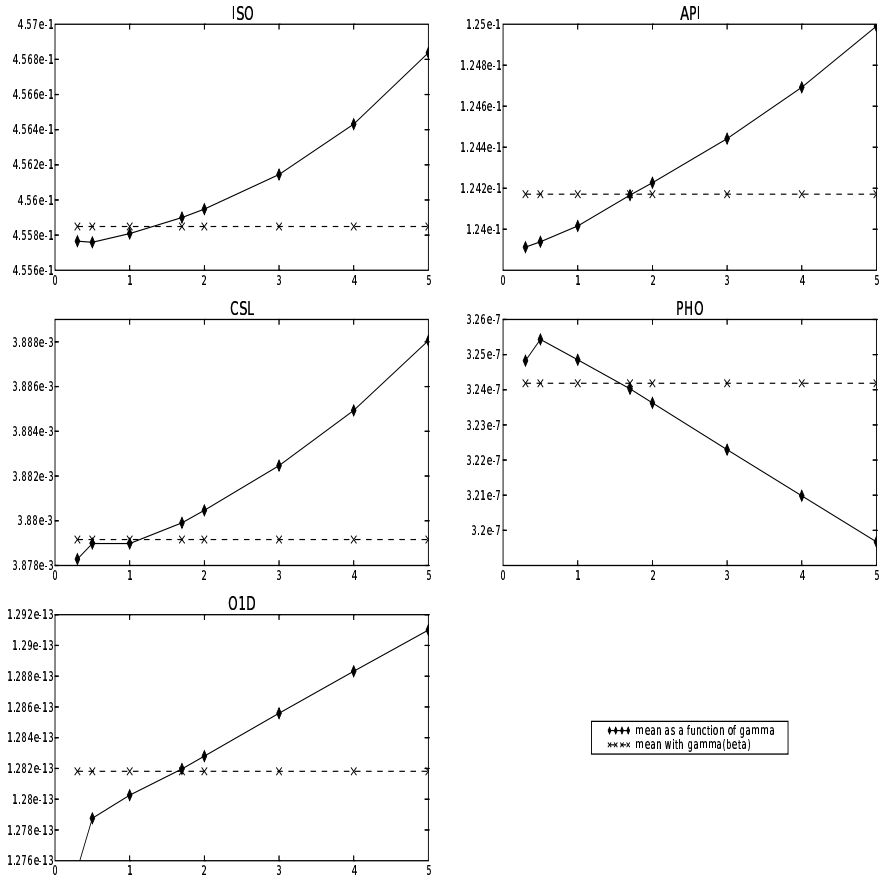

Figure 52: Concentrations mean ($\mu g \cdot m^{-3}$) as a function of γ for ISO, API, CSL, PHO and O_1D with $\Delta t = 600$ s

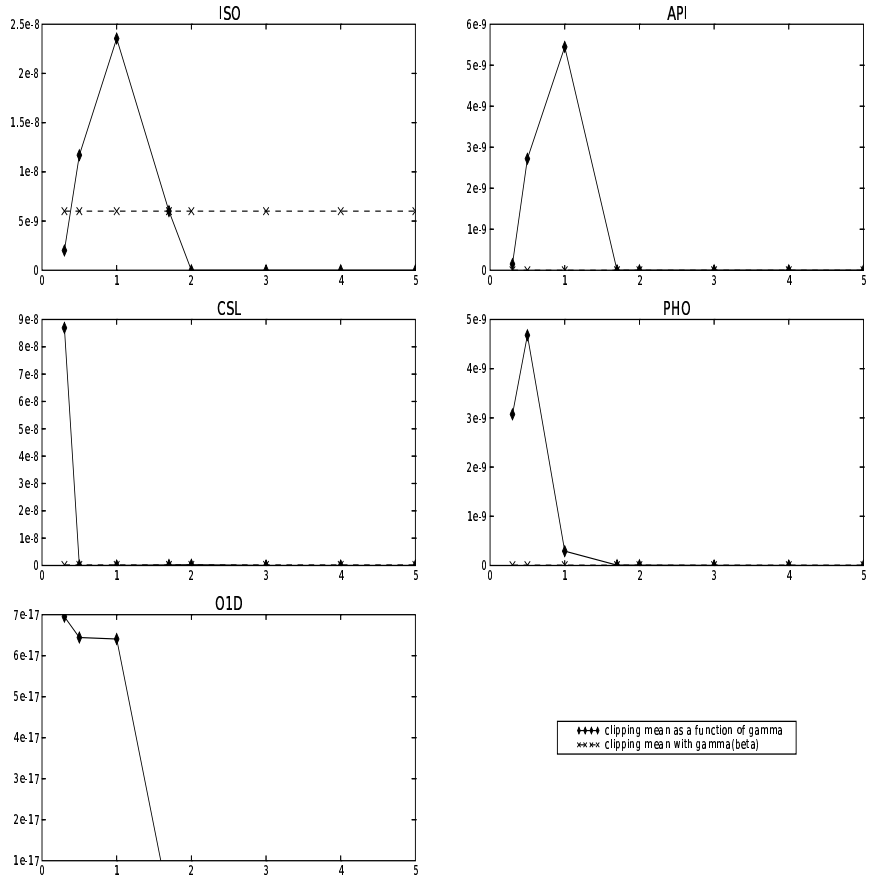

Figure 53: Clipping concentrations mean ($\mu g \cdot m^{-3}$) as a function of γ for ISO, API, CSL, PHO and O_1D with $\Delta t = 600$ s

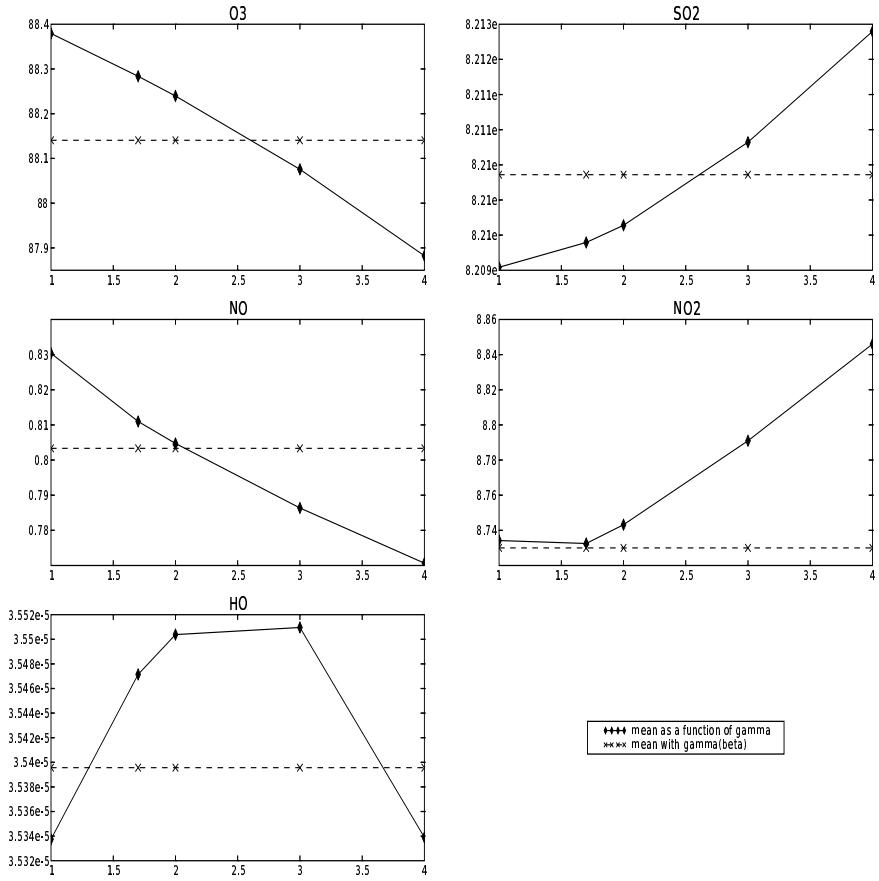

Figure 54: Concentrations mean ($\mu g \cdot m^{-3}$) as a function of γ for O_3, SO_2, NO, NO_2 and HO with $\Delta t = 1800$ s

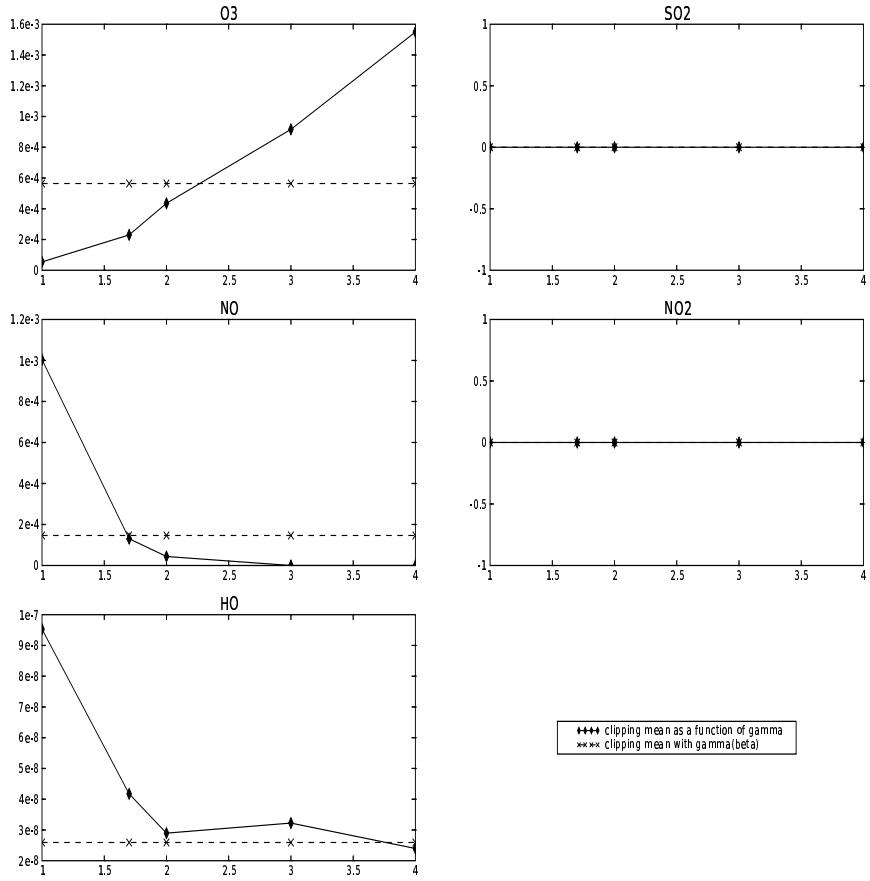

Figure 55: Clipping concentrations mean ($\mu g \cdot m^{-3}$) as a function of γ for O_3, SO_2, NO, NO_2 and HO with $\Delta t = 1800$ s

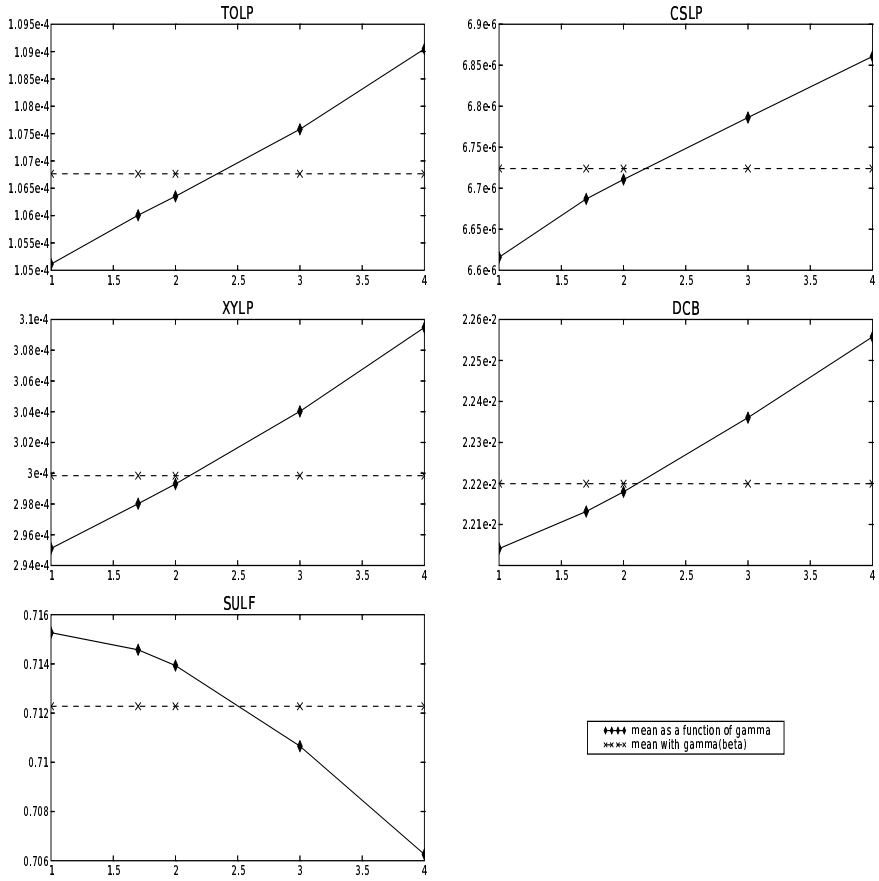

Figure 56: Concentrations mean ($\mu g \cdot m^{-3}$) as a function of γ for TOLP, CSLP, XYLP, DCB and SULF with $\Delta t = 1800$ s

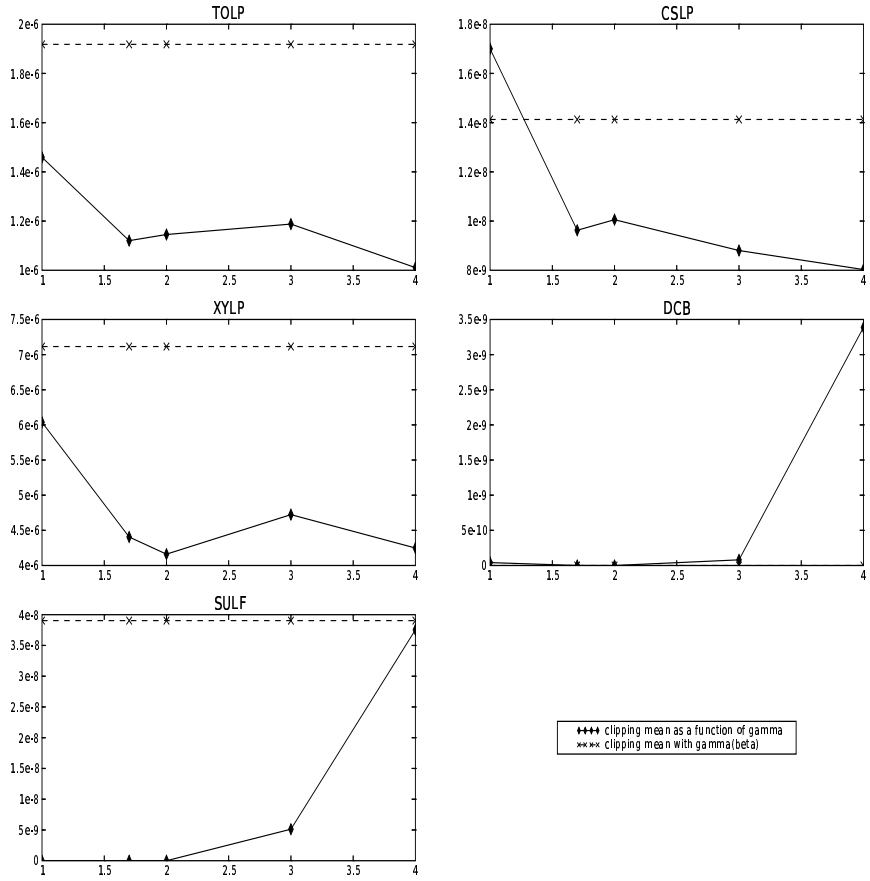

Figure 57: Clipping concentrations mean ($\mu g \cdot m^{-3}$) as a function of γ for TOLP, CSLP, XYLP, DCB and SULF with $\Delta t = 1800$ s

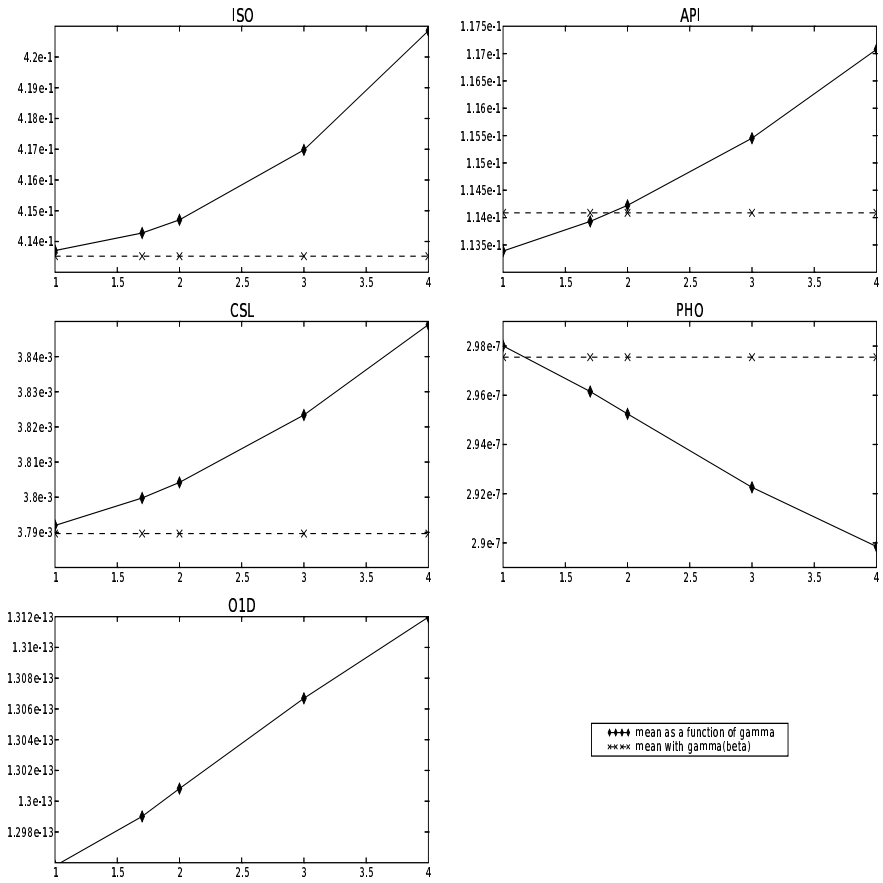

Figure 58: Concentrations mean ($\mu g \cdot m^{-3}$) as a function of γ for ISO, API, CSL, PHO and O_1D with $\Delta t = 1800$ s

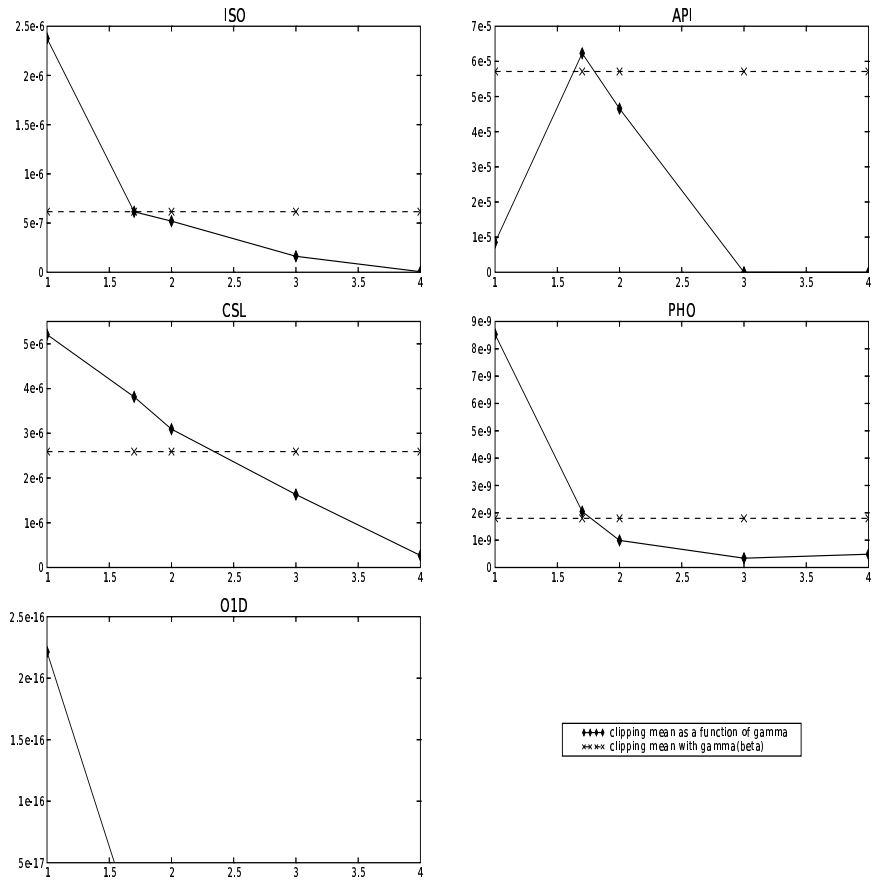

Figure 59: Clipping concentrations mean ($\mu g \cdot m^{-3}$) as a function of γ for ISO, API, CSL, PHO and O_1D with $\Delta t = 1800$ s

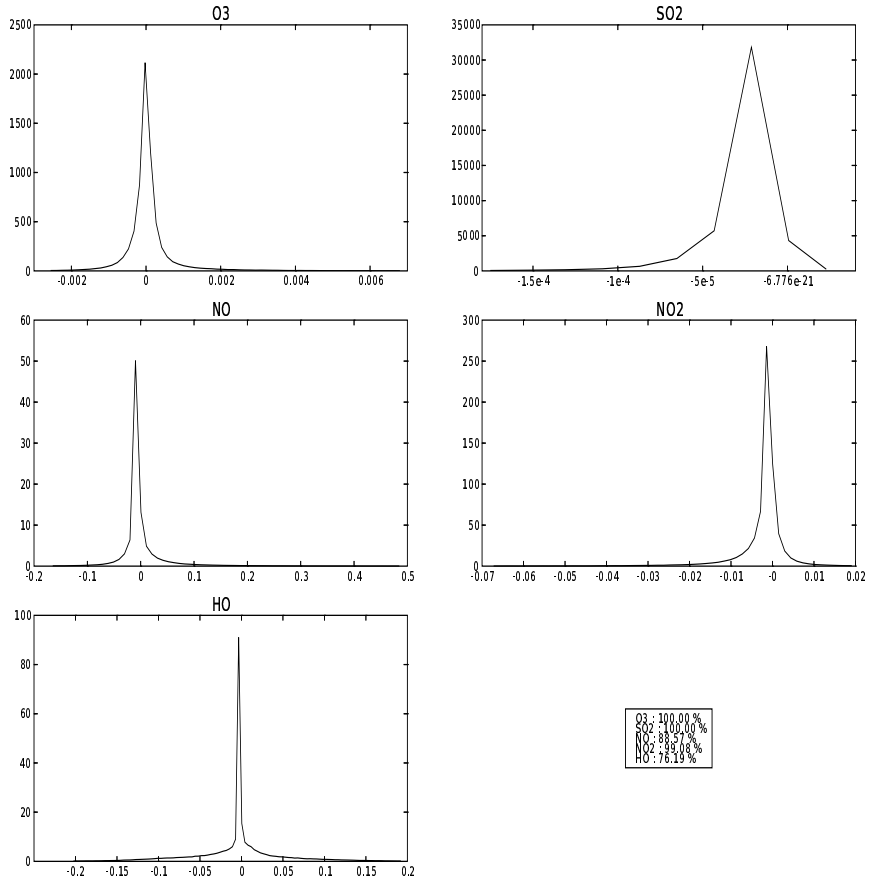

Figure 60: PDF of error between $\gamma = 1 + \frac{\sqrt{2}}{2}$ and $\gamma = 3$ with $\Delta t = 600$ s

5 Advection algorithms

5.1 Advection scheme

We want to estimate the sensitivity of POLAIR3D to its advection scheme. Therefore, we test it on a continental case over one week with an Upwind scheme:

$$F_{i+\frac{1}{2}} = \begin{cases} \nu_{i+\frac{1}{2}} c_i & \text{if } u_{i+\frac{1}{2}} \geq 0 \\ -\nu_{i+\frac{1}{2}} c_{i+1} & \text{if } u_{i+\frac{1}{2}} < 0 \end{cases} \tag{46}$$

and a third-order Direct Spatial Time (DST) scheme without flux-limiter ([7]):

$$F_{i+\frac{1}{2}} = \begin{cases} \nu_{i+\frac{1}{2}} (c_i + d_0 (\nu_{i+\frac{1}{2}})(c_{i+1} - c_i) + d_1 (\nu_{i+\frac{1}{2}})(c_i - c_{i-1})) & \text{if } u_{i+\frac{1}{2}} \geq 0 \\ -\nu_{i+\frac{1}{2}} (c_{i+1} + d_0 (\nu_{i+\frac{1}{2}})(c_i - c_{i+1}) + d_1 (\nu_{i+\frac{1}{2}})(c_{i+1} - c_{i+2})) & \text{if } u_{i+\frac{1}{2}} < 0. \end{cases} \tag{47}$$

As seen in figure 62, the advection scheme does not have any impact on the mean. Figures 67 and 68 also seem to indicate that locally, the advection scheme does not a very strong impact. However, we can see slight differences in figures 61 and 63. As expected, the Upwind scheme introduces numerical diffusion that leads to smaller peaks. On the other hand, a third-order scheme is less diffusive (the one without flux limiter is the least diffusive), but may introduce oscillations (even though the flux limiter limits them), and therefore, positivity of the results is not guaranteed (in order to be sure there will not be any problems with chemistry, POLAIR3D sets every negative concentration to 0, but then mass conservation is lost). Figure 61 illustrates that, with an Upwind scheme, the peaks of concentrations can be up to 9% smaller than with a third-order scheme without flux limiter as far as O_3 is concerned, 18% for SO_2, 19% for NO and 17% for NO_2. The concentrations' standard deviation is lowered up to 25% of its value with a no limiter DST3 when an Upwind scheme is used for O_3, 14% for SO_2 and 25% for NO as shown in figure 63. This clearly indicates that an Upwind scheme is not useable for maximal values (as expected).

However, these values (figures 61–68) were obtained with a turbulent diffusion coefficient K_H equal to 50 000 $m^2 \cdot s^{-1}$, which is quite high. Therefore, this may reduce the impact of numerical diffusion. That is why the same comparisons have been runned with other turbulent diffusion coefficients: 0 $m^2 \cdot s^{-1}$ and 10 000 $m^2 \cdot s^{-1}$.

When $K_H = 0$ or $K_H = 10000$ $m^2.s^{-1}$, the advection scheme can be quite decisive. The advection scheme does have an impact whatever the diffusive coefficient is, but when K_H is too important, then the numerical diffusion is hidden by the physical diffusion (as expected).

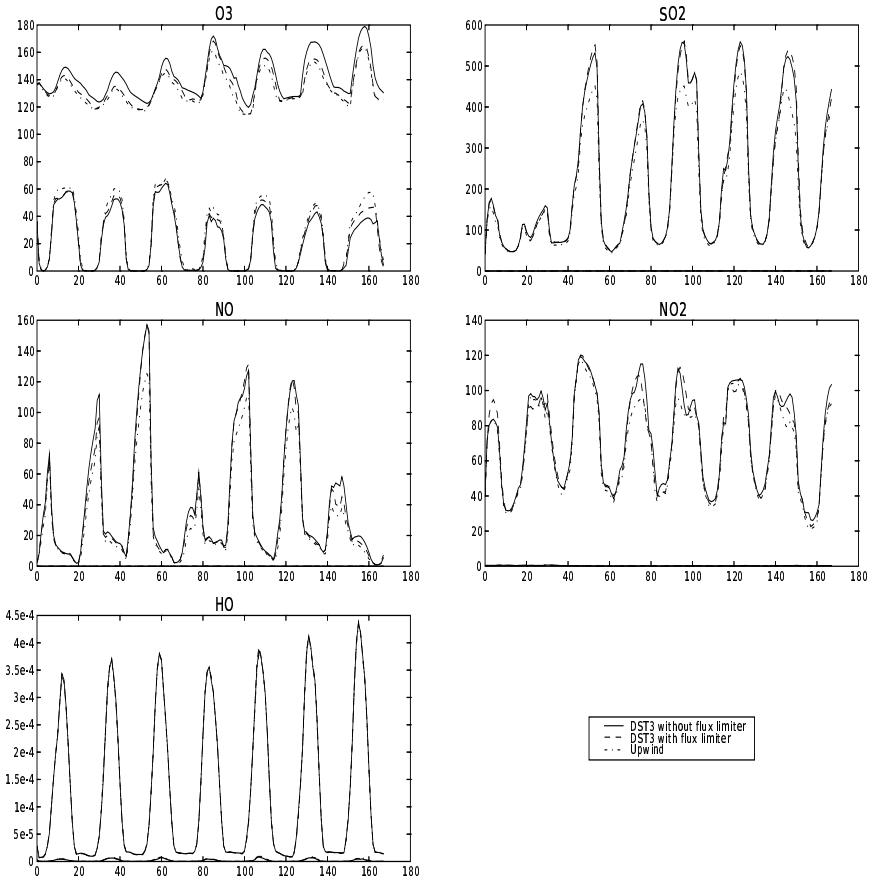

Figure 61: Time evolution of the spatial minimum and maximum ($\mu g \cdot m^{-3}$) when $K_H = 50000\ m^2.s^{-1}$ for different advection schemes

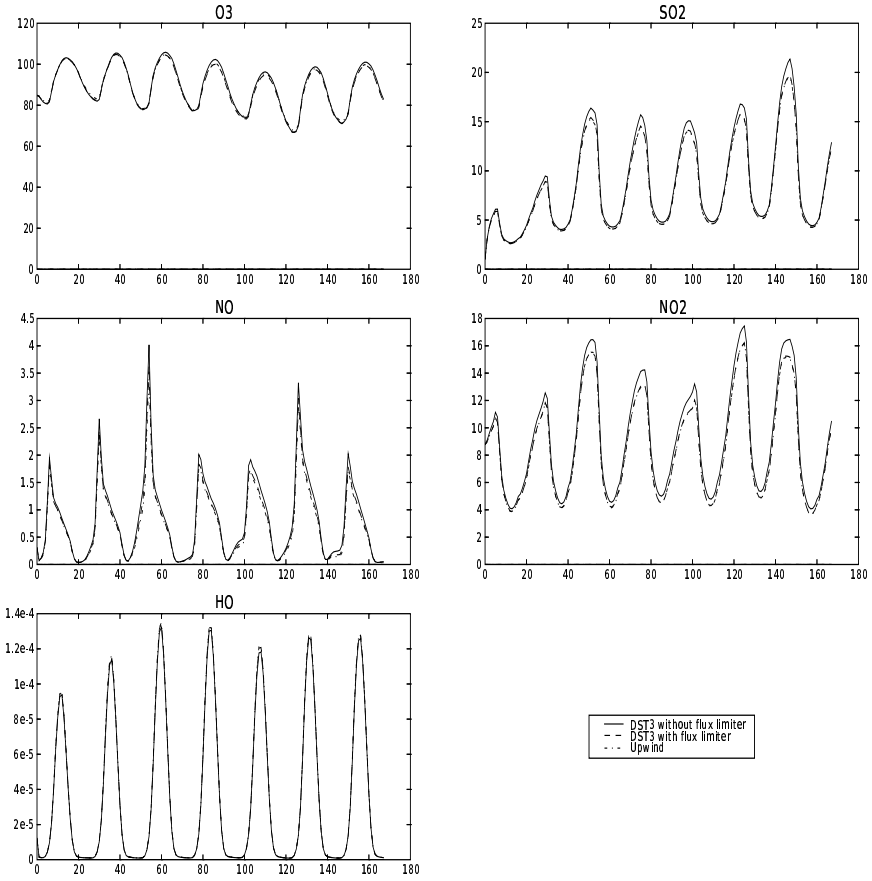

Figure 62: Time evolution of the spatial mean ($\mu g \cdot m^{-3}$) when $K_H = 50000\ m^2.s^{-1}$ for different advection schemes

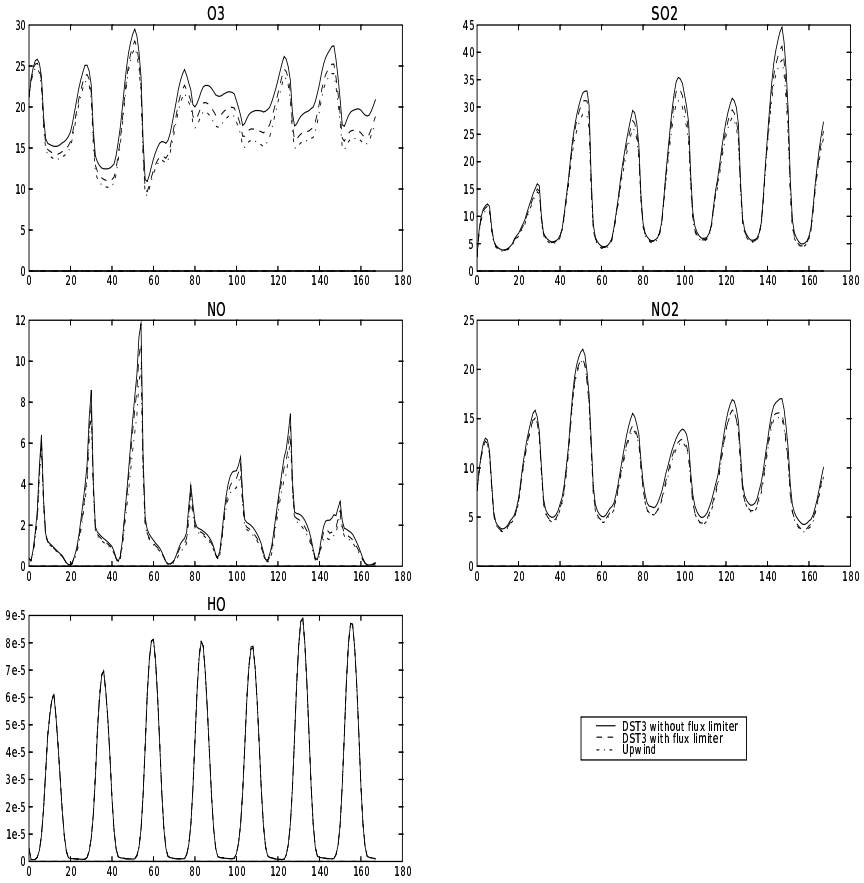

Figure 63: Time evolution of the spatial standard deviation ($\mu g \cdot m^{-3}$) when $K_H = 50000\ m^2.s^{-1}$ for different advection schemes

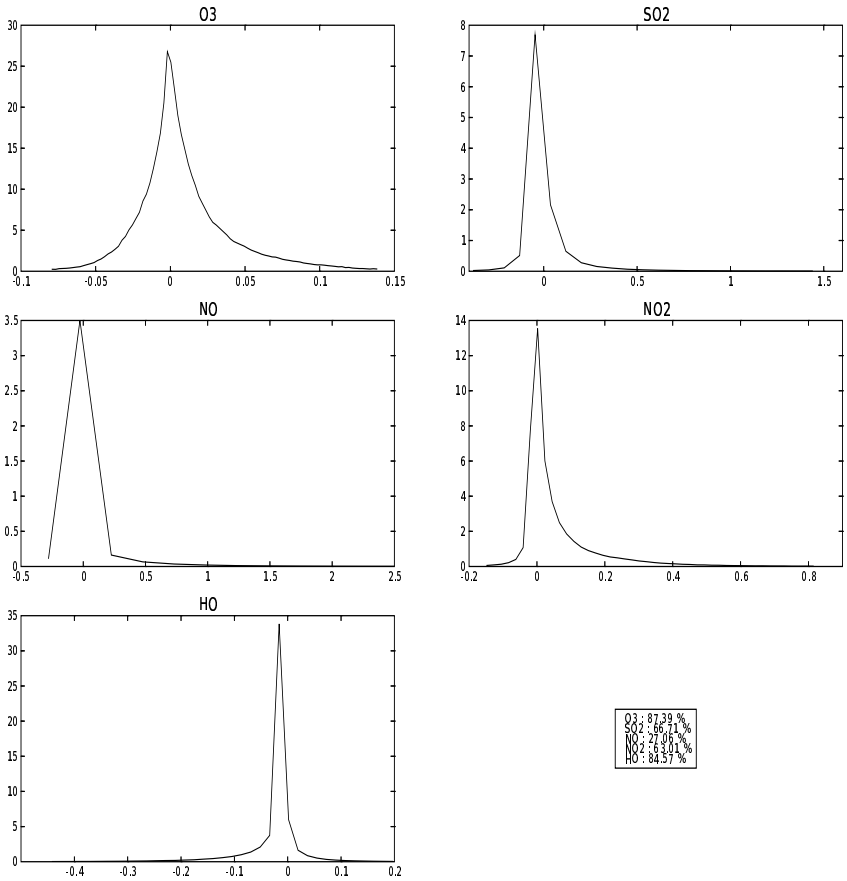

Figure 64: PDF of error between DST3 with flux limiter and without flux limiter for a continental simulation

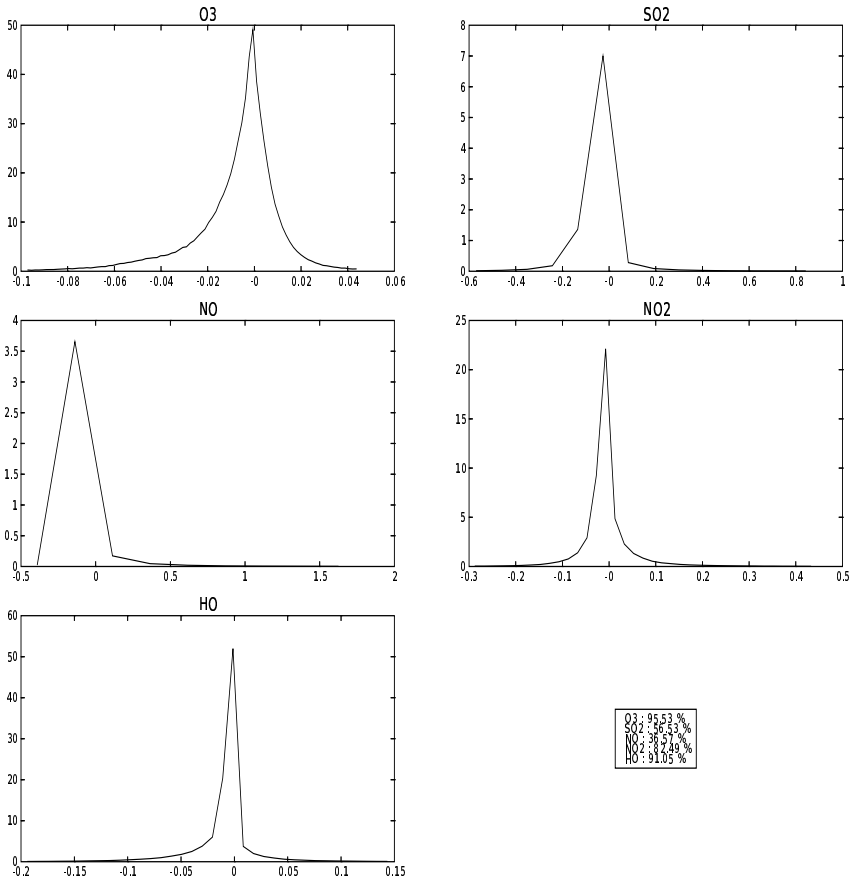

Figure 65: PDF of error between DST3 with flux limiter and upwind for a continental simulation

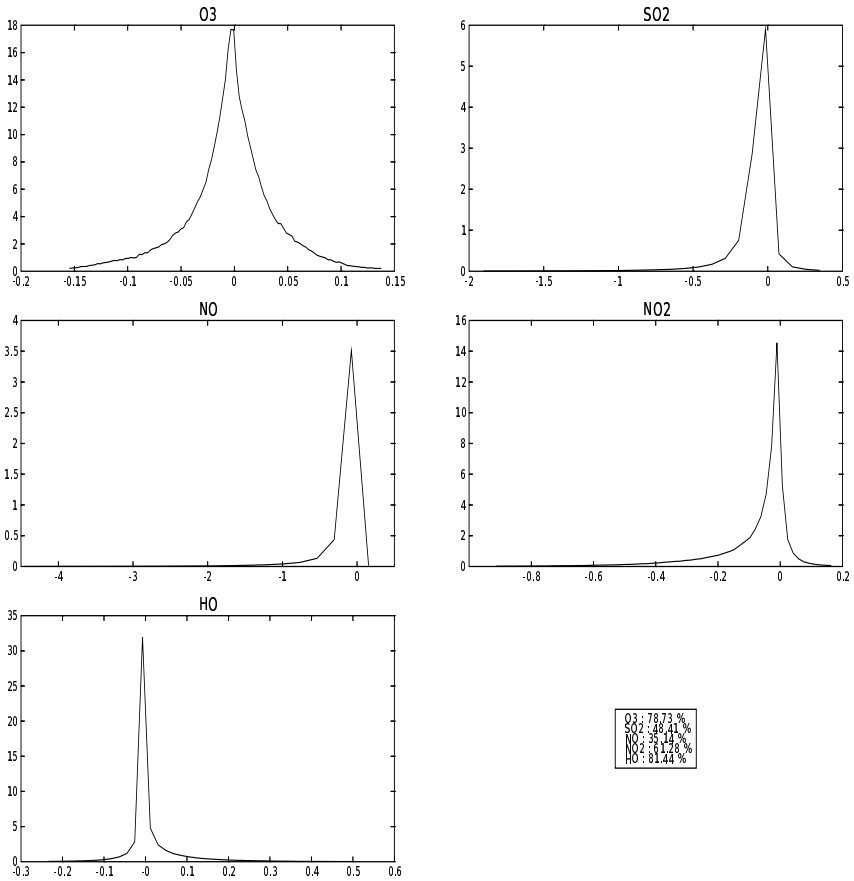

Figure 66: PDF of error between DST3 without flux limiter and upwind for a continental simulation

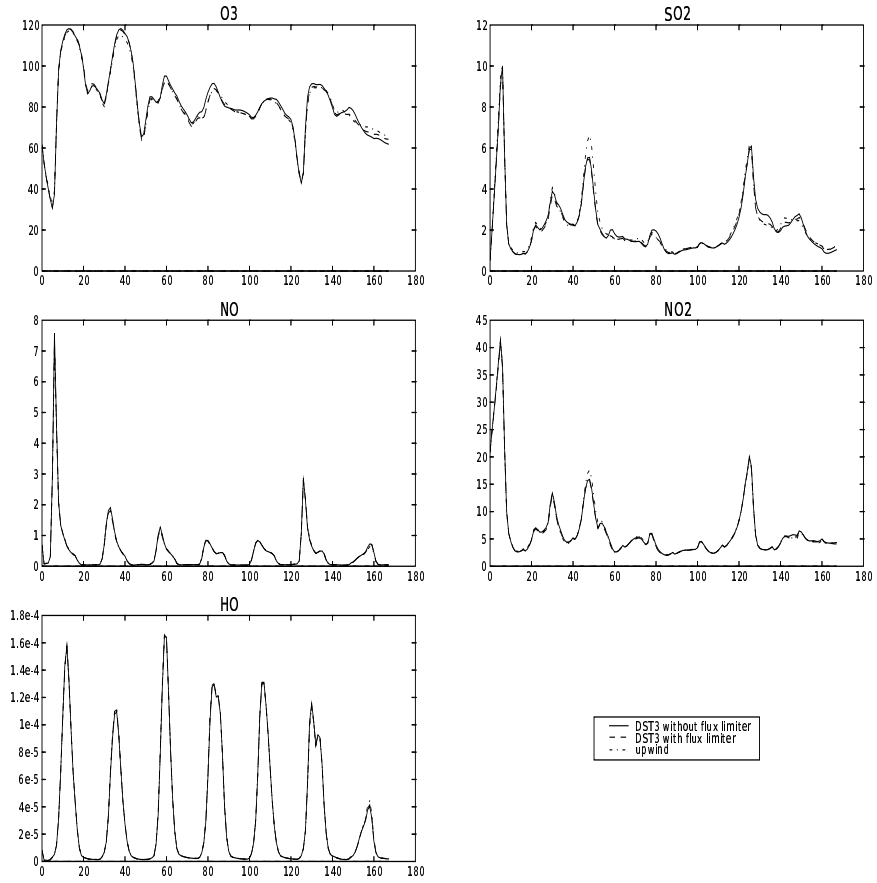

Figure 67: Time evolution of the concentrations ($\mu g \cdot m^{-3}$) over Paris when $K_H = 50000\ m^2.s^{-1}$ for different advection schemes

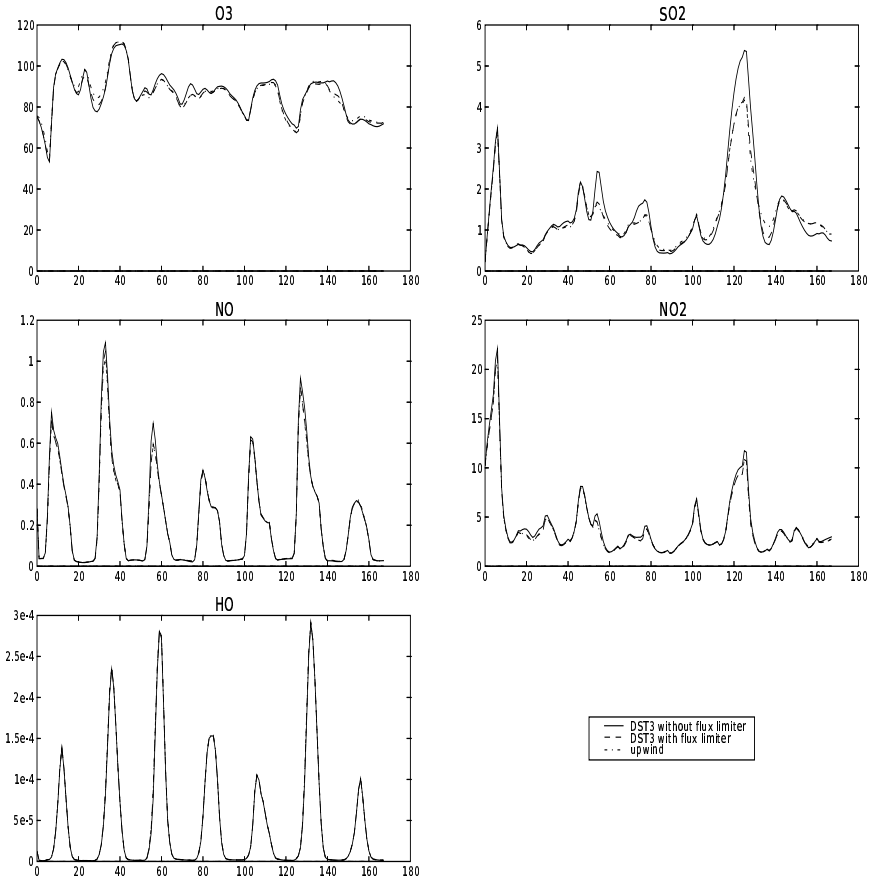

Figure 68: Time evolution of the concentrations ($\mu g \cdot m^{-3}$) over Pontarlier when $K_H = 50000\ m^2.s^{-1}$ for different advection schemes

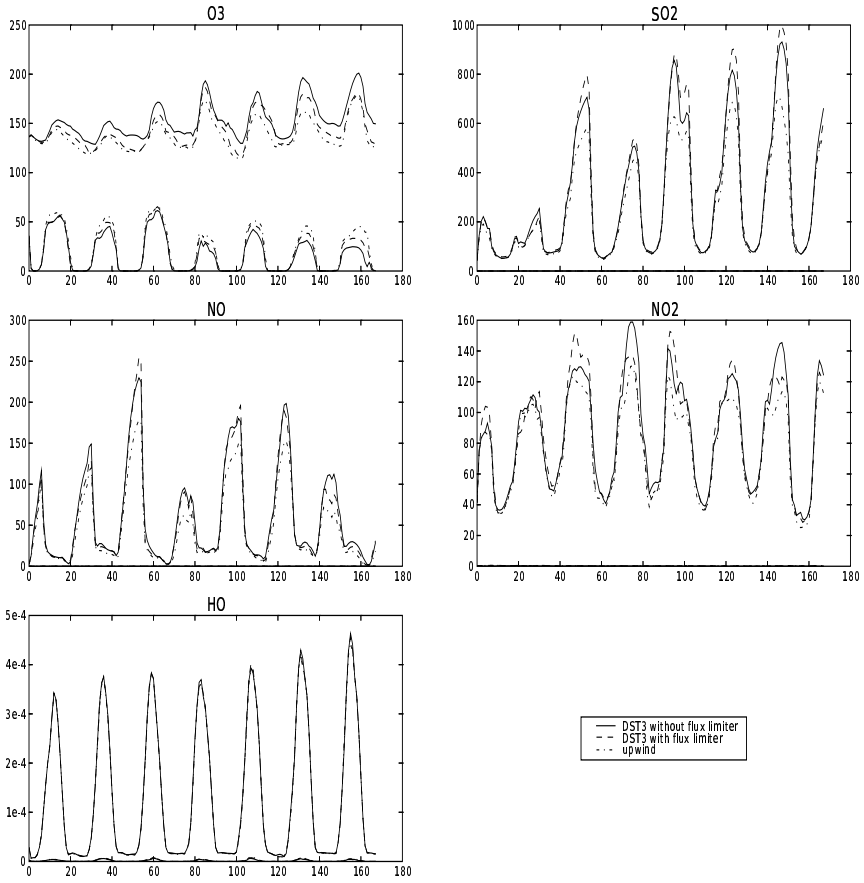

Figure 69: Time evolution of the spatial minimum and maximum ($\mu g \cdot m^{-3}$) when $K_H = 0\ m^2.s^{-1}$ for different advection schemes

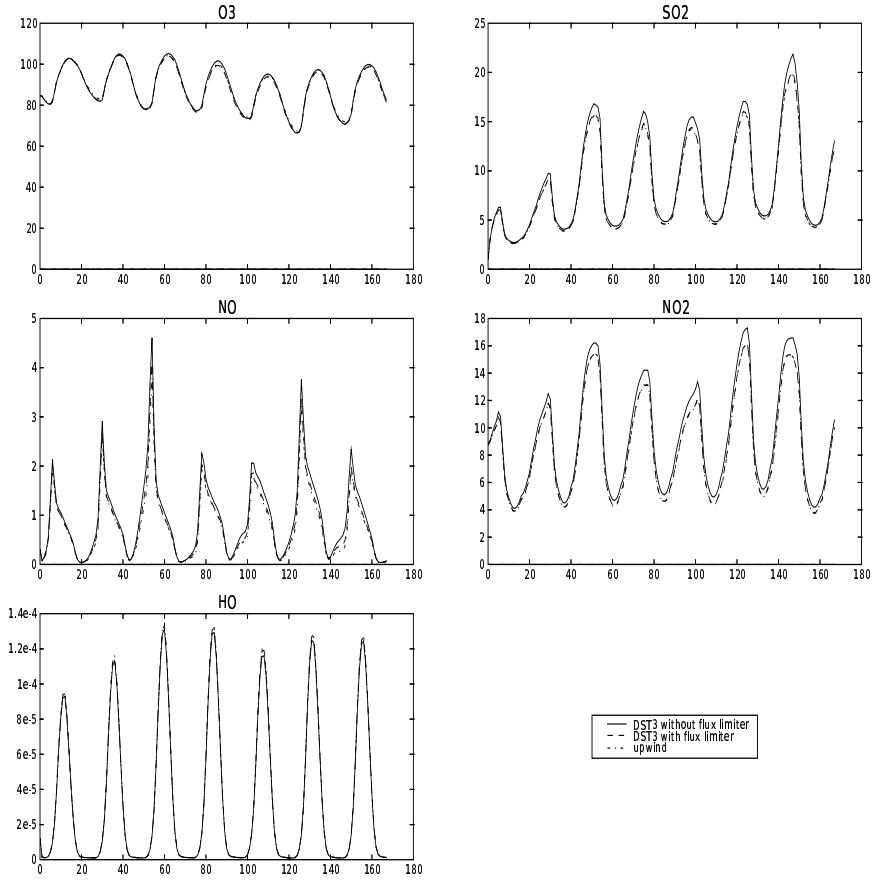

Figure 70: Time evolution of the spatial mean ($\mu g \cdot m^{-3}$) when $K_H = 0\ m^2.s^{-1}$ for different advection schemes

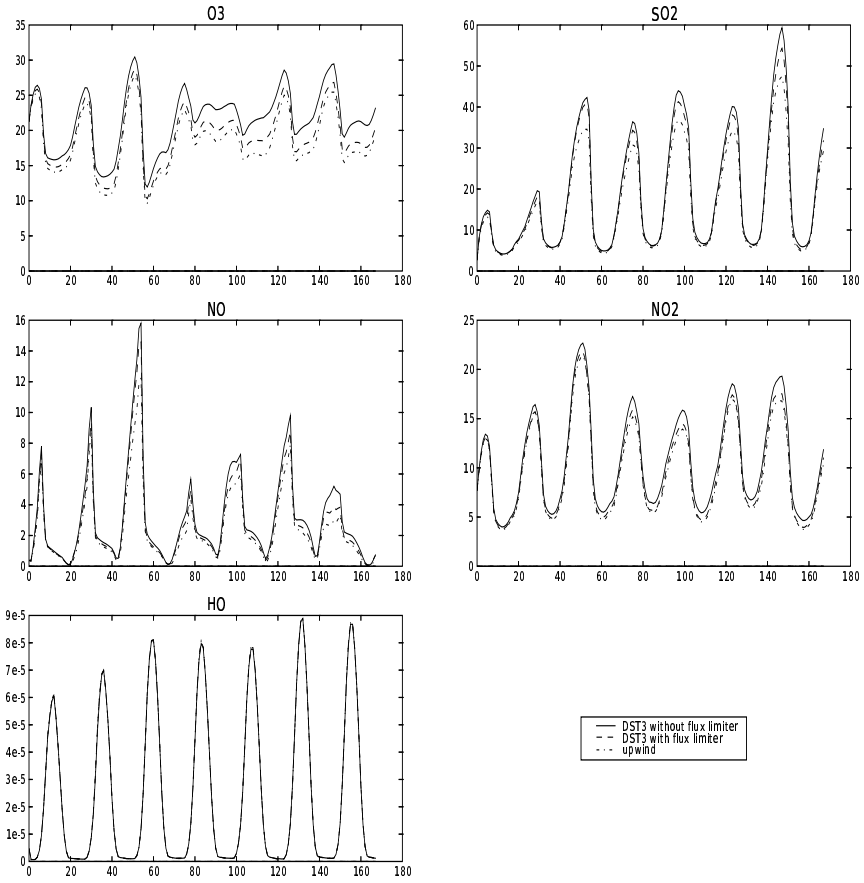

Figure 71: Time evolution of the spatial standard deviation ($\mu g \cdot m^{-3}$) when $K_H = 0\ m^2.s^{-1}$ for different advection schemes

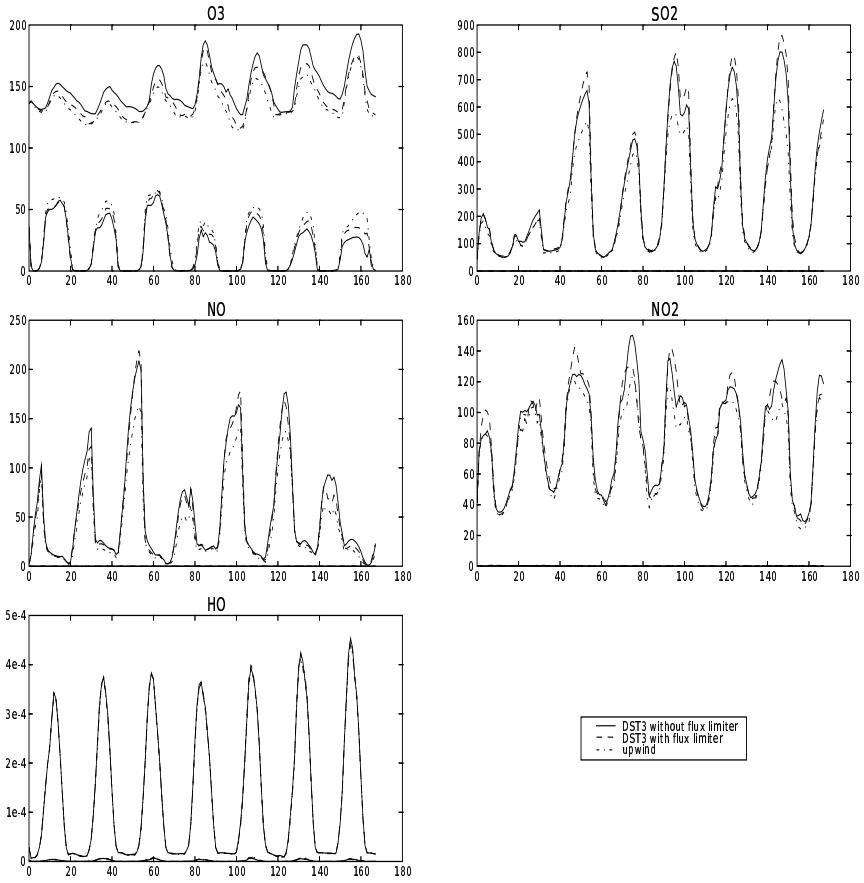

Figure 72: Time evolution of the spatial minimum and maximum ($\mu g \cdot m^{-3}$) when $K_H = 10000\ m^2.s^{-1}$ for different advection schemes

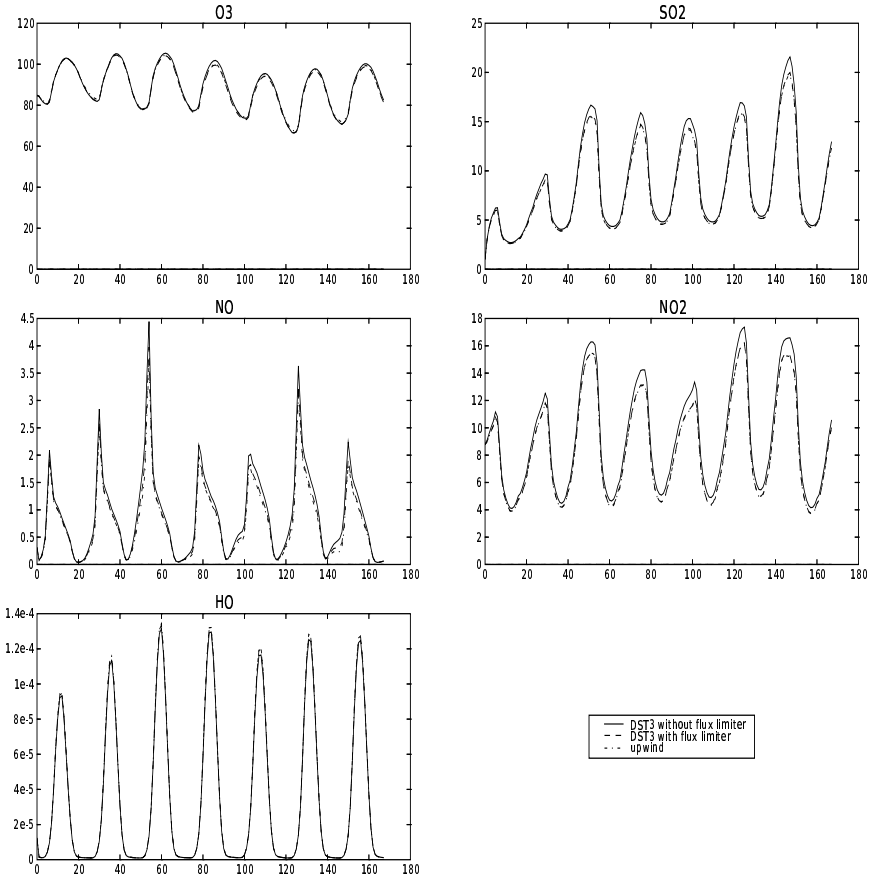

Figure 73: Time evolution of the spatial mean ($\mu g \cdot m^{-3}$) when $K_H = 10000\ m^2.s^{-1}$ for different advection schemes

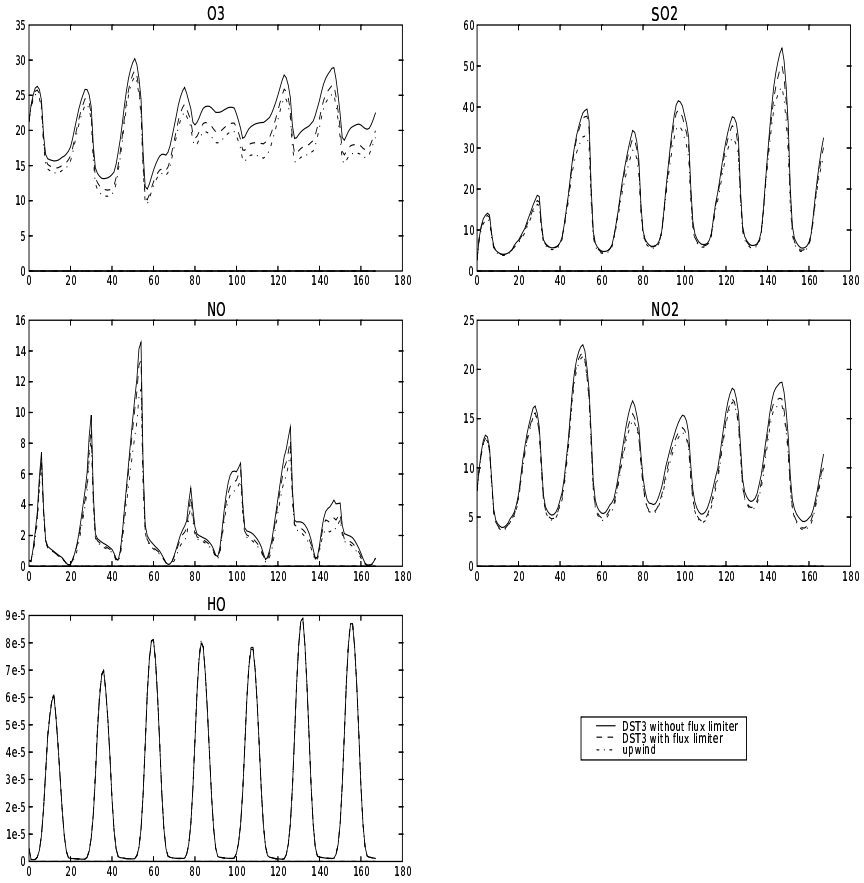

Figure 74: Time evolution of the spatial standard deviation ($\mu g \cdot m^{-3}$) when $K_H = 10000\ m^2.s^{-1}$ for different advection schemes

Besides, in terms of CPU time, the Upwind scheme is much more efficient. Therefore, it could be interesting to use an Upwind scheme in some cases (for examples, if we need the simulation to be fast) since the numerical diffusion introduced is quite negligible compared to physical diffusion.

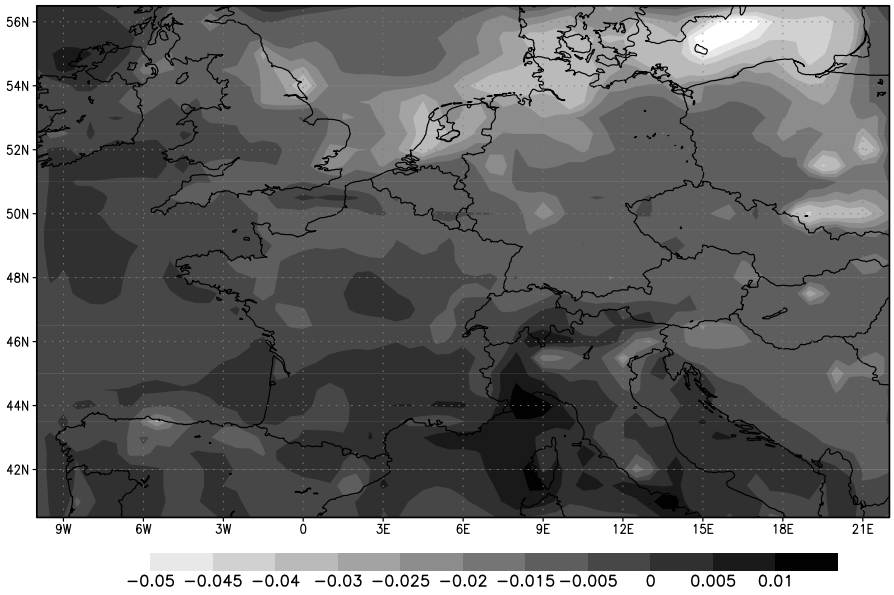

Figure 75: $\frac{mean(upwind)-mean(DST3withfluxlimiter)}{mean(DST3withfluxlimiter)}$ for O_3 with $K_H = 50000m^2.s^{-1}$

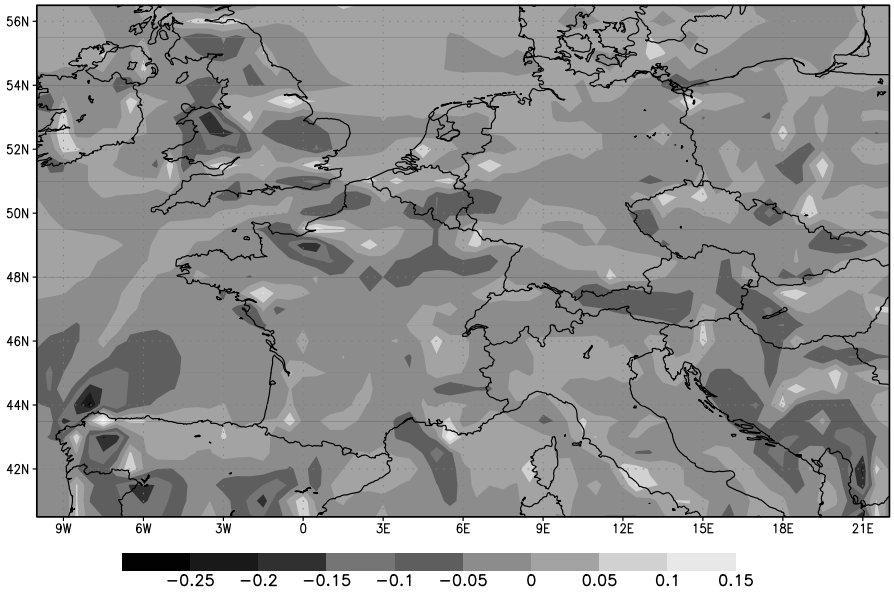

Figure 76: $\frac{mean(upwind)-mean(DST3withfluxlimiter)}{mean(DST3withfluxlimiter)}$ for SO_2 with $K_H = 50000m^2.s^{-1}$

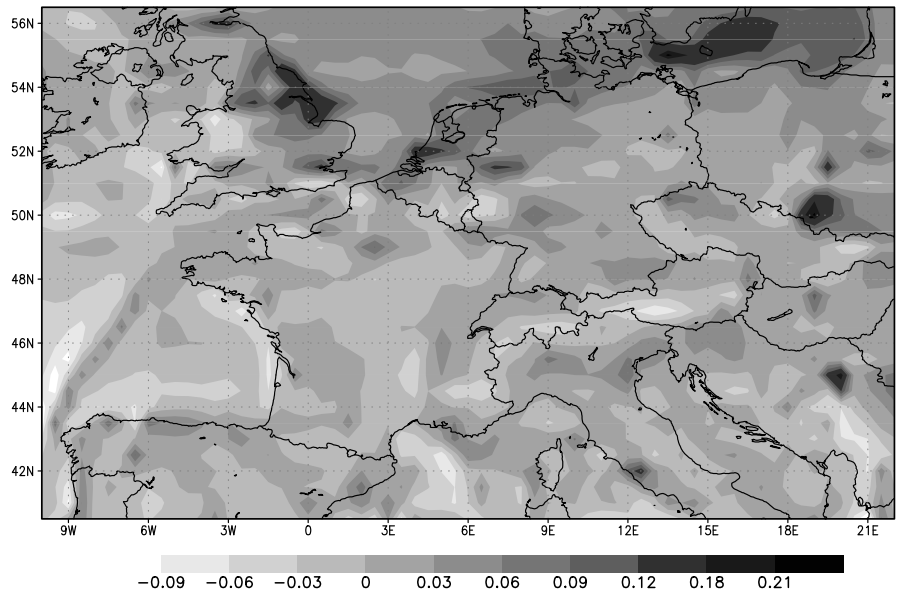

Figure 77: $\frac{mean(upwind)-mean(DST3withfluxlimiter)}{mean(DST3withfluxlimiter)}$ for NO with $K_H = 50000m^2.s^{-1}$

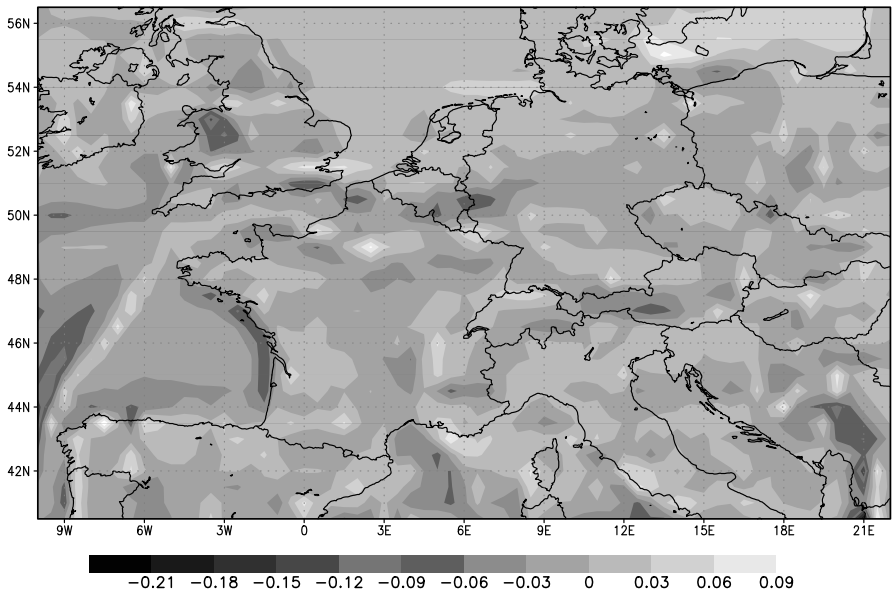

Figure 78: $\frac{mean(upwind)-mean(DST3withfluxlimiter)}{mean(DST3withfluxlimiter)}$ for NO_2 with $K_H = 50000m^2.s^{-1}$

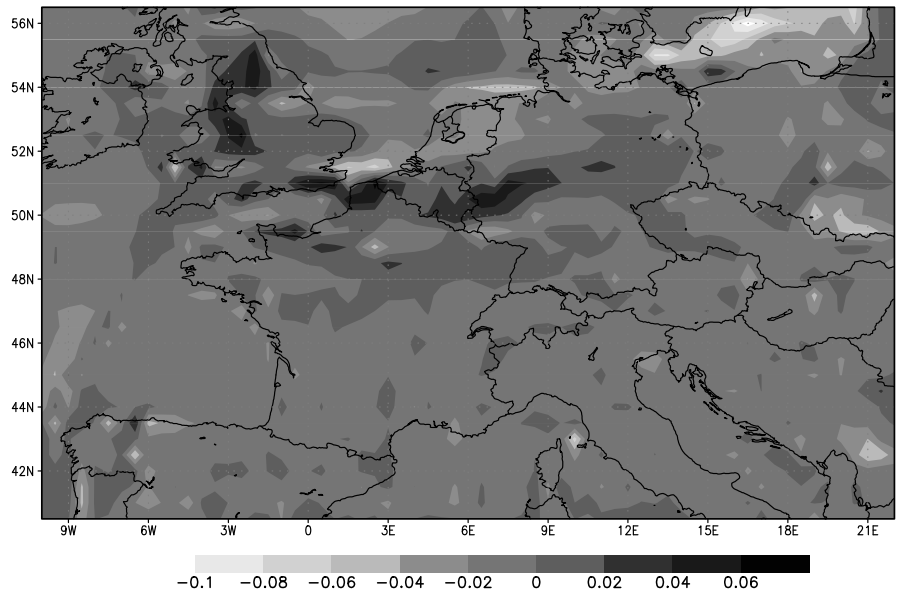

Figure 79: $\frac{mean(upwind)-mean(DST3withfluxlimiter)}{mean(DST3withfluxlimiter)}$ for HO with $K_H = 50000m^2.s^{-1}$

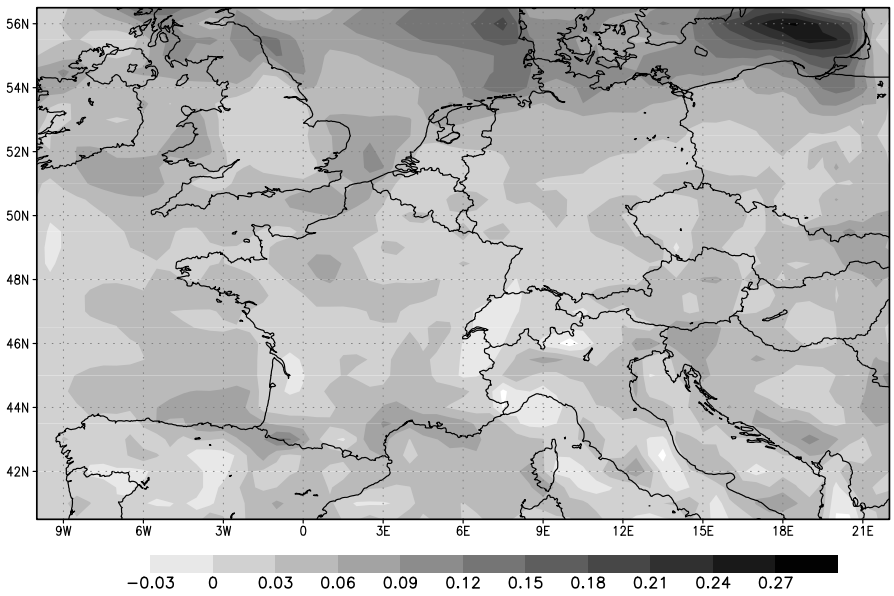

Figure 80: $\frac{\sigma(upwind)-\sigma(DST3withfluxlimiter)}{\sigma(DST3withfluxlimiter)}$ for O_3 with $K_H = 50000m^2.s^{-1}$

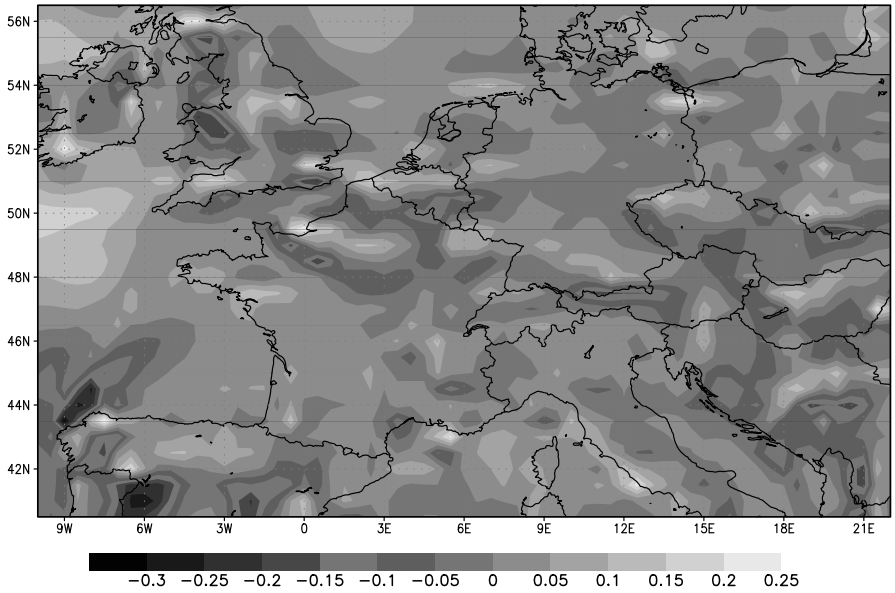

Figure 81: $\frac{\sigma(upwind)-\sigma(DST3withfluxlimiter)}{\sigma(DST3withfluxlimiter)}$ for SO_2 with $K_H = 50000m^2.s^{-1}$

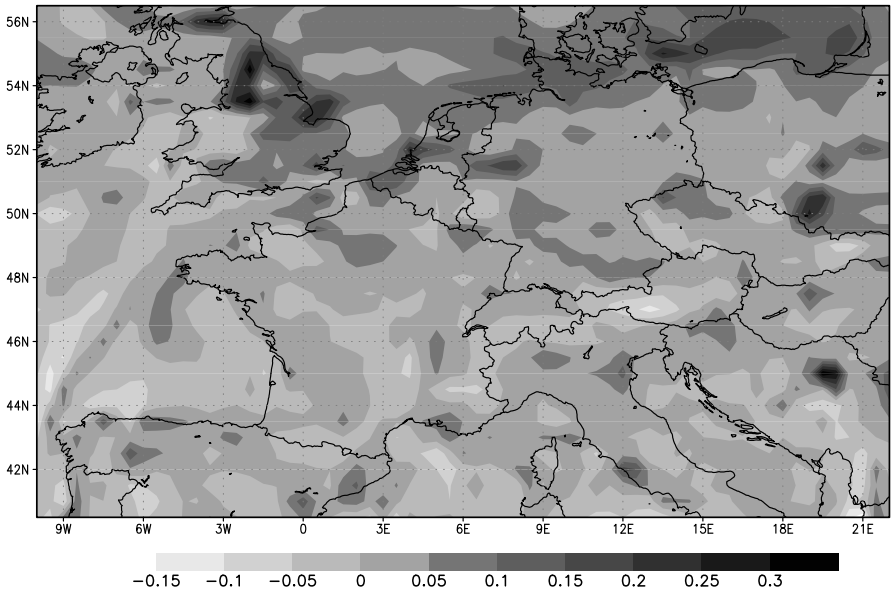

Figure 82: $\frac{\sigma(upwind)-\sigma(DST3withfluxlimiter)}{\sigma(DST3withfluxlimiter)}$ for NO with $K_H = 50000m^2.s^{-1}$

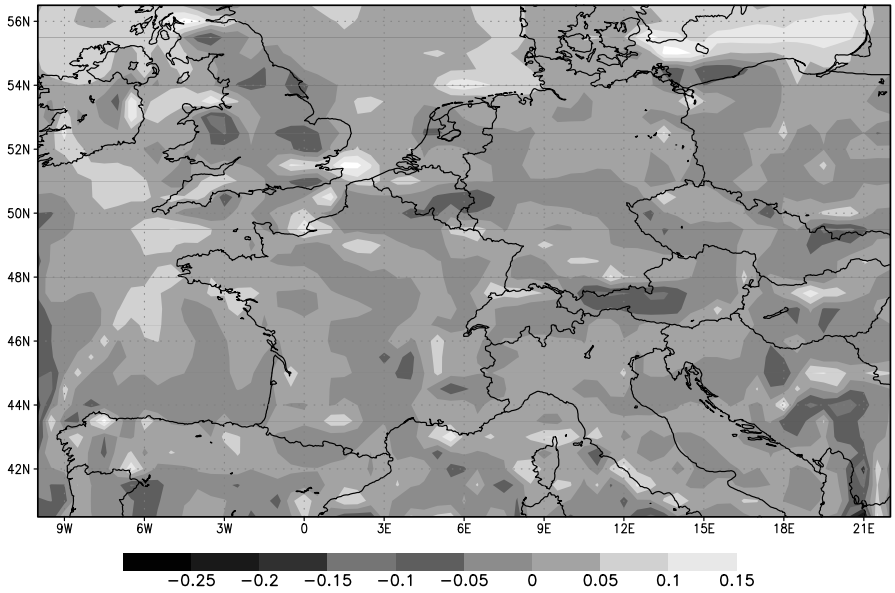

Figure 83: $\frac{\sigma(upwind)-\sigma(DST3withfluxlimiter)}{\sigma(DST3withfluxlimiter)}$ for NO_2 with $K_H = 50000m^2.s^{-1}$

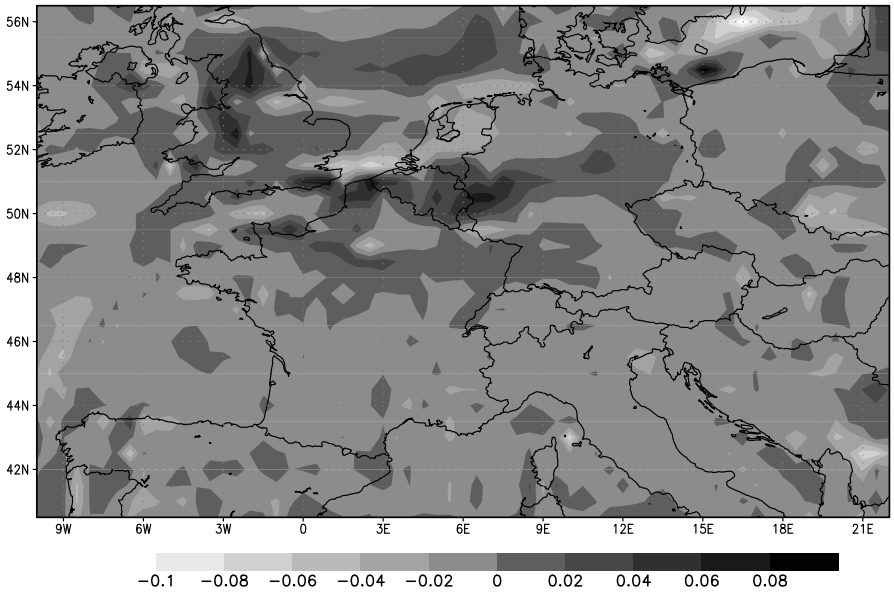

Figure 84: $\frac{\sigma(upwind)-\sigma(DST3withfluxlimiter)}{\sigma(DST3withfluxlimiter)}$ for HO with $K_H = 50000m^2.s^{-1}$

Figures 85–87 seem to indicate that the choice of advection scheme has an impact (even though no so strong) on a regional study, mainly on the standard deviation. The advection scheme does have an impact however on the simulation of the Chernobyl accident, as shown in figures 91–93.

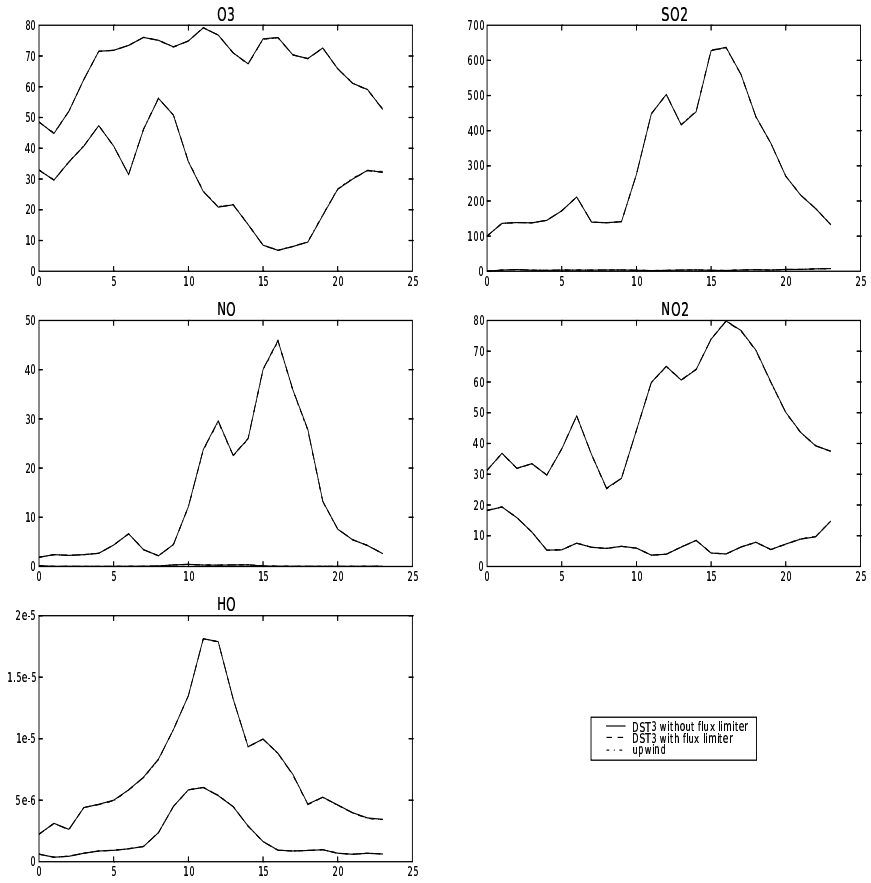

Figure 85: Time evolution of the spatial minimum and maximum ($\mu g \cdot m^{-3}$) over Lille for different advection schemes

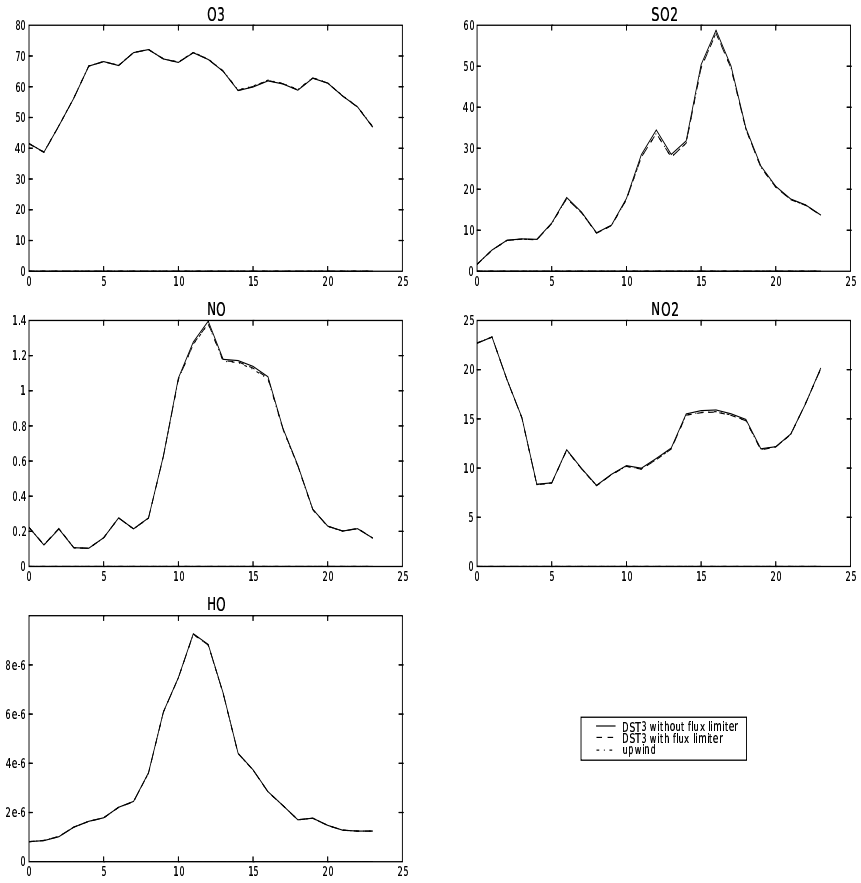

Figure 86: Time evolution of the spatial mean ($\mu g \cdot m^{-3}$) over Lille for different advection schemes

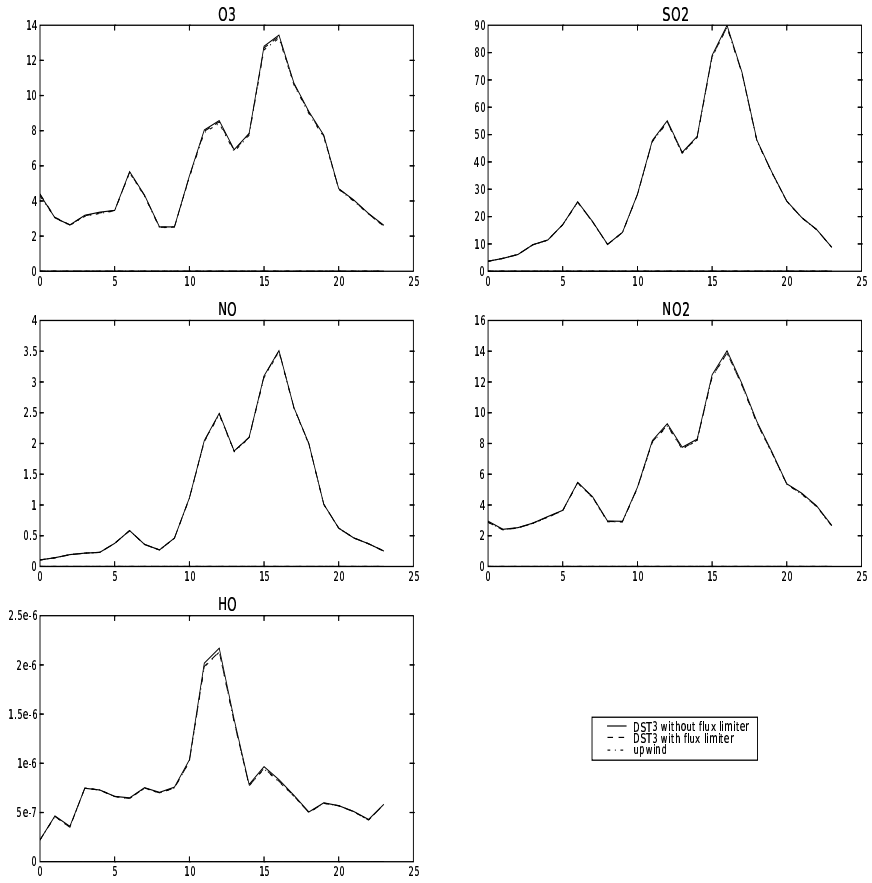

Figure 87: Time evolution of the spatial standard deviation ($\mu g \cdot m^{-3}$) over Lille for different advection schemes

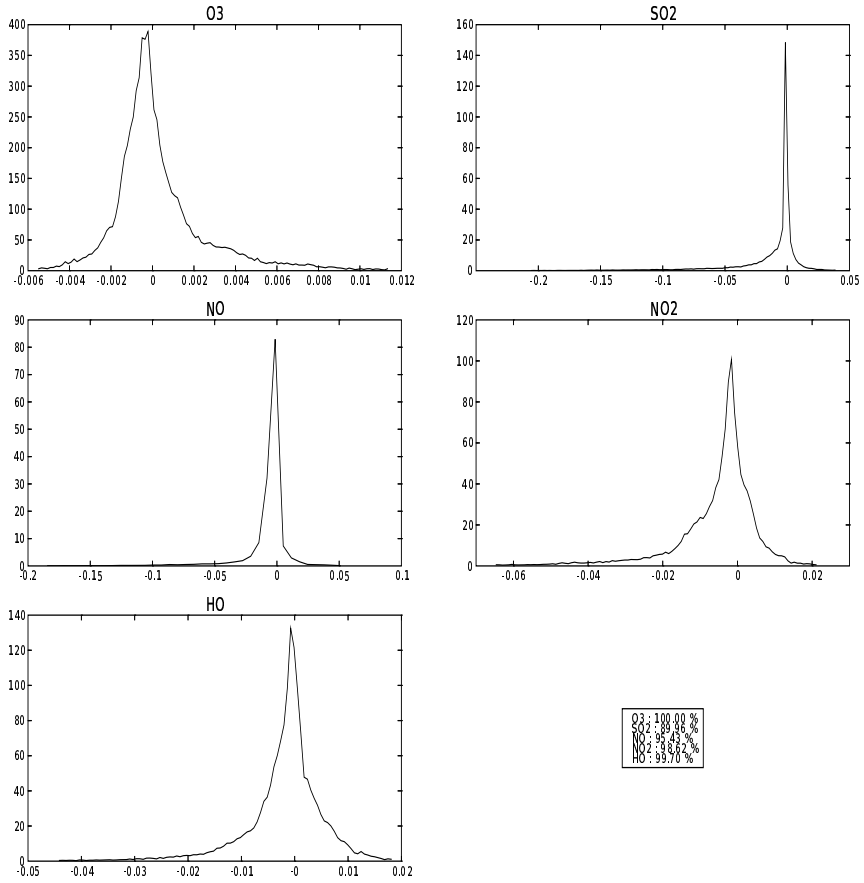

Figure 88: PDF of error between DST3 with flux limiter and without flux limiter for a regional simulation

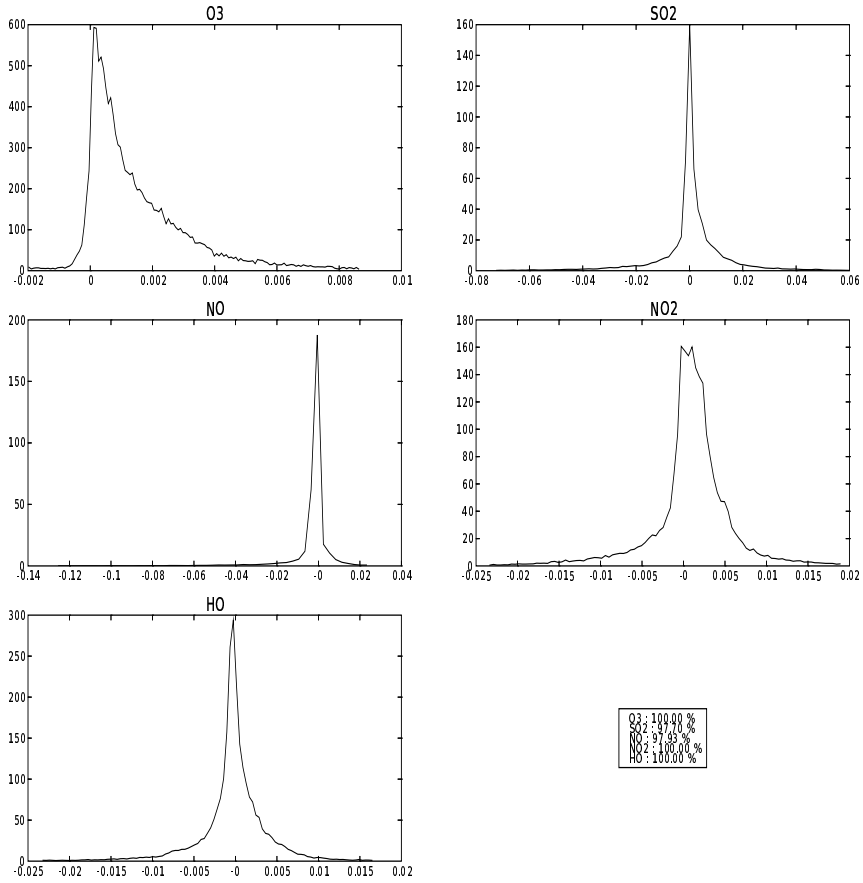

Figure 89: PDF of error between DST3 with flux limiter and upwind for a regional simulation

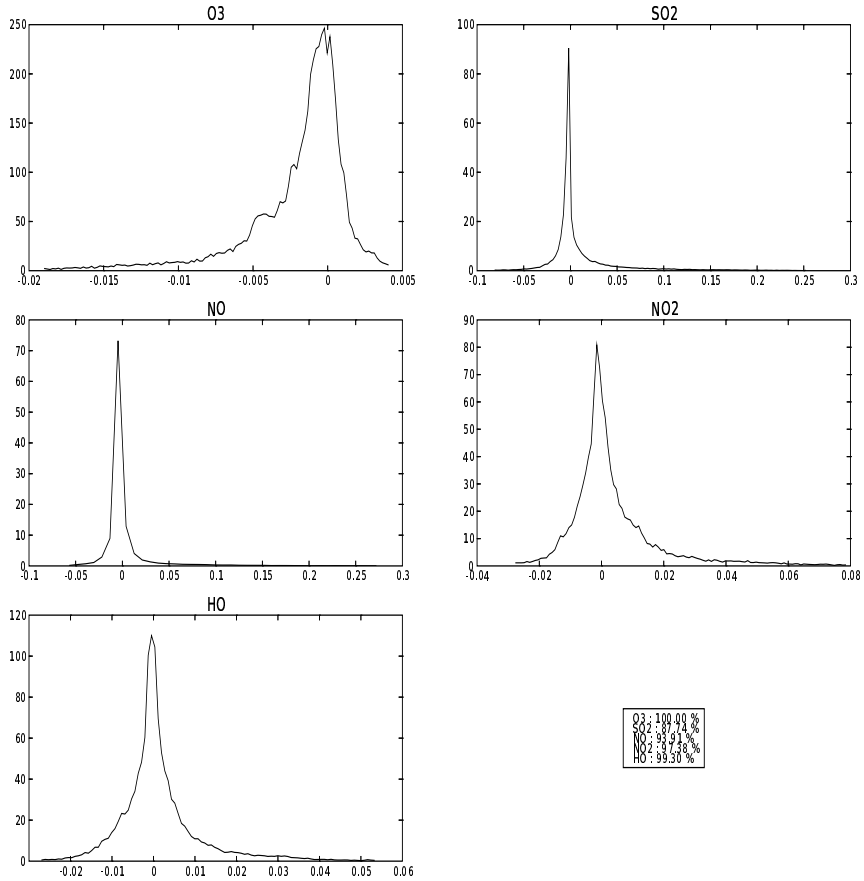

Figure 90: PDF of error between DST3 without flux limiter and upwind for a regional simulation

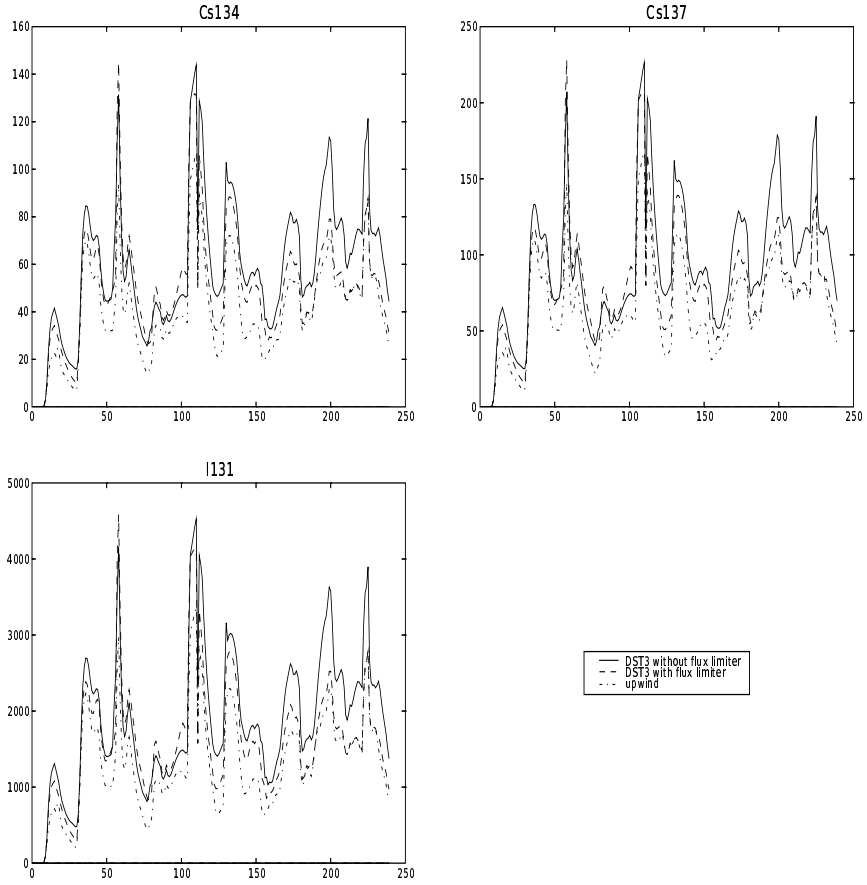

Figure 91: Time evolution of the spatial minimum and maximum ($\mu g \cdot m^{-3}$) for different advection schemes on the Chernobyl accident simulation

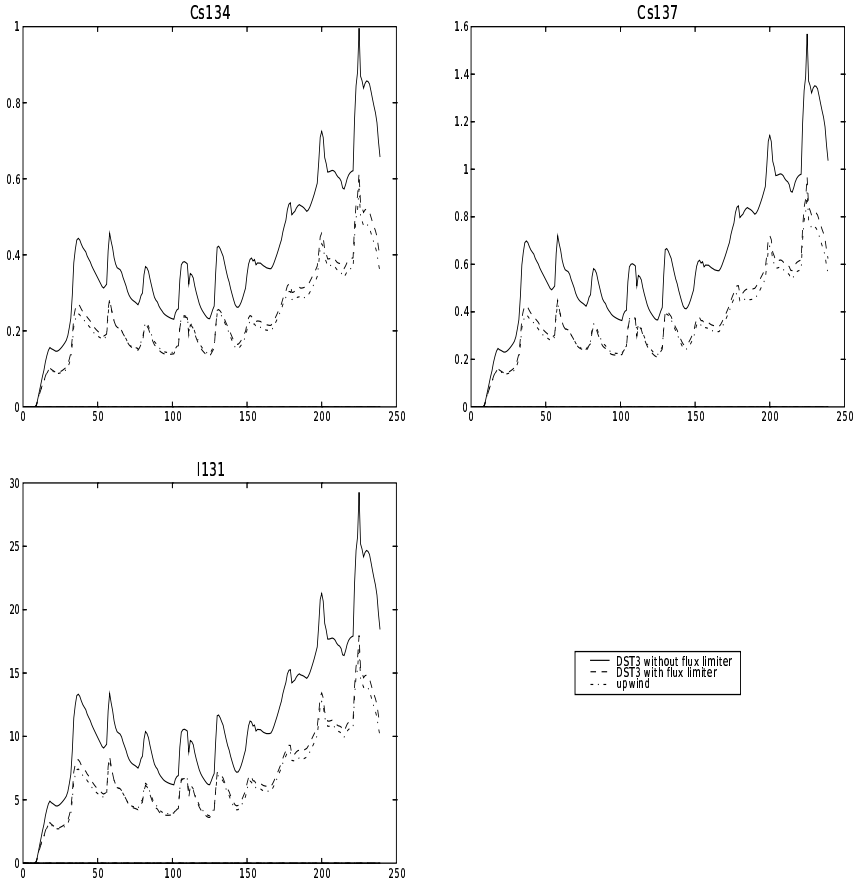

Figure 92: Time evolution of the spatial mean ($\mu g \cdot m^{-3}$) for different advection schemes on the Chernobyl accident simulation

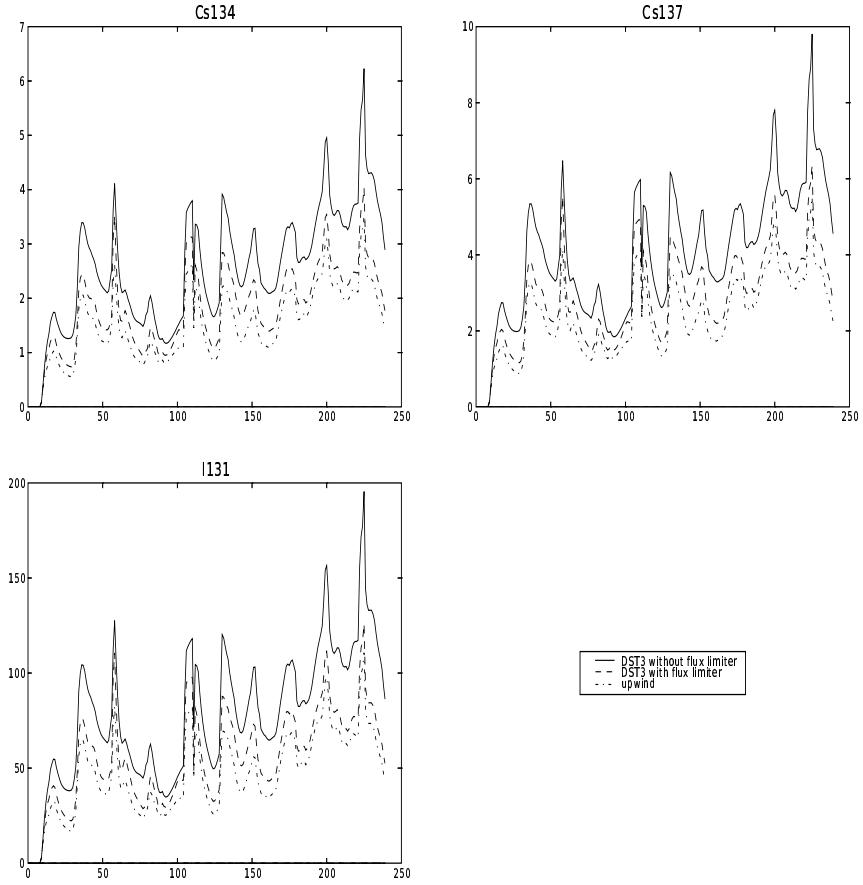

Figure 93: Time evolution of the spatial standard deviation ($\mu g \cdot m^{-3}$) for different advection schemes on the Chernobyl accident simulation

5.2 Positivity

As said in the previous subsection, the Upwind scheme is positive, and mass conservative, whereas third-order schemes introduce oscillations, and thus may lead to negative concentrations. POLAIR3D sets every negative concentration to 0 in order to prevent problems within the chemical process. Therefore, the average concentration is eager to be more important with a scheme that does not guarantee positivity than with a scheme like Upwind. Indeed, the table 4 indicates that the other schemes tend to a higher average concentration (it is not so obvious for HO and O_3, but this can be due to chemistry).

	HO	NO	NO_2	SO_2	O_3
without flux limiter	$3,50.10^{-5}$	0,83	9,14	8,67	89,30
with flux limiter	$3,55.10^{-5}$	0,75	8,53	8,20	88,41
upwind	$3,57.10^{-5}$	0,72	8,49	8,17	89,02

Table 4: Average concentration ($\mu g \cdot m^{-3}$) as a function of advection scheme for a continental simulation

A closer look to positivity with a simulation of the Chernobyl accident will reveal the behaviors of the different schemes.

The Upwind scheme is the reference. For the Chernobyl simulation over 10 days, the average concentrations of the three radioelements Cs_{134},Cs_{137} and I_{131} are shown in table 5.

	Cs_{134}	Cs_{137}	I_{131}
without flux limiter	0,59	0,93	16,40
with flux limiter	0,35	0,55	9,75
upwind	0,33	0,52	9,27

Table 5: Average concentration in Bequerel (Bq) as a function of advection scheme for a Chernobyl simulation

Even though the third-order scheme with flux limiter leads to higher concentrations than the Upwind scheme, the difference is really negligible compared to the third-order scheme without flux limiter (for each species, the difference is about 5%). Therefore, even though the scheme with flux limiter does not guarantee positivity, it seems to be a good compromise.

5.3 Directional splitting

As implemented in POLAIR3D, the advection process is solved without directional splitting. We want to test the sensitivity to directional splitting. Even though we do not know about the inaccuracy that such a splitting brings, directional splitting allows the CFL condition to be less restrictive.

We test POLAIR3D with a DST scheme using directional splitting. After 1008 iterations, we get the results plotted in figures 94–96. The simulation with directional splitting does not change from the one without splitting. Hoxever, on a regional test and on a Chernobyl simulation, differences are much more noticeable, as shown on figures 108–114

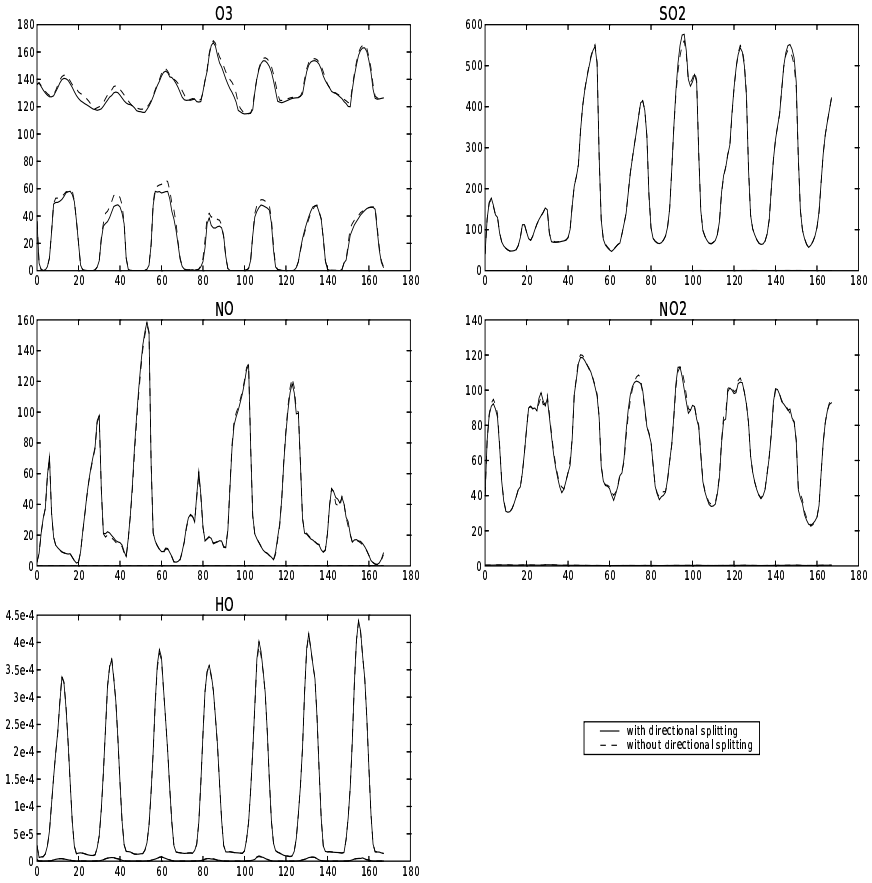

Figure 94: Time evolution of the spatial minimum and maximum ($\mu g \cdot m^{-3}$) with and without directional splitting

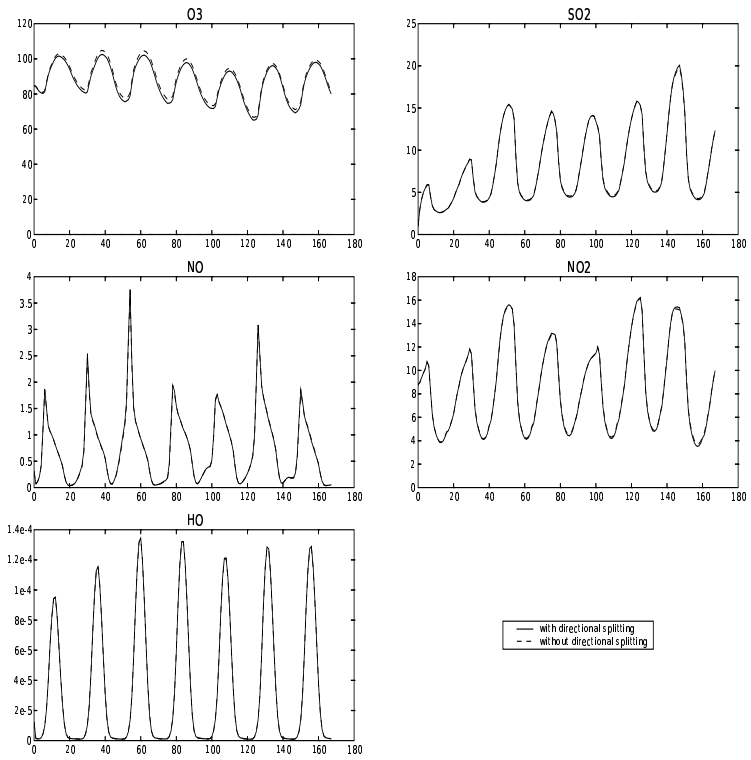

Figure 95: Time evolution of the spatial mean ($\mu g \cdot m^{-3}$) with and without directional splitting

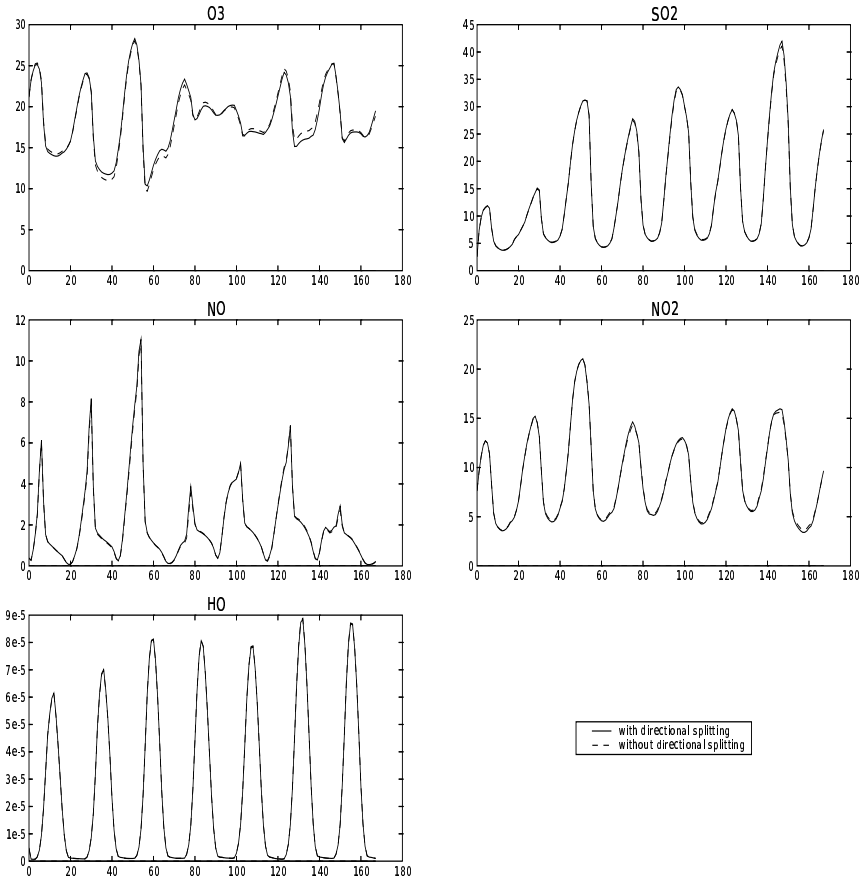

Figure 96: Time evolution of the spatial standard deviation ($\mu g \cdot m^{-3}$) with and without directional splitting

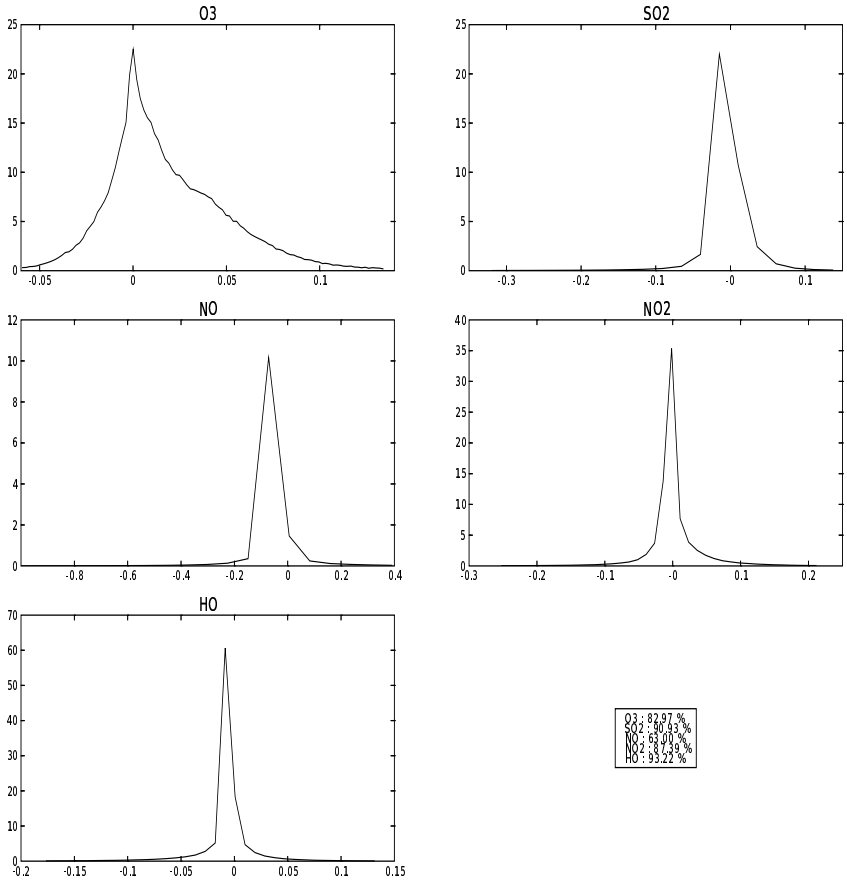

Figure 97: PDF of error between simulations with directional splitting and without directional splitting for a continental simulation

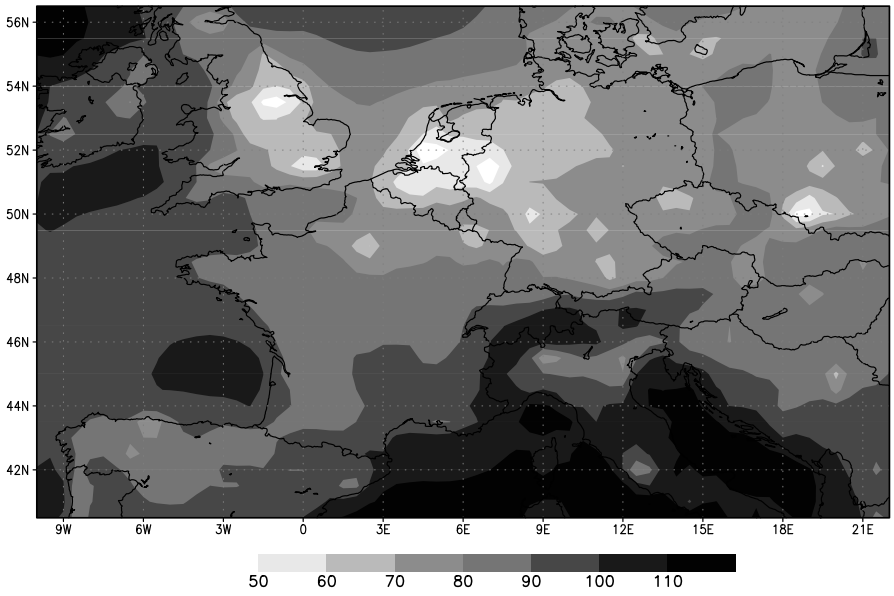

Figure 98: Concentration mean ($\mu g \cdot m^{-3}$) without directional splitting for O_3

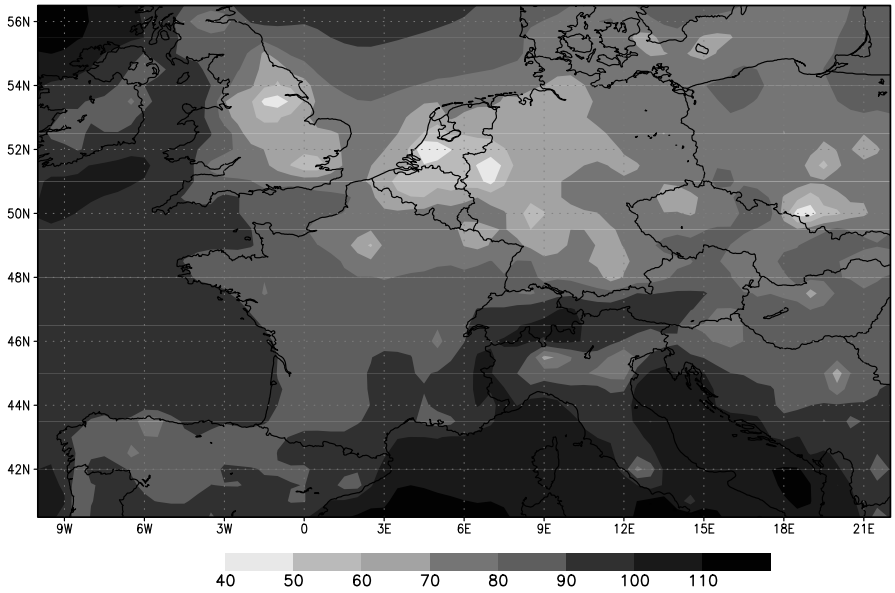

Figure 99: Concentration mean ($\mu g \cdot m^{-3}$) with directional splitting for O_3

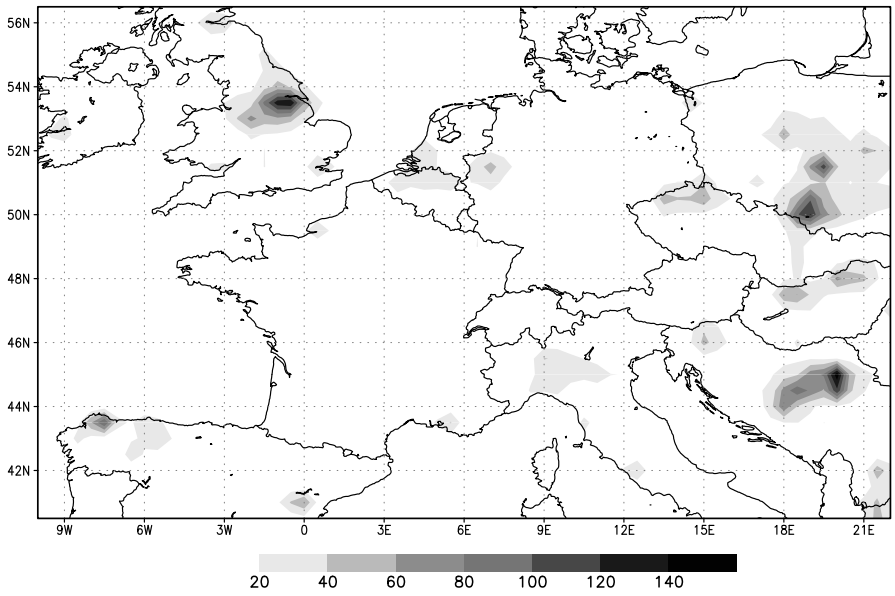

Figure 100: Concentration mean ($\mu g \cdot m^{-3}$) without directional splitting for SO_2

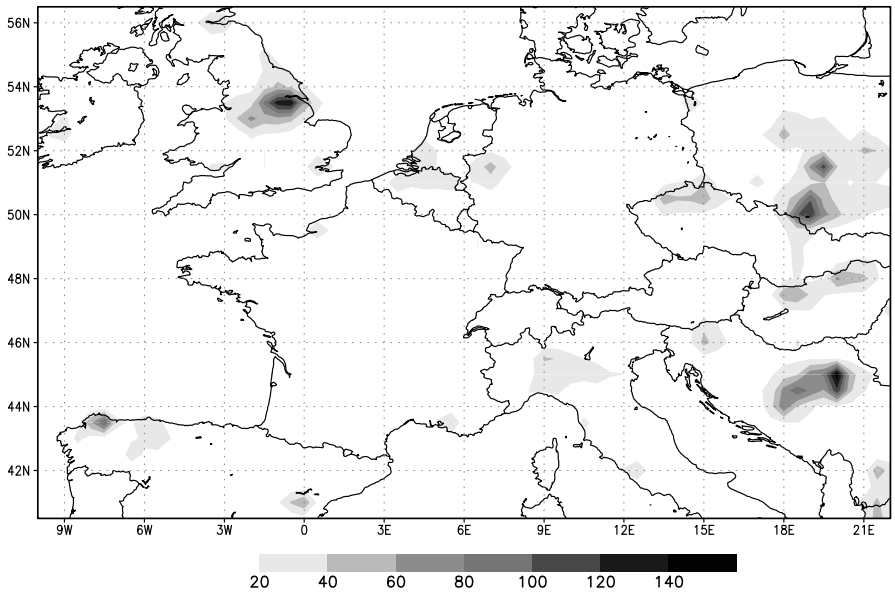

Figure 101: Concentration mean ($\mu g \cdot m^{-3}$) with directional splitting for SO_2

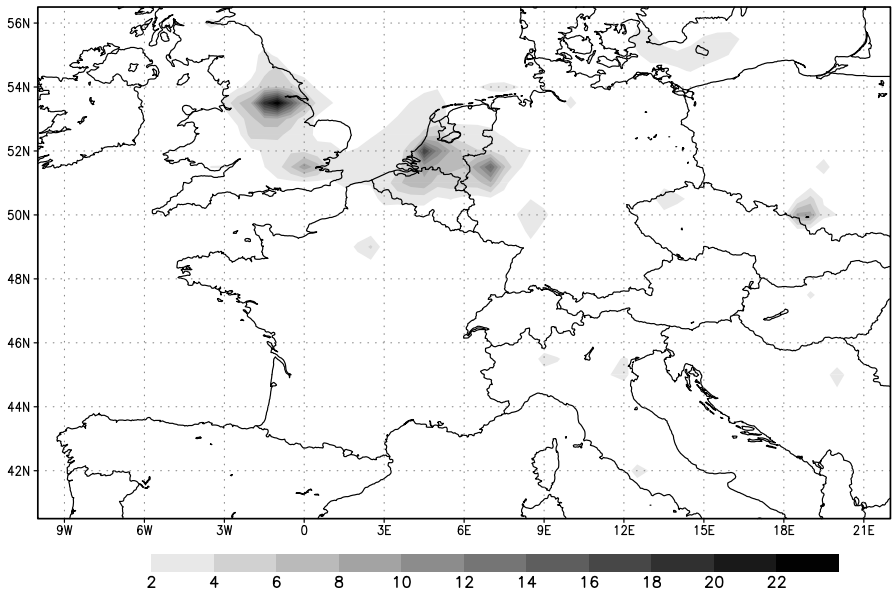

Figure 102: Concentration mean ($\mu g \cdot m^{-3}$) without directional splitting for NO

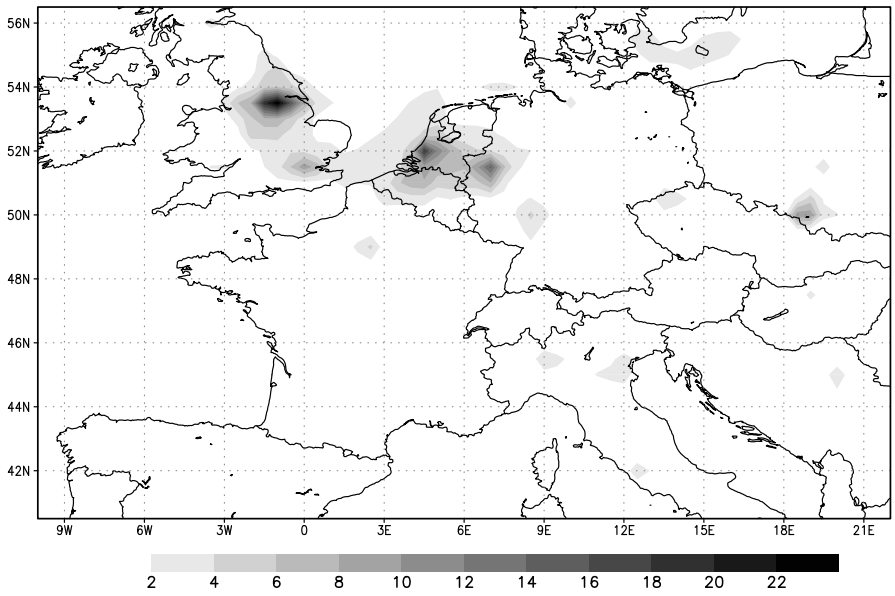

Figure 103: Concentration mean ($\mu g \cdot m^{-3}$) with directional splitting for NO

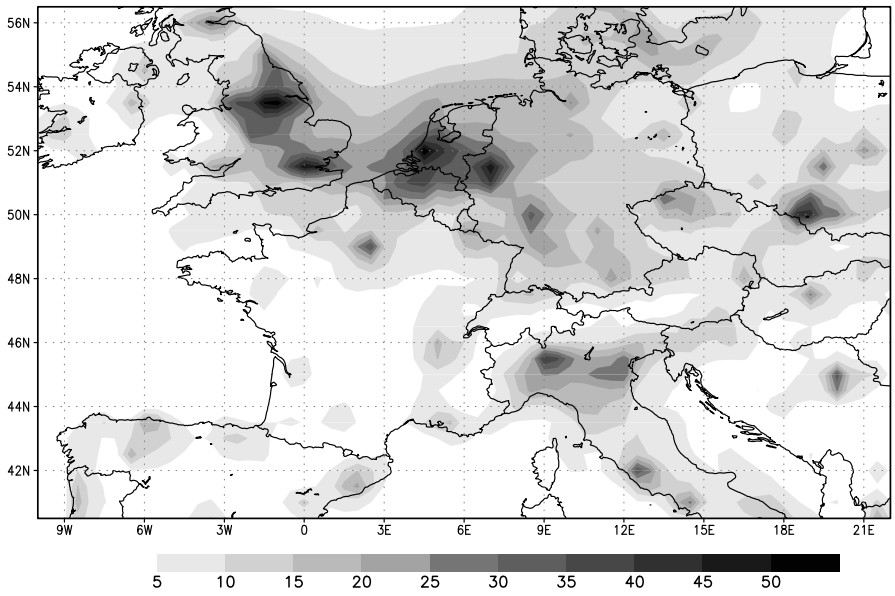

Figure 104: Concentration mean ($\mu g \cdot m^{-3}$) without directional splitting for NO_2

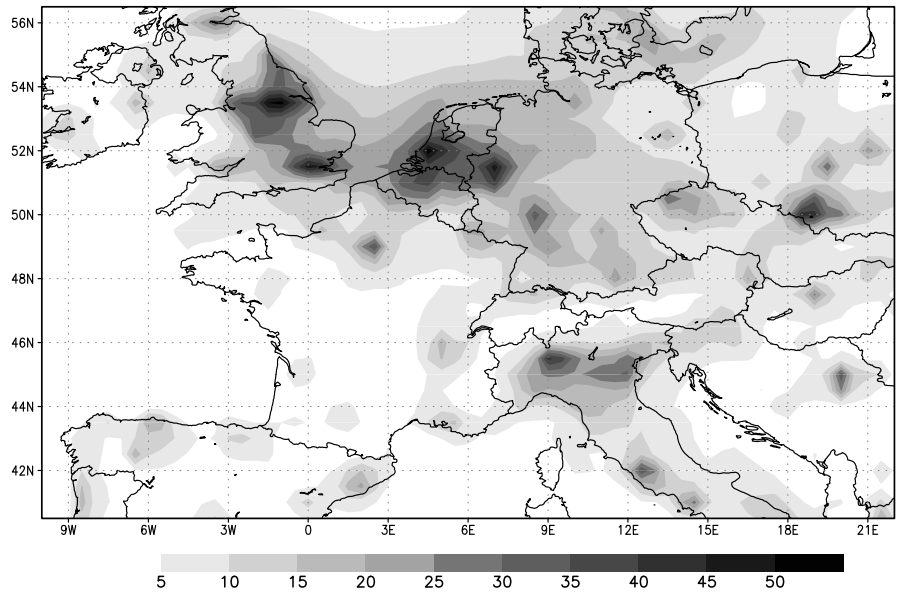

Figure 105: Concentration mean ($\mu g \cdot m^{-3}$) with directional splitting for NO_2

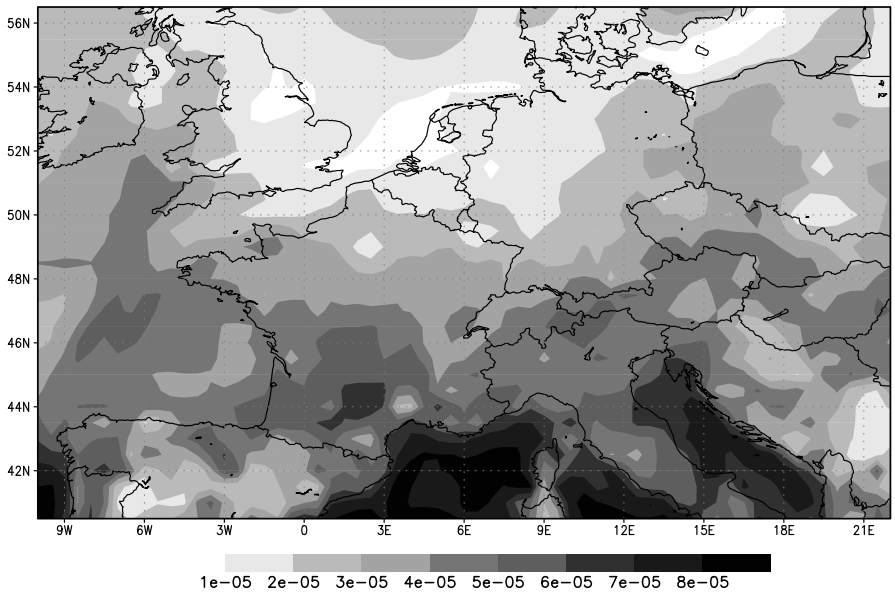

Figure 106: Concentration mean ($\mu g \cdot m^{-3}$) without directional splitting for HO

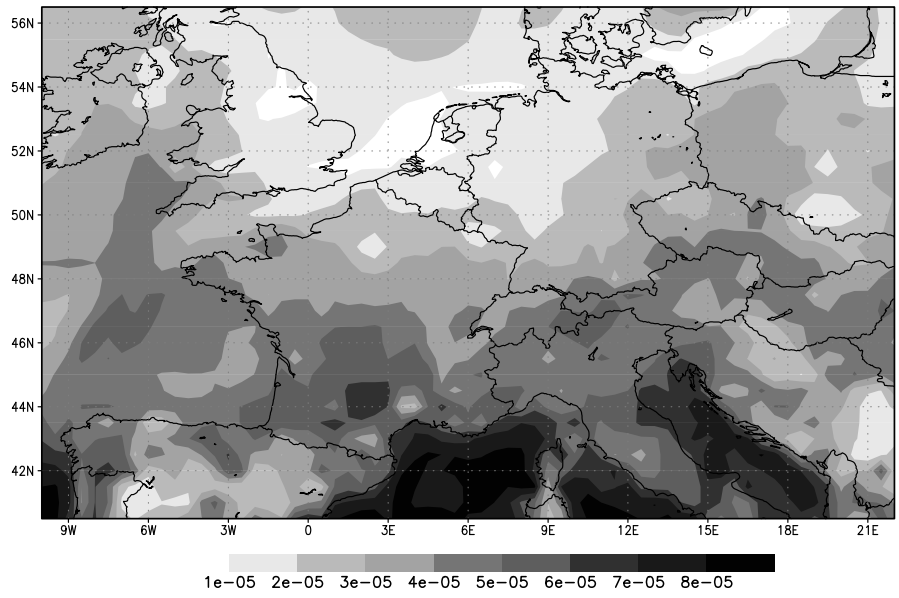

Figure 107: Concentration mean ($\mu g \cdot m^{-3}$) with directional splitting for HO

5.4 Conclusion

Even though an Upwind scheme does lower the peak values, on an average, the advection scheme is not so determining. Besides, the impact of a flux limiter is not very strong on positivity. Therefore, a third-order DST with flux limiter seems to be a good compromise.

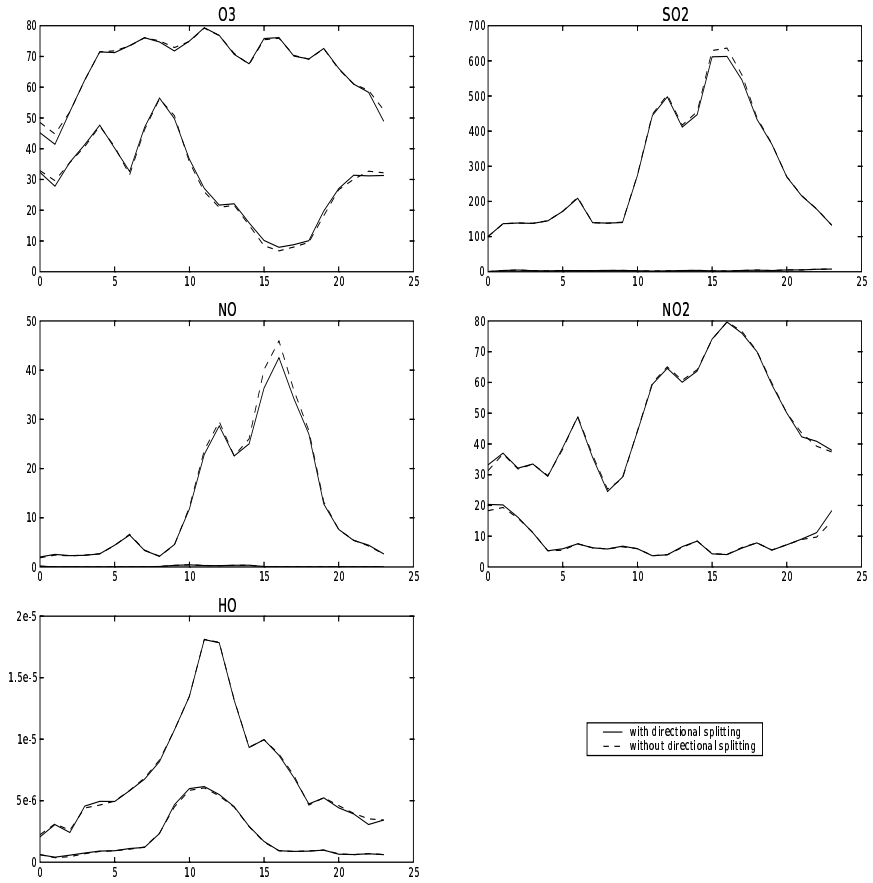

Figure 108: Time evolution of the spatial minimum and maximum ($\mu g \cdot m^{-3}$) over Lille with and without directional splitting

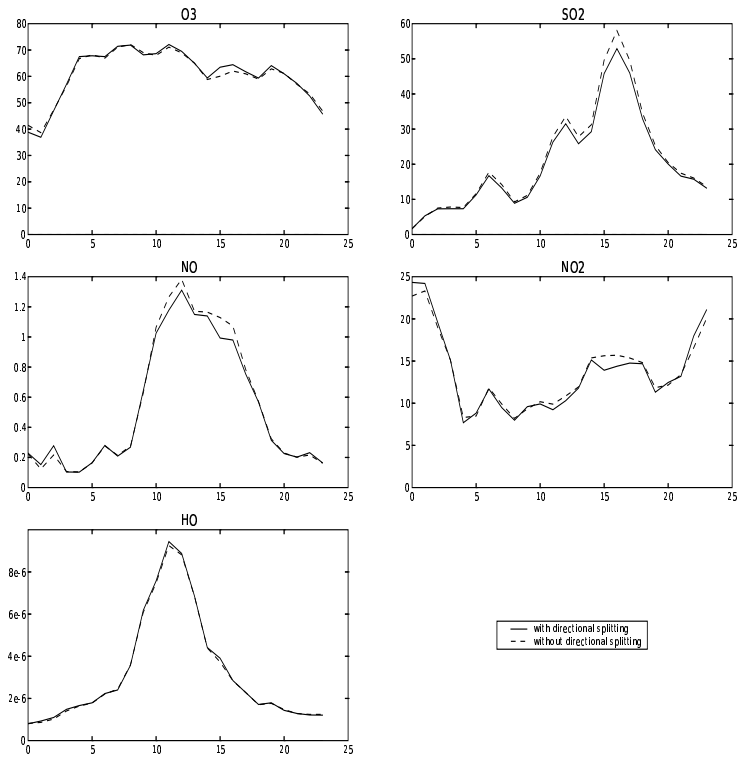

Figure 109: Time evolution of the spatial mean ($\mu g \cdot m^{-3}$) over Lille with and without directional splitting

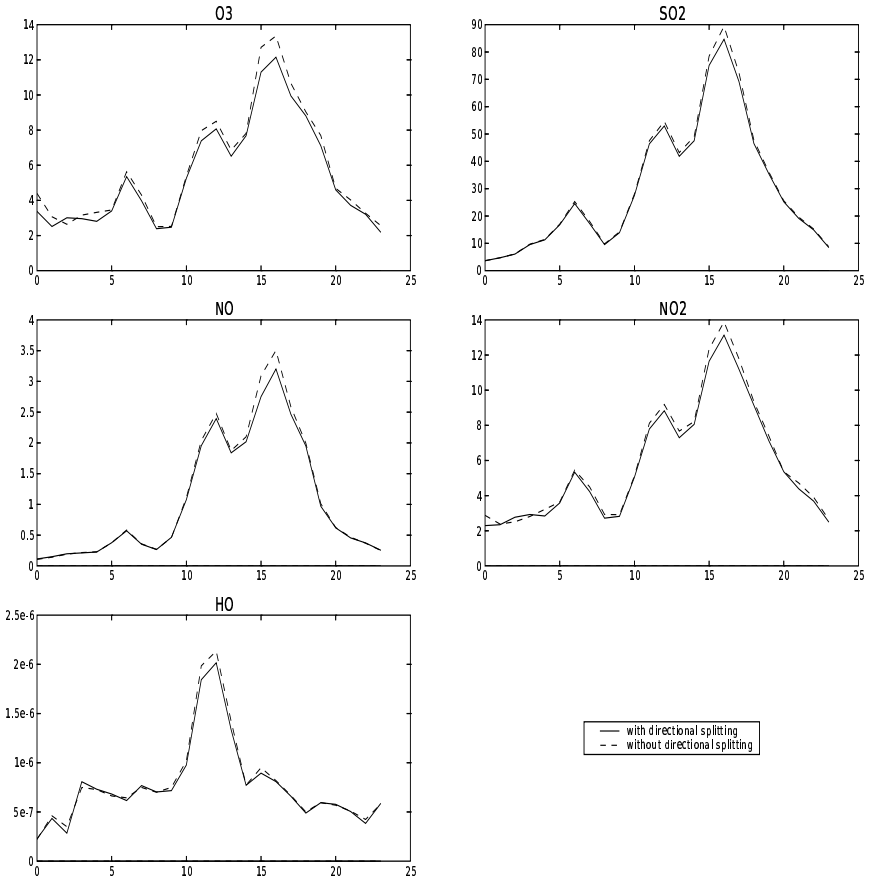

Figure 110: Time evolution of the spatial standard deviation ($\mu g \cdot m^{-3}$) over Lille with and without directional splitting

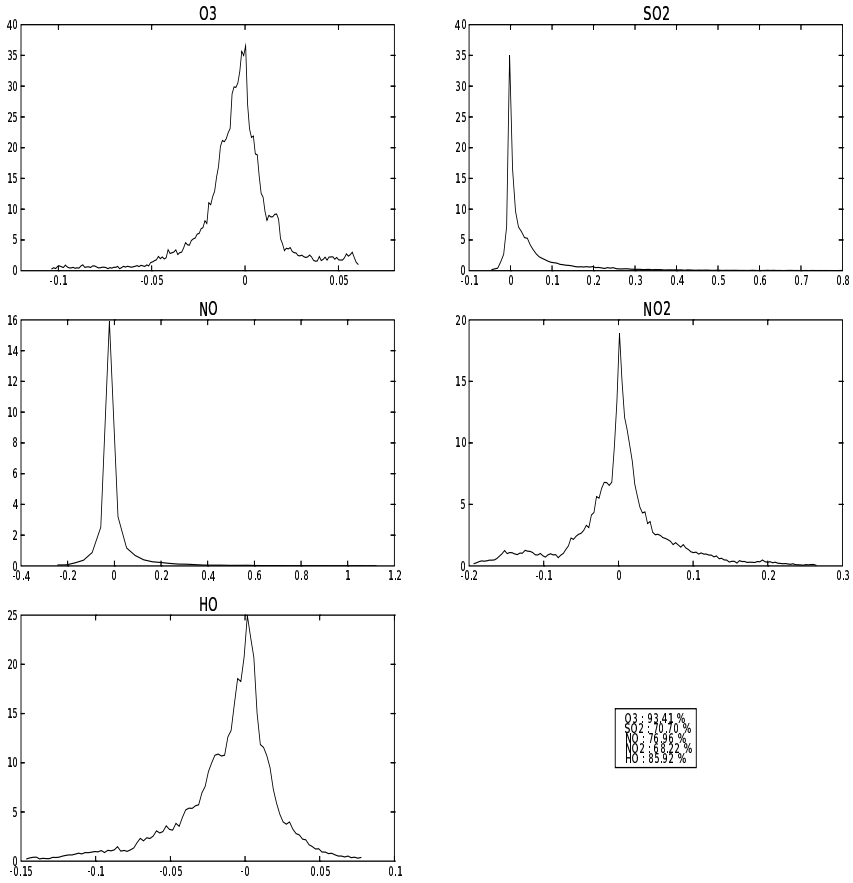

Figure 111: PDF of error between simulations with directional splitting and without directional splitting for a regional simulation

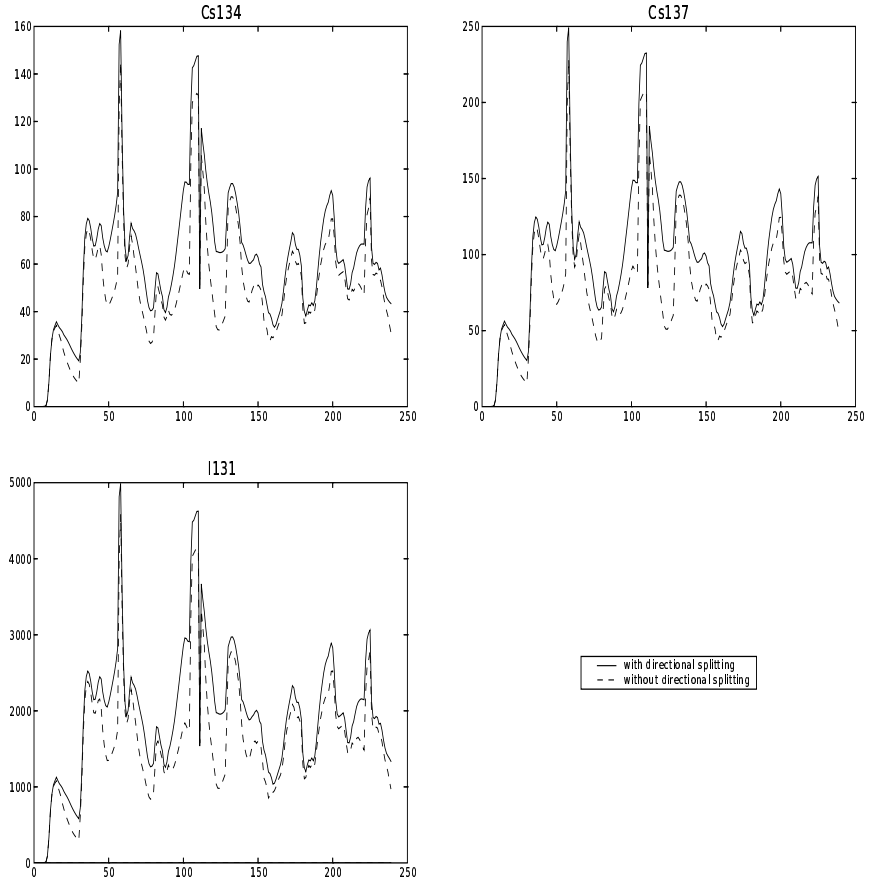

Figure 112: Time evolution of the spatial minimum and maximum ($\mu g \cdot m^{-3}$) with and without directional splitting for a simulation of the Chernobyl accident

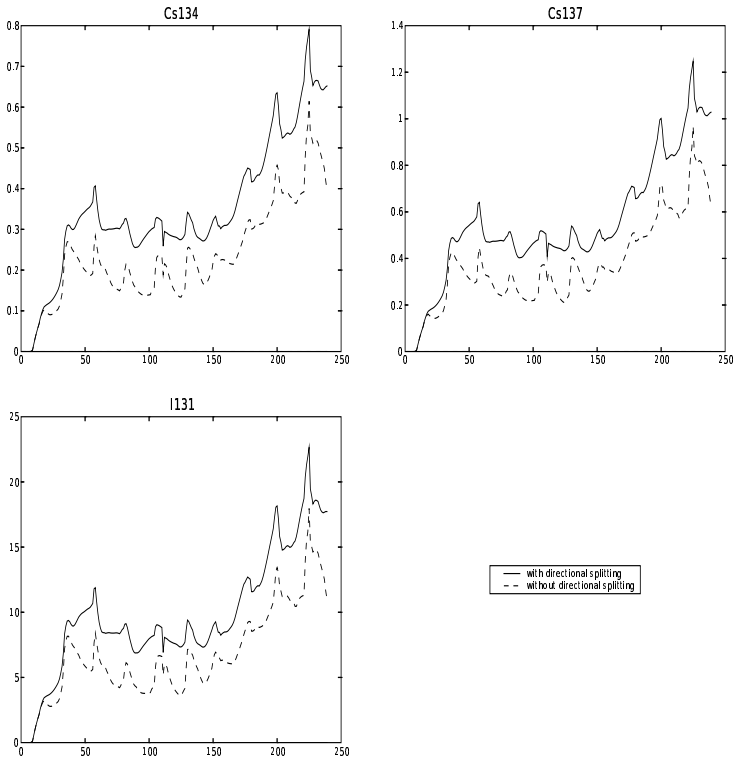

Figure 113: Time evolution of the spatial mean ($\mu g \cdot m^{-3}$) with and without directional splitting for a simulation of the Chernobyl accident

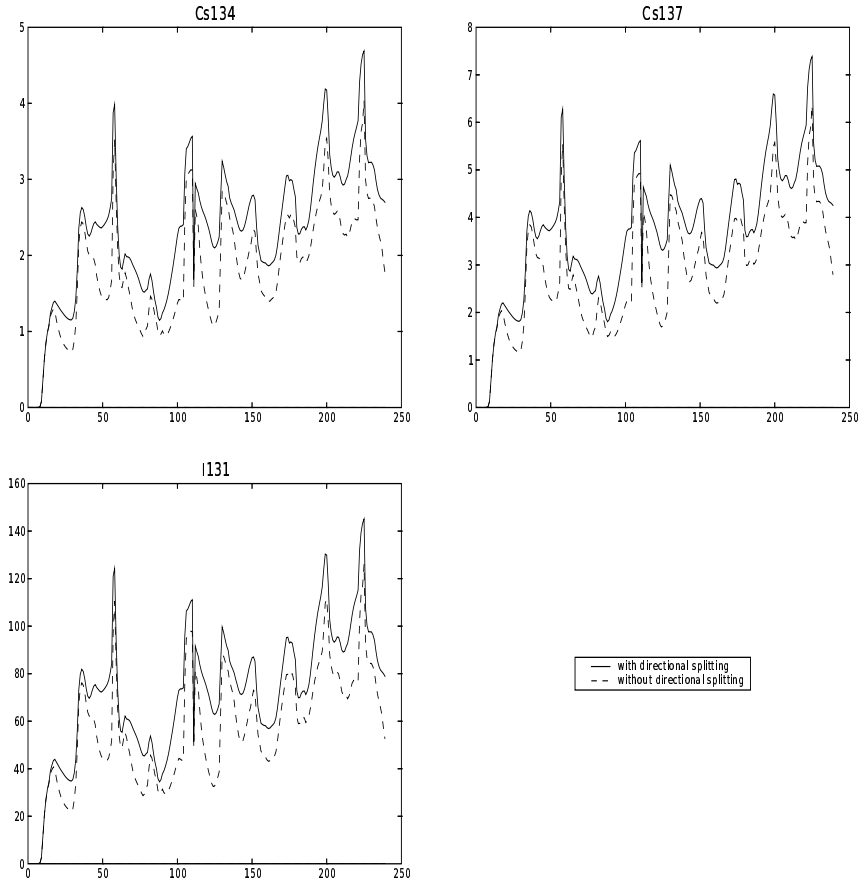

Figure 114: Time evolution of the spatial standard deviation ($\mu g \cdot m^{-3}$) with and without directional splitting for a simulation of the Chernobyl accident

6 Impact of horizontal diffusion

6.1 Diffusion coefficient

The objective of this subsection is to test the sensitivity to the coefficient K_H. Therefore, we run simulations over Europe for a week with 5 different values of K_H: 0, 1 000, 10 000, 50 000 and 100 000 $m^2 \cdot s^{-1}$. Some of these values (0 and 100 000 $m^2.s^{-1}$) are clearly unrealistic, but they are tested for the sake of completeness.

We can see in figure 116 that the value of K_H has a small influence on the spatial average value of concentrations. Indeed, no species seems to be affected by the value of K_H. On the other hand, as shown on figure 115, K_H has an influence on the maximum of concentrations. We see clearly that the peaks of concentration are very affected according to the value of K_H (for SO_2, NO or NO_2, the value of the peaks for $K_H = 50\ 000\ m^2 \cdot s^{-1}$ is 25 to 50 % less significant than the value for $K_H = 0\ m^2 \cdot s^{-1}$.) This was foreseeable, as diffusion " flattens " the maxima.

In the same way, the spatial standard deviation is slightly affected by the value of K_H. This number is representative of the variability of the concentrations on the field, this is why the value of K_H more strongly affects the heterogeneous species, such as NO, NO_2 and SO_2, which are more localized.

Only HO does not seem to be subject to the influence of K_H.

Figures 115–117 thus seem to indicate that the physical diffusion is not negligible compared to the numerical diffusion.

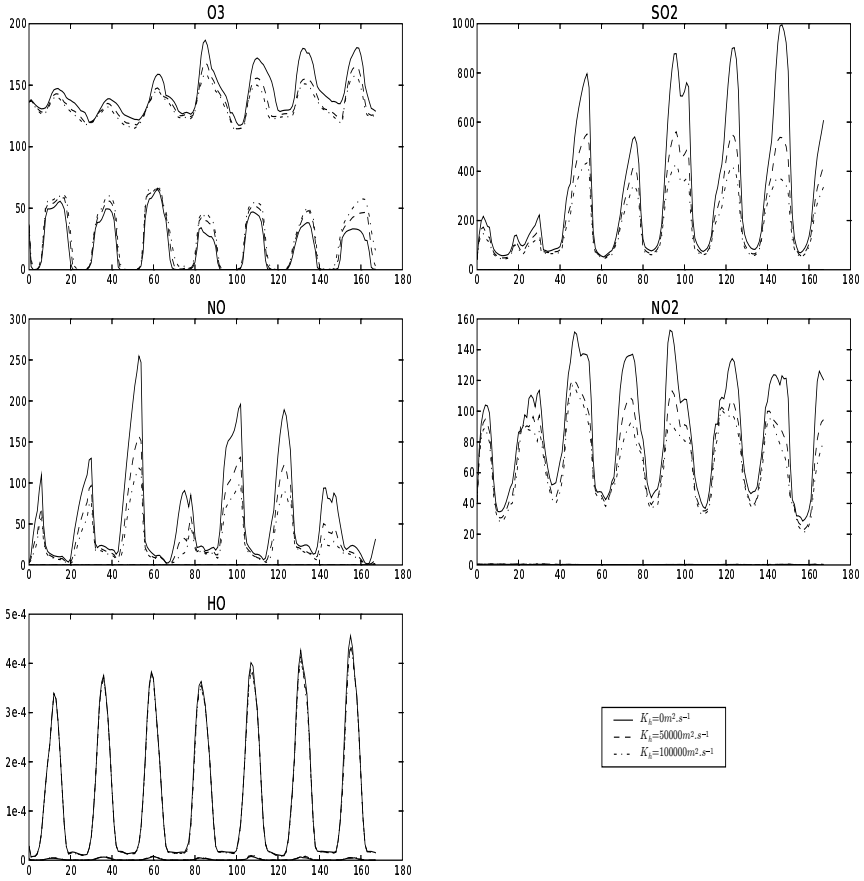

Figure 115: Time evolution of the spatial minimum and maximum ($\mu g \cdot m^{-3}$) for different values of K_H

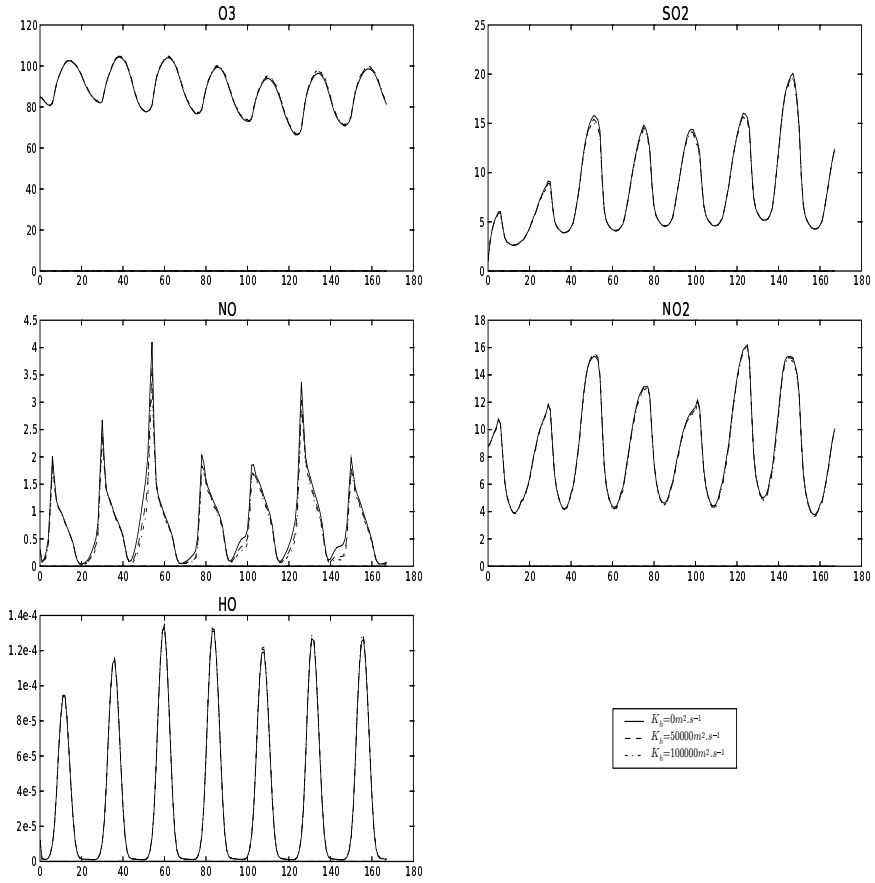

Figure 116: Time evolution of the spatial mean ($\mu g \cdot m^{-3}$) for different values of K_H

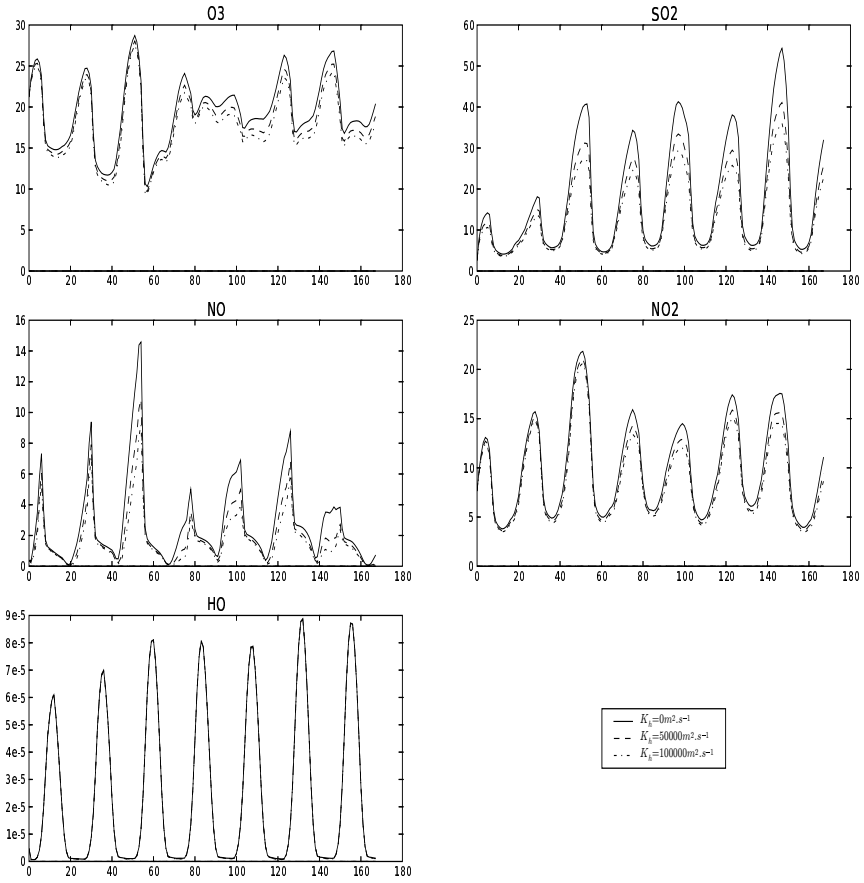

Figure 117: Time evolution of the spatial standard deviation ($\mu g \cdot m^{-3}$) for different values of K_H

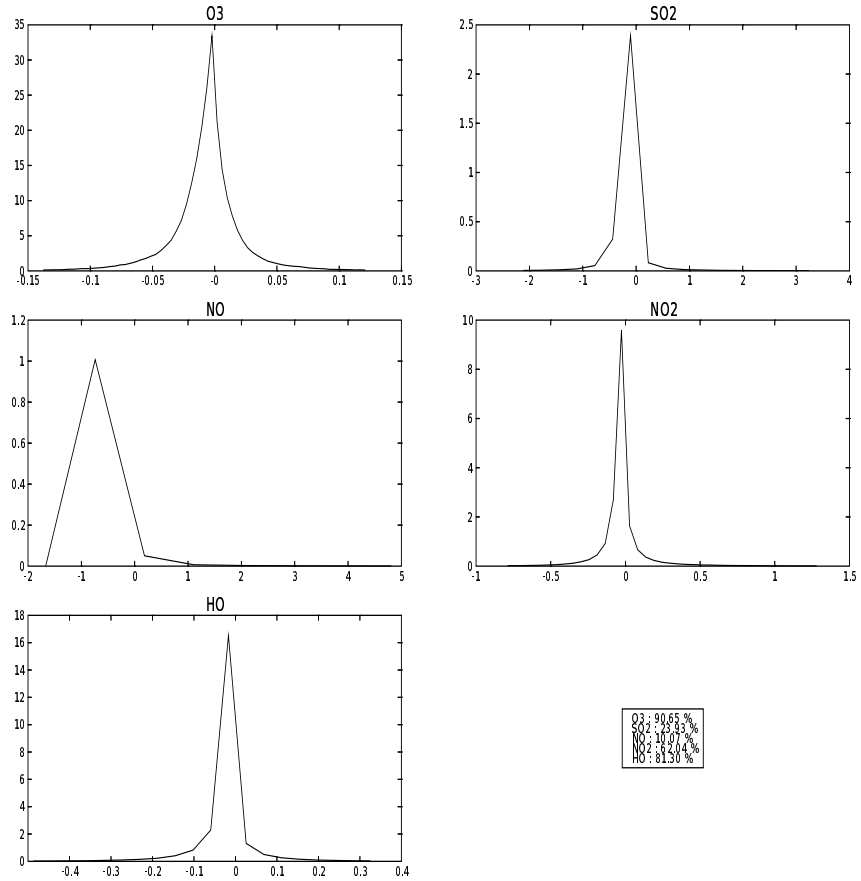

Figure 118: PDF of error between $K_H = 0$ and $K_H = 50000$

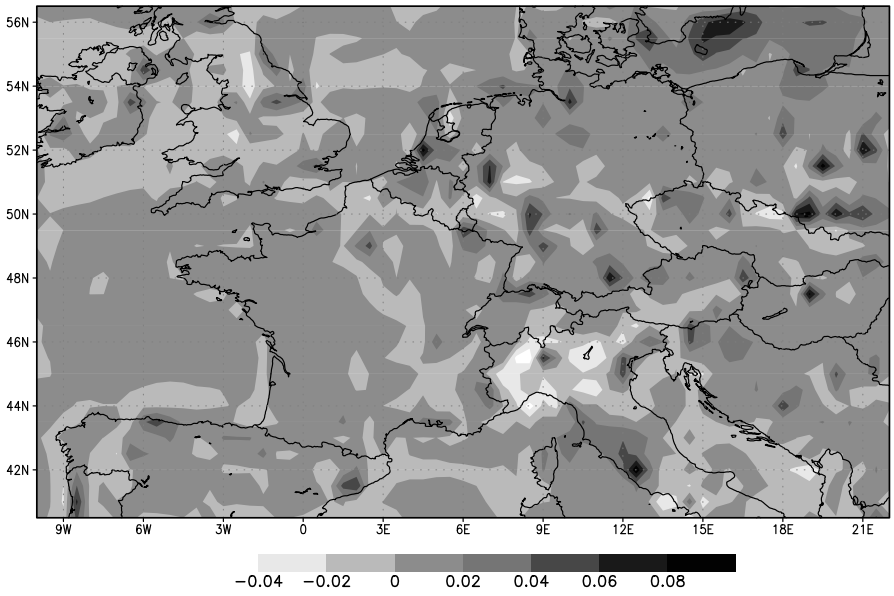

Figure 119: $\frac{mean(K_H{=}50000) - mean(K_H{=}0)}{mean(K_H{=}0)}$ *for* O_3

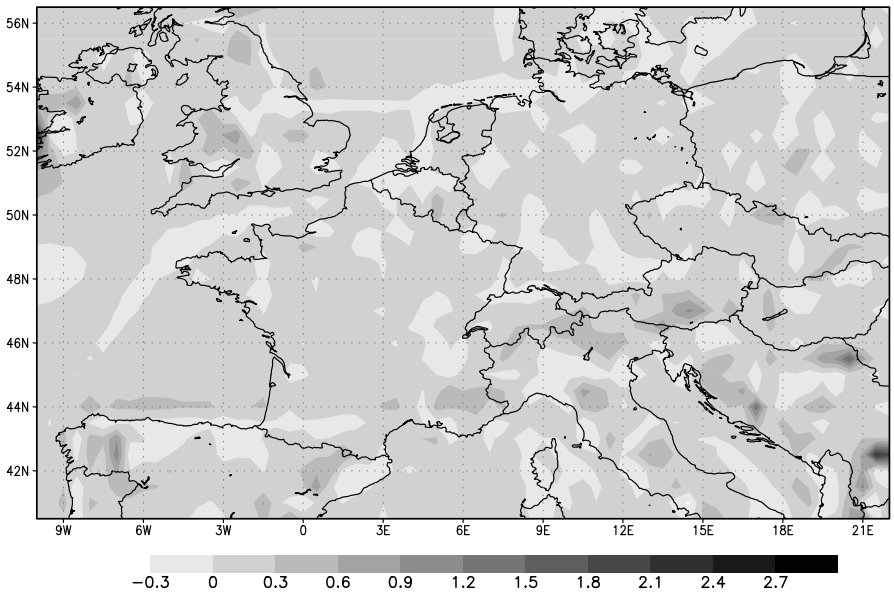

Figure 120: $\frac{mean(K_H{=}50000)-mean(K_H{=}0)}{mean(K_H{=}0)}$ *for* SO_2

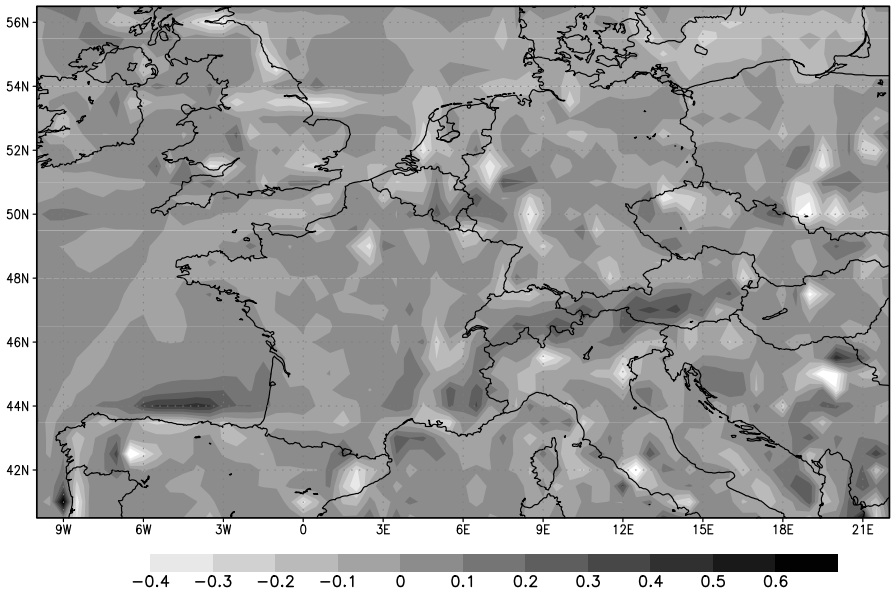

Figure 121: $\frac{mean(K_H{=}50000)-mean(K_H{=}0)}{mean(K_H{=}0)}$ *for* NO

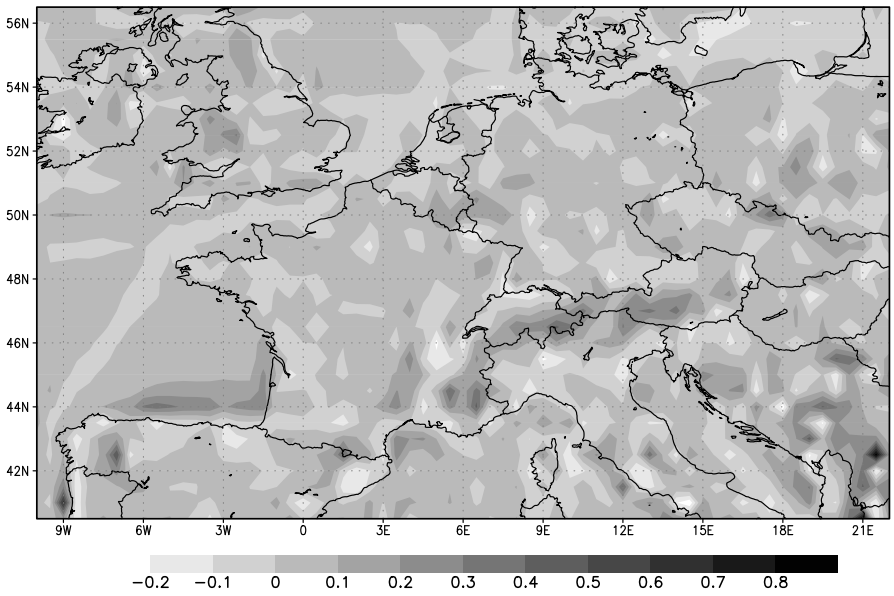

Figure 122: $\frac{mean(K_H{=}50000)-mean(K_H{=}0)}{mean(K_H{=}0)}$ *for* NO_2

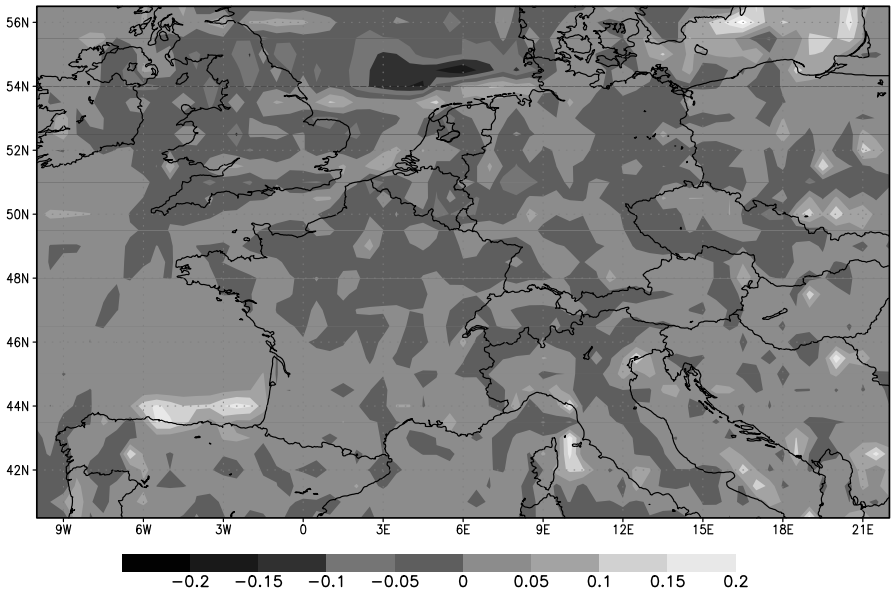

Figure 123: $\frac{mean(K_H{=}50000)-mean(K_H{=}0)}{mean(K_H{=}0)}$ *for* HO

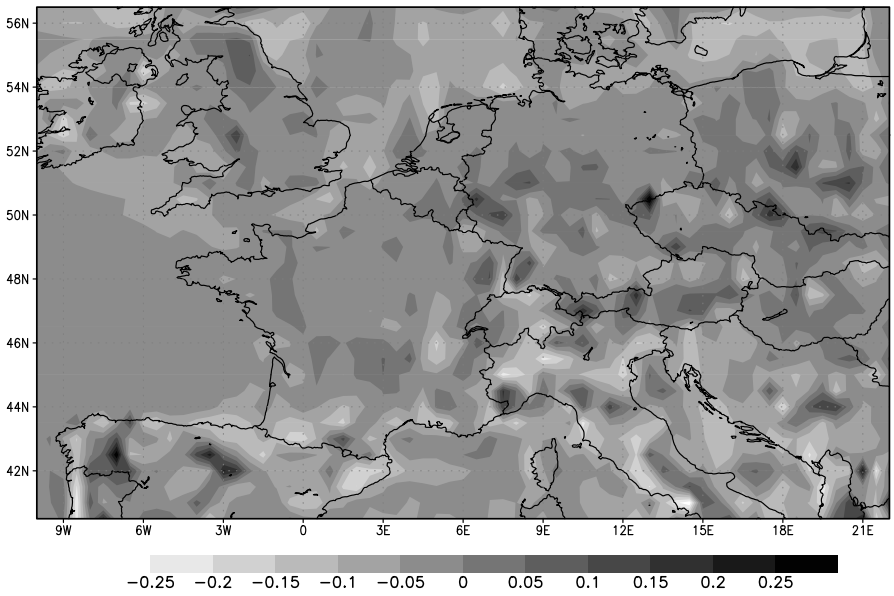

Figure 124: $\frac{\sigma(K_H{=}50000)-\sigma(K_H{=}0)}{\sigma(K_H{=}0)}$ *for* O_3

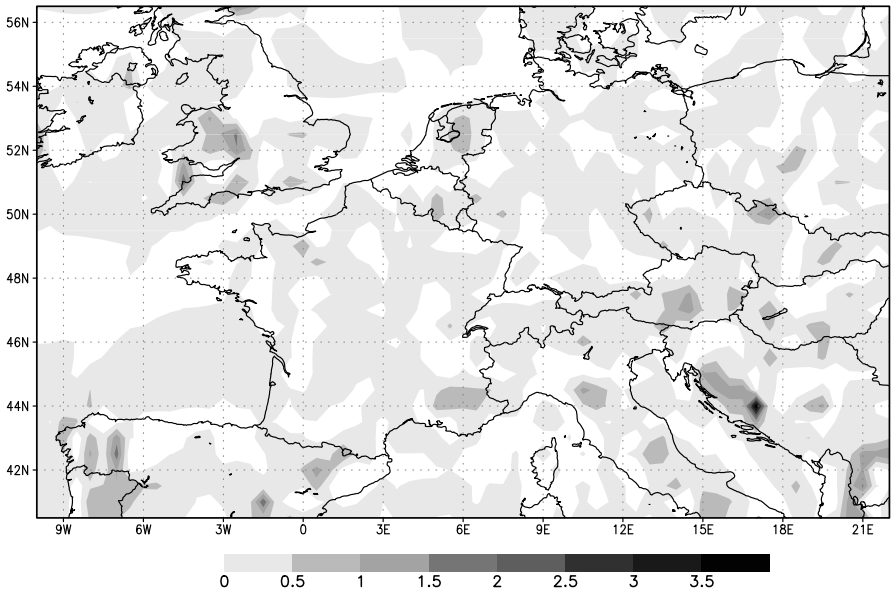

Figure 125: $\frac{\sigma(K_H{=}50000)-\sigma(K_H{=}0)}{\sigma(K_H{=}0)}$ *for* SO_2

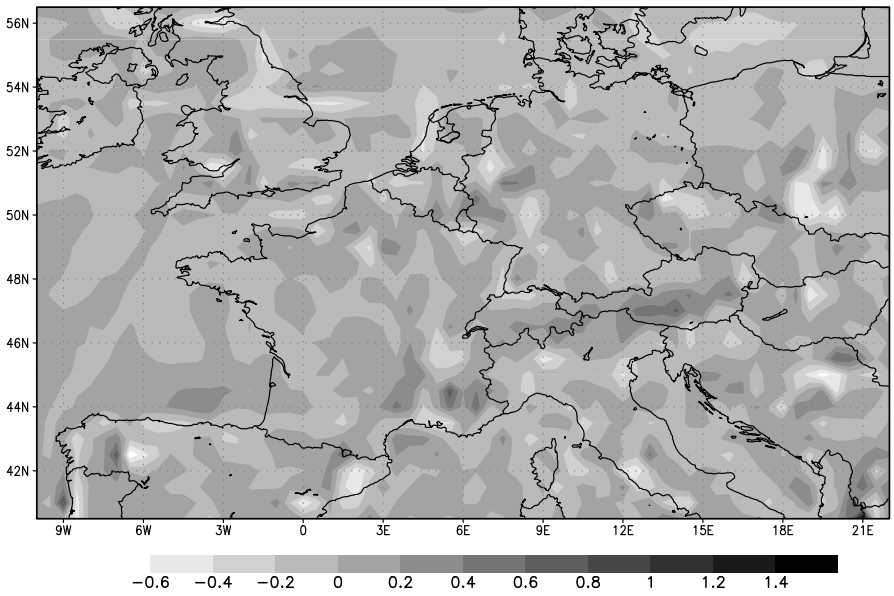

Figure 126: $\frac{\sigma(K_H{=}50000)-\sigma(K_H{=}0)}{\sigma(K_H{=}0)}$ *for* NO

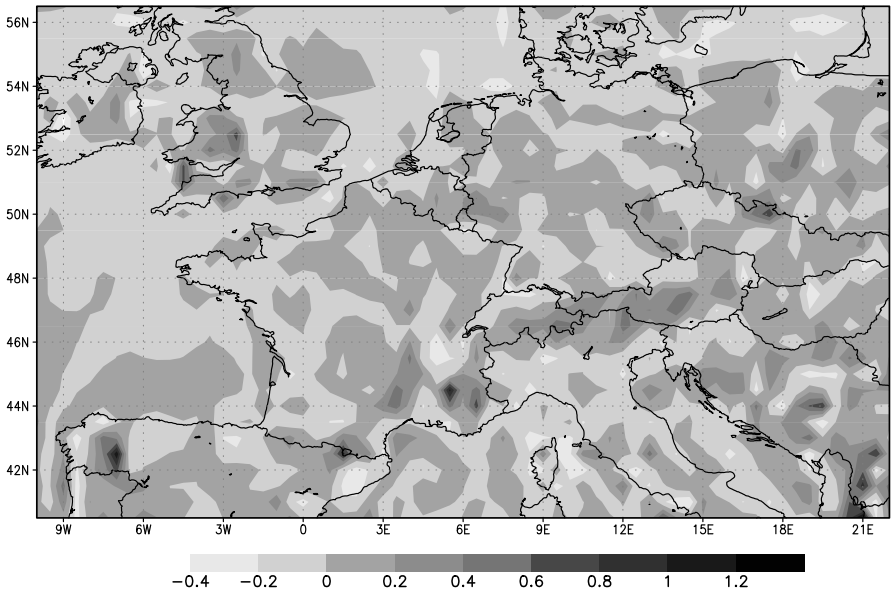

Figure 127: $\frac{\sigma(K_H{=}50000)-\sigma(K_H{=}0)}{\sigma(K_H{=}0)}$ *for* NO_2

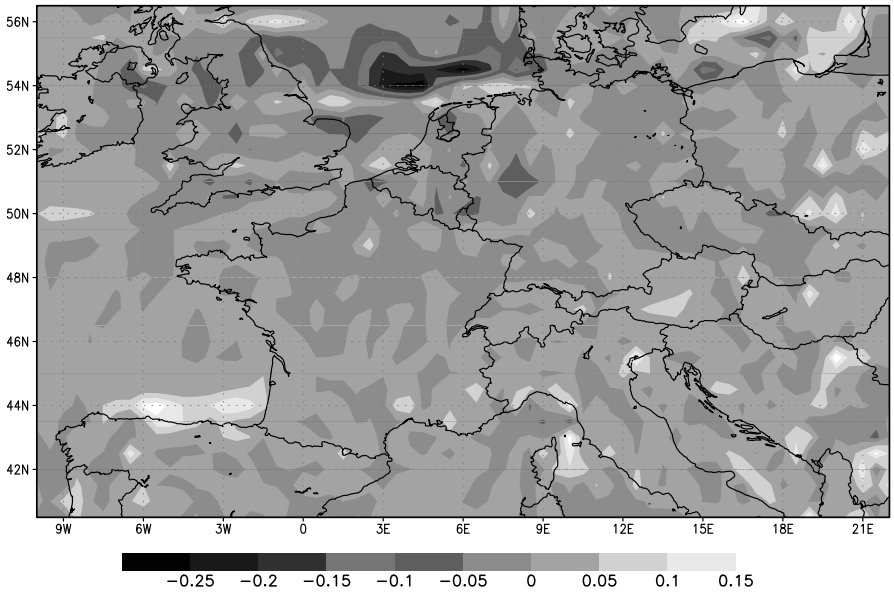

Figure 128: $\frac{\sigma(K_H{=}50000)-\sigma(K_H{=}0)}{\sigma(K_H{=}0)}$ *for* HO

The figures 119–128 indicate that the value of K_H may have a real influence, mainly around large cities, which are the major points of emissions of the species NO and SO_2.

Indeed, the cities correspond to polluted areas where the spatial heterogeneity of the emissions is strong. It is thus logical that the impact of the horizontal diffusion is significant in these places.

The cities also correspond to the most inhabited places in which the thresholds of pollution can be reached, and thus become alarming for the populations.

On the other hand, we see in the figures 124 and 119 that O_3, which is a rather homogeneous species, does not feel very strongly the impact of K_H. (However we see differences on the level in large cities because ozone is affected by the emissions of NO_x.)

Figures 129–130 plot the time evolution of the concentrations over Paris and over Pontarlier.

K_H is important for the forecast in agglomerations (since we are interested in the peaks of pollution) but not very significant for certain impact studies (where we are more interested in the average).

Figures 131–133 allow us to compare numerical diffusion and physical diffusion. It seems indeed that there is not a very important difference between using an Upwind scheme (which brings high numerical diffusion) without physical diffusion and using a DST with strong physical diffusion.

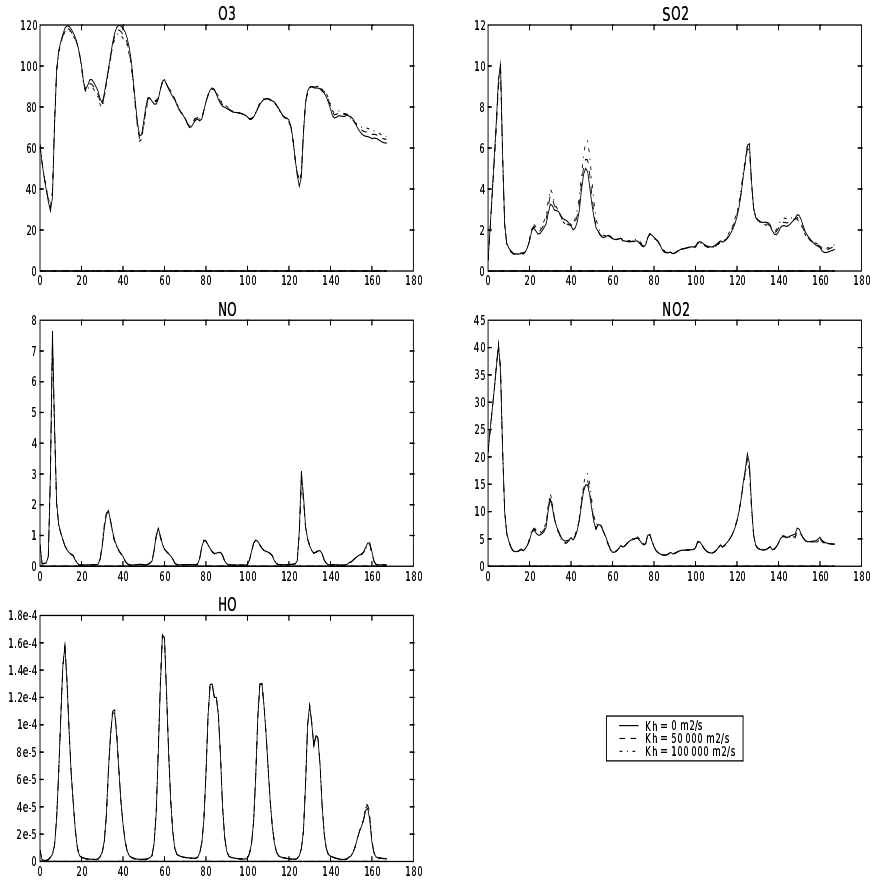

Figure 129: Time evolution of the concentrations ($\mu g \cdot m^{-3}$) over Paris for different values of K_H

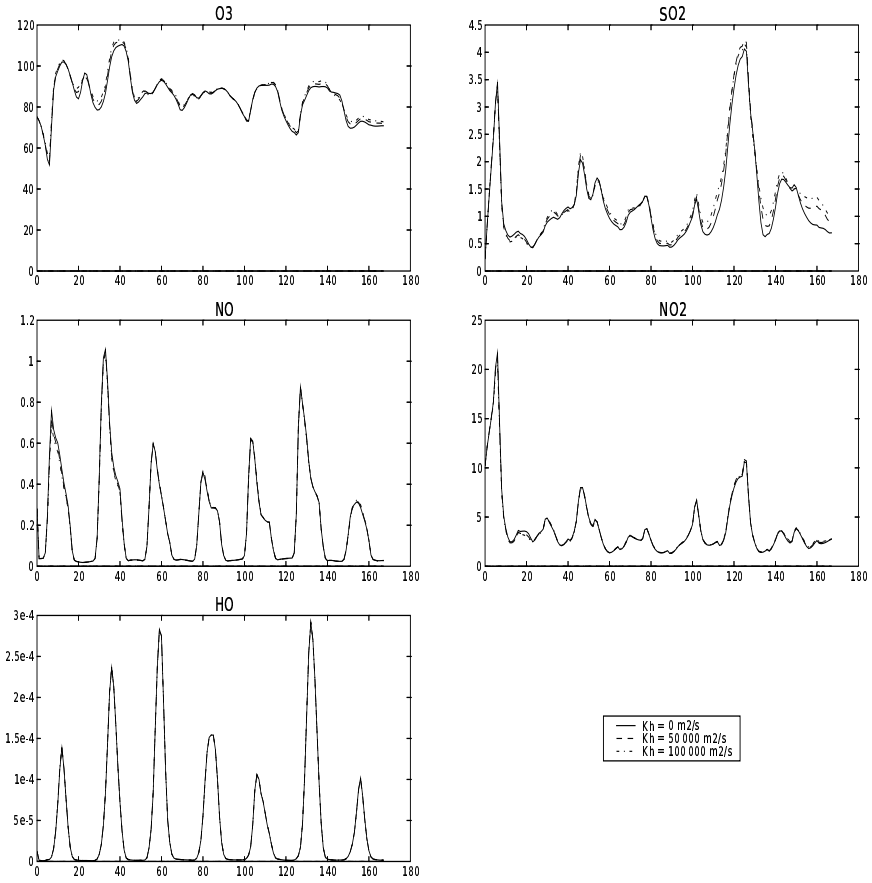

Figure 130: Time evolution of the concentrations ($\mu g \cdot m^{-3}$) over Pontarlier for different values of K_H

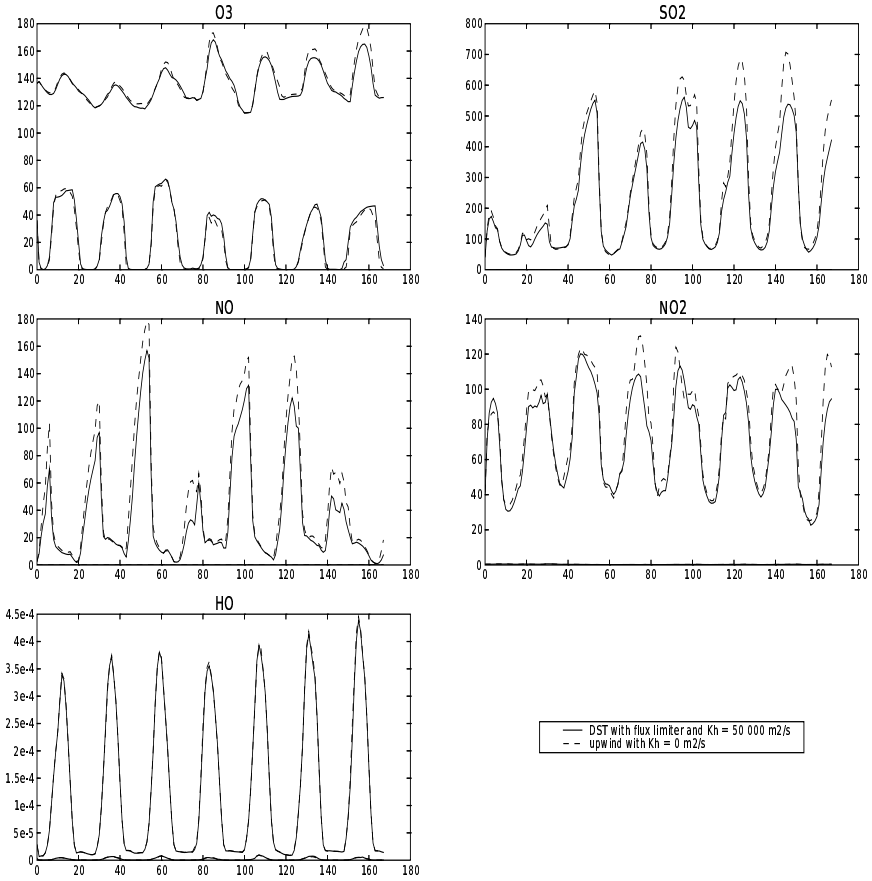

Figure 131: Time evolution of the spatial minimum and maximum ($\mu g \cdot m^{-3}$) with different advection schemes and diffusion coefficients

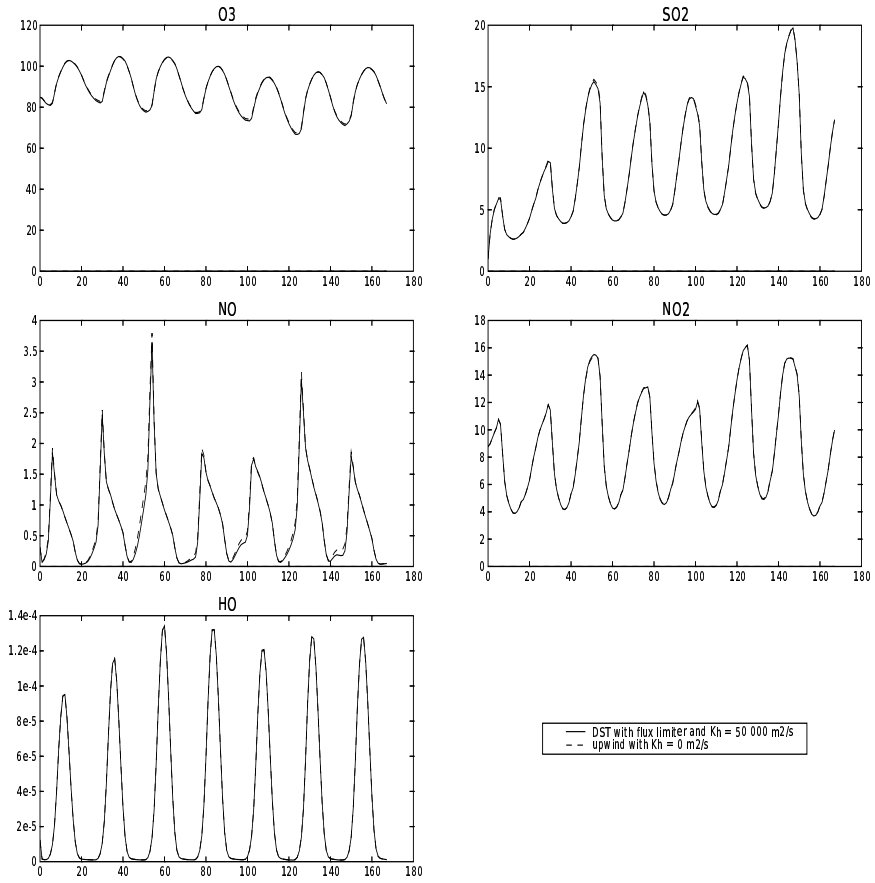

Figure 132: Time evolution of the spatial mean ($\mu g \cdot m^{-3}$) with different advection schemes and diffusion coefficients

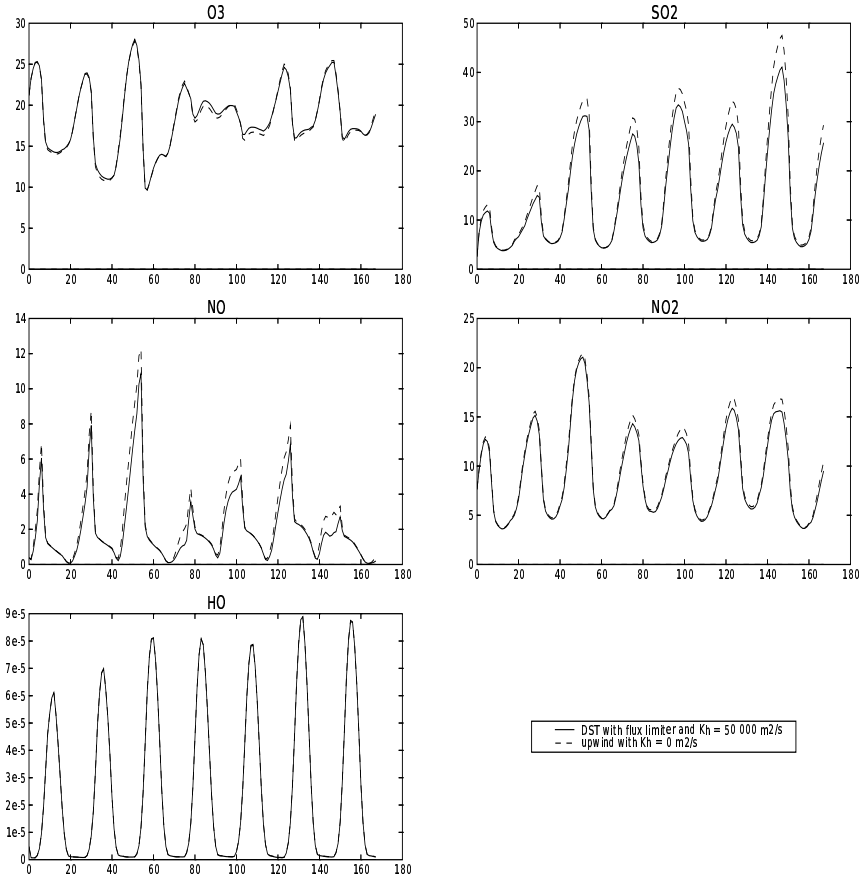

Figure 133: Time evolution of the spatial standard deviation ($\mu g \cdot m^{-3}$) with different advection schemes and diffusion coefficients

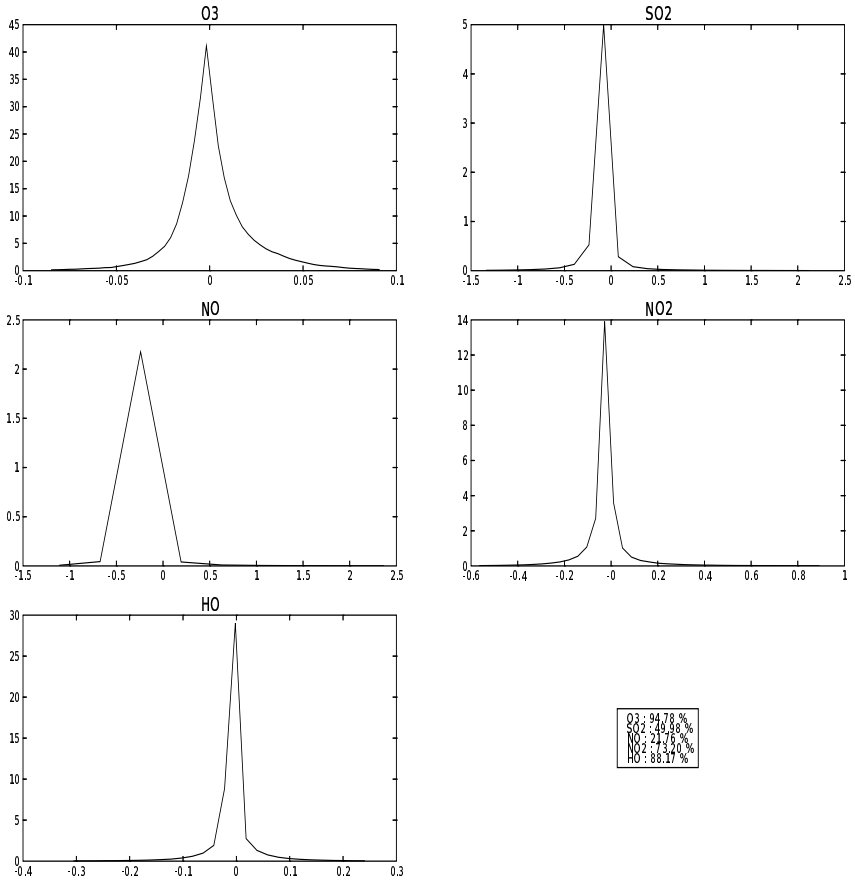

Figure 134: PDF of error between simulations with DST3 with flux limiter & Kh=50000 vs upwind & Kh=0

6.2 Density formulation

We now want to look at the influence of the parameterization choice. By choosing the concentration parameterization, the approximation is made:

$$\nabla\left(\frac{c_i}{\rho}\right) \simeq \frac{\nabla c_i}{\rho} \tag{48}$$

Therefore, we should mainly see differences between the concentration parameterization and the mass fraction parameterization in places where ρ is quite variable. Figure 135 indicates how ρ is distributed over the domain:

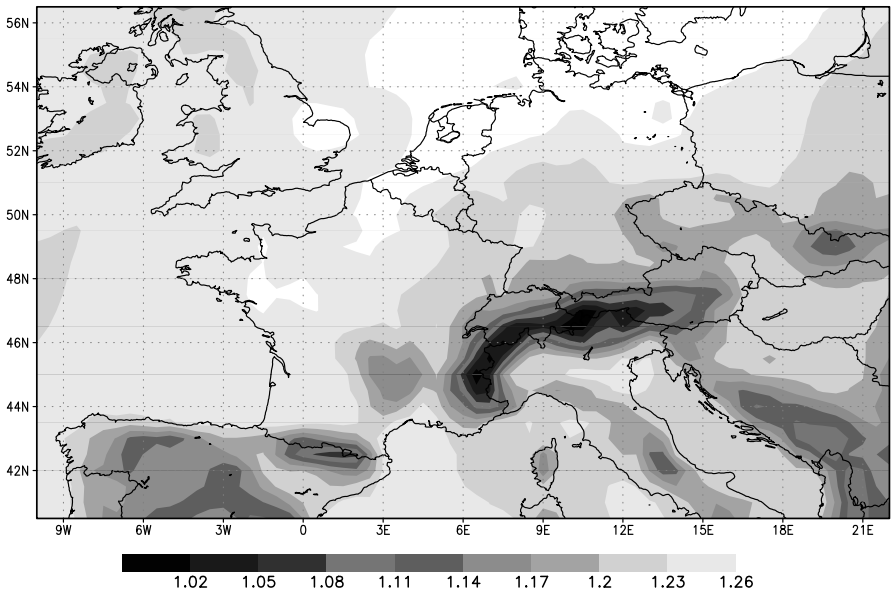

Figure 135: ρ over Europe

In figures 136–138, it seems that the species which is mostly influenced by the parameterization is O_3. Indeed, figure 140 indicates how ρ evolves with z. We can see that ρ is stronger at ground, therefore, the diffusion will be stronger at ground when air density is taken into account compared to the simulation where air density is not taken into account. As far as O_3 is concerned, the diffusion tends to transport it towards ground. Therefore, when air density is taken into account, this phenomenon is amplified. That is why O_3 is more important at ground when air density is taken into account.

Figures 141–145 seem to indicate that the parameterization choice does not have a great influence on the results, since the impact is not

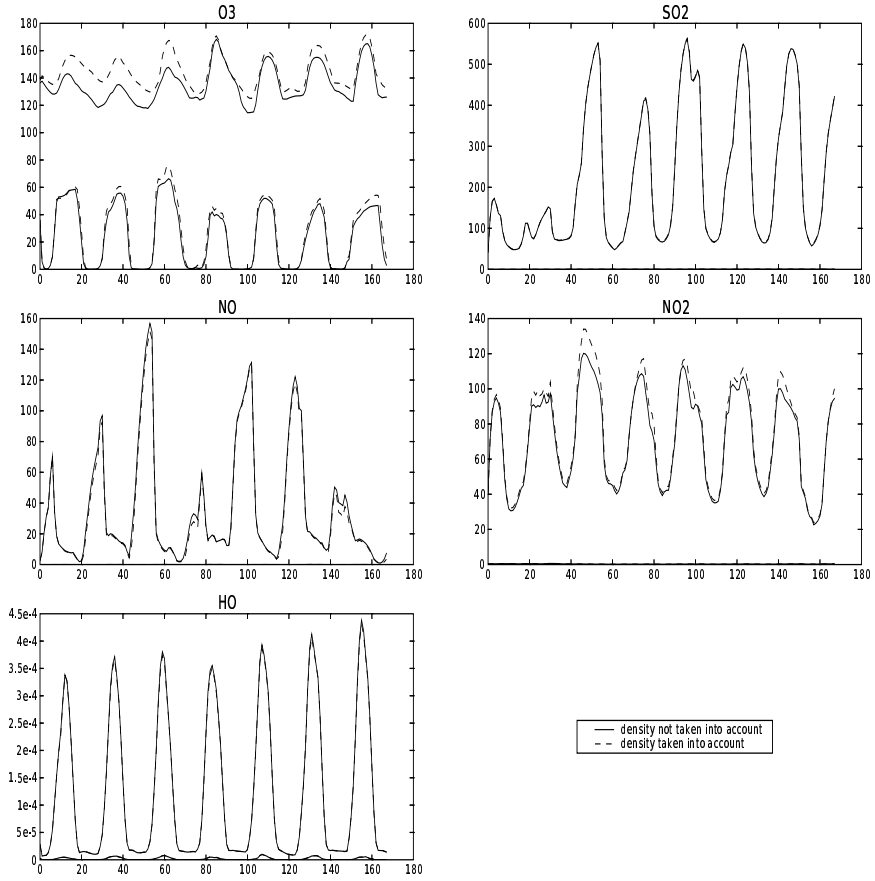

Figure 136: Time evolution of the spatial minimum and maximum ($\mu g \cdot m^{-3}$) on the ground when air density is taken into account or not taken into account

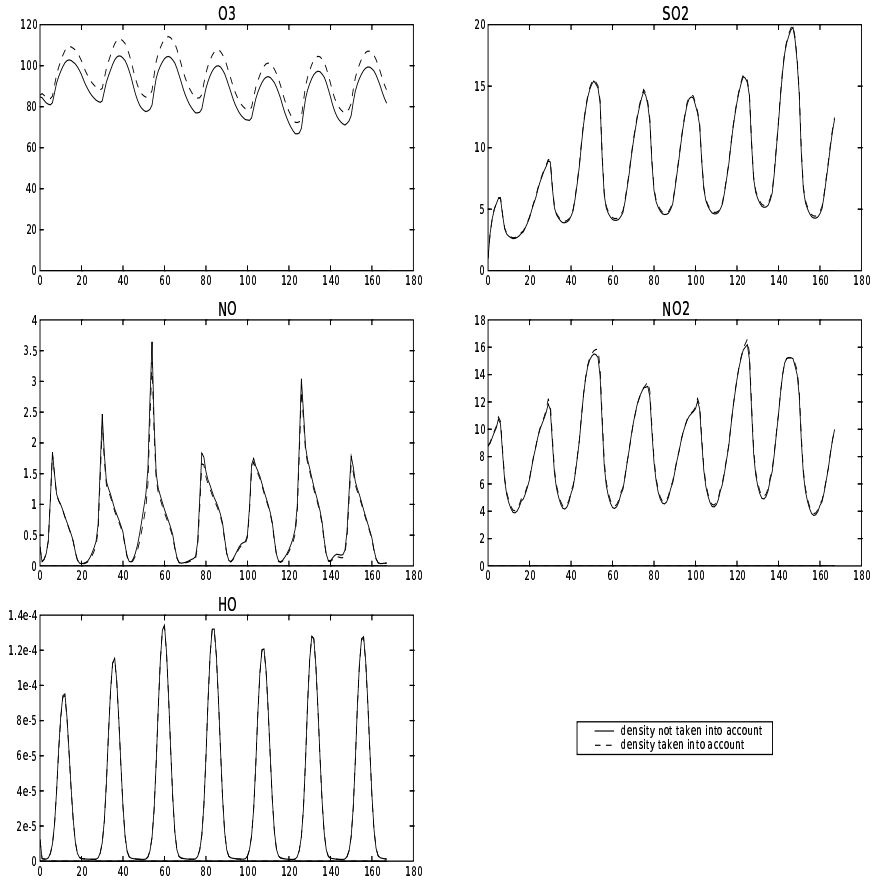

Figure 137: Time evolution of the spatial mean ($\mu g \cdot m^{-3}$) on the ground when air density is taken into account or not taken into account

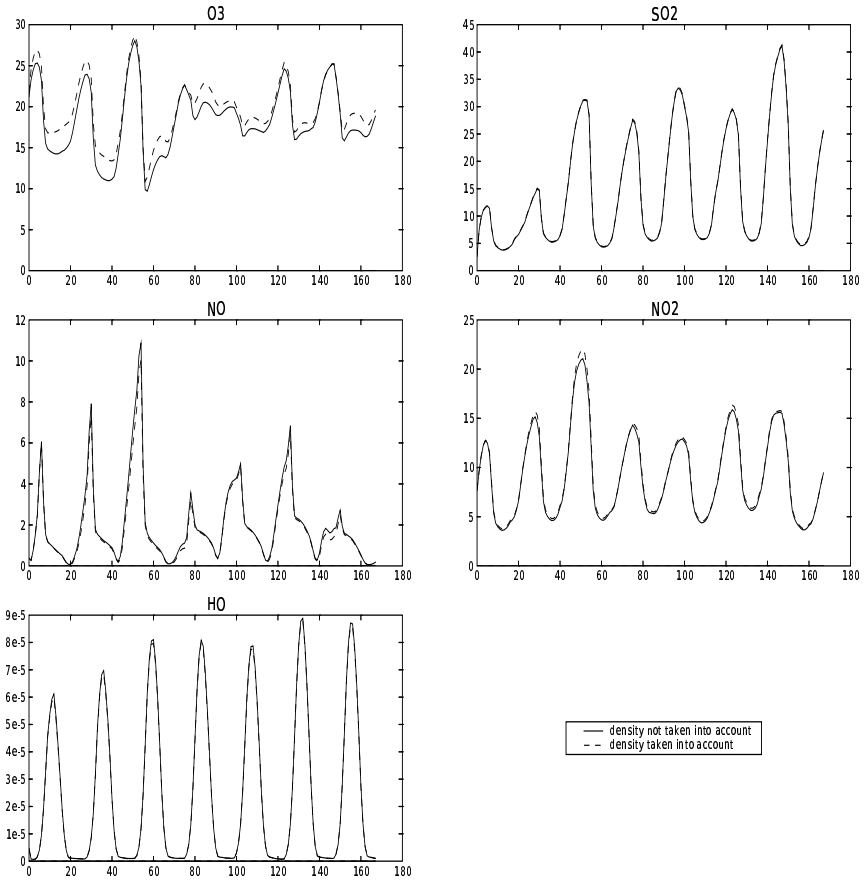

Figure 138: Time evolution of the spatial standard deviation ($\mu g \cdot m^{-3}$) on the ground when air density is taken into account or not taken into account

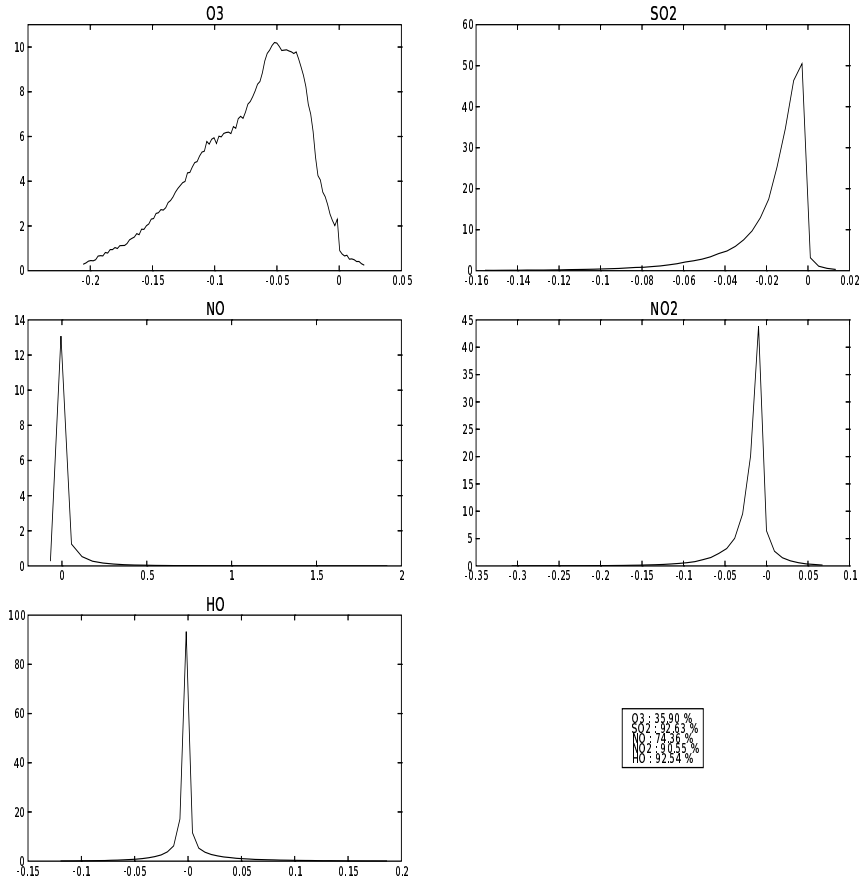

Figure 139: PDF of error between simulations where density is taken into account and where density is not taken into account

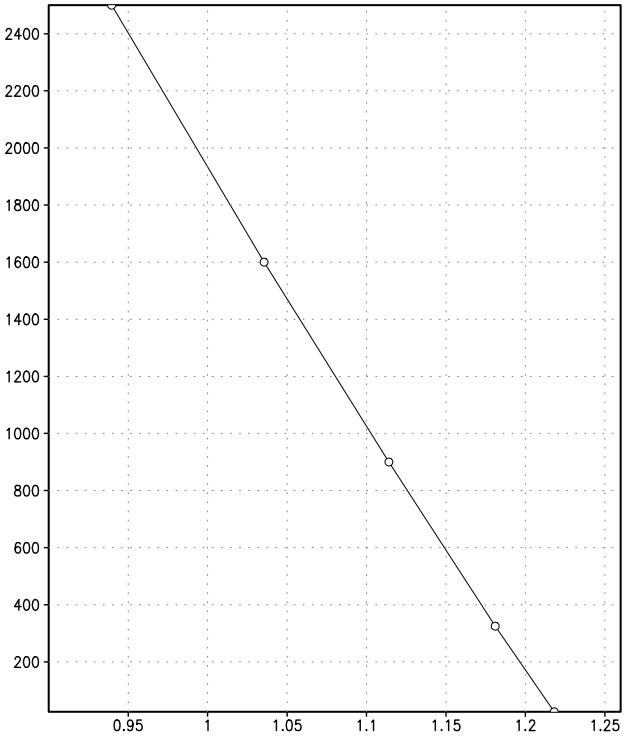

Figure 140: Averaged value of ρ over Europe

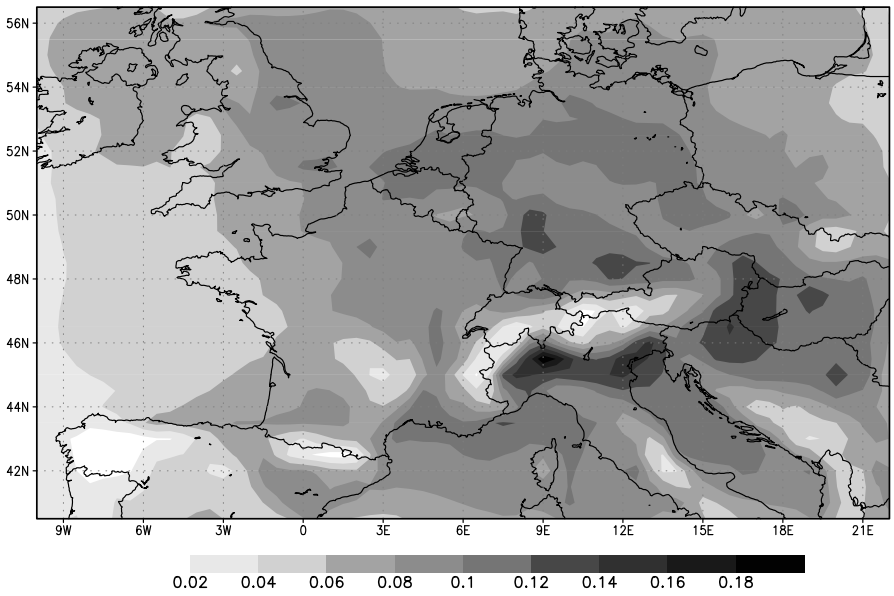

Figure 141: $\frac{mean\,(m_i\ parameterization)\ -\ mean\,(c_i\ parameterization)}{mean\,(c_i\ parameterization)}$ for O3

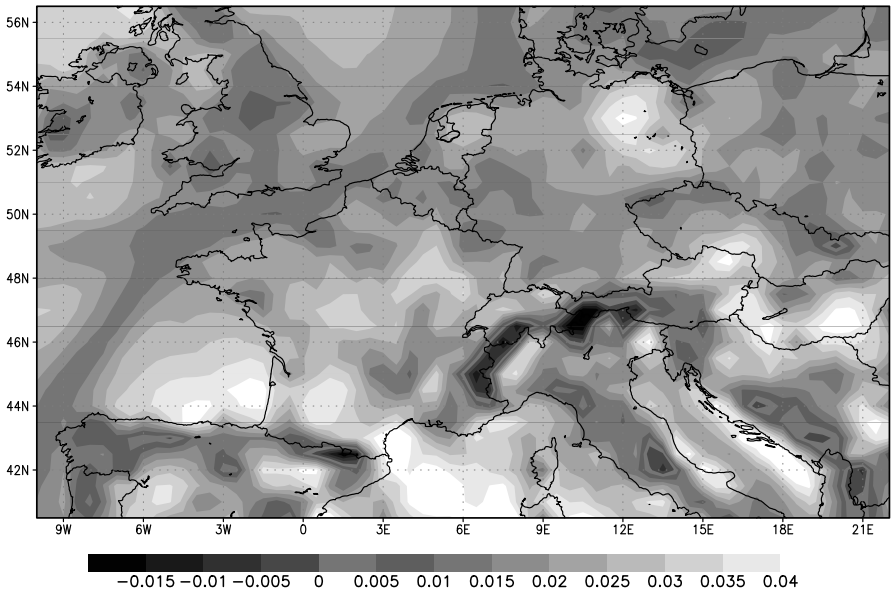

Figure 142: $\frac{mean\,(m_i\ parameterization)\ -\ mean\,(c_i\ parameterization)}{mean\,(c_i\ parameterization)}$ for SO2

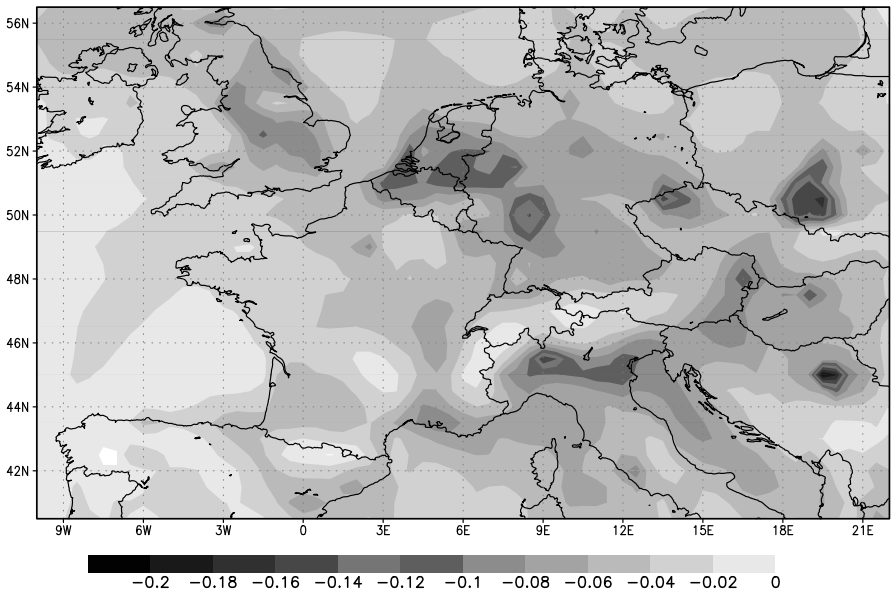

Figure 143: $\frac{mean\,(m_i\ parameterization)\ -\ mean\,(c_i\ parameterization)}{mean\,(c_i\ parameterization)}$ for NO

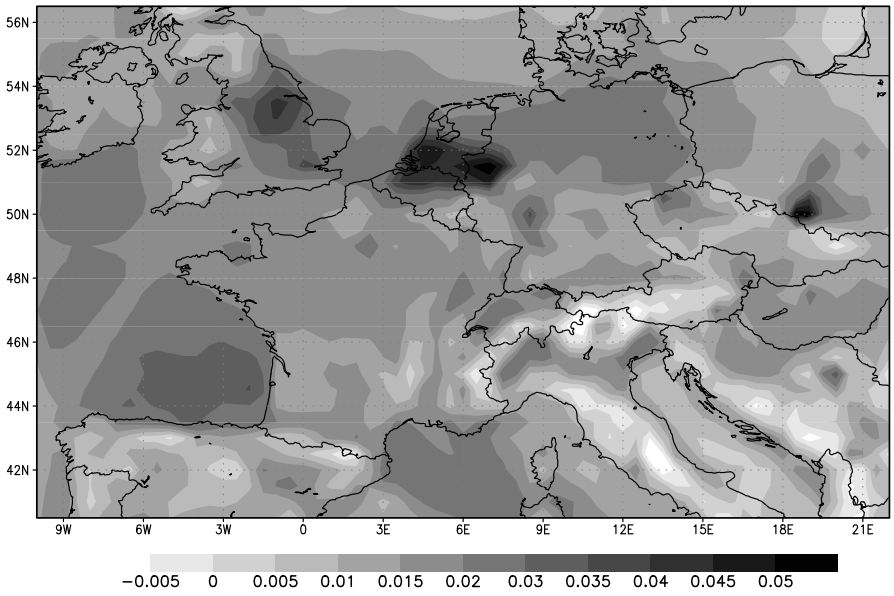

Figure 144: $\frac{mean\,(m_i\ parameterization)\ -\ mean\,(c_i\ parameterization)}{mean\,(c_i\ parameterization)}$ for NO2

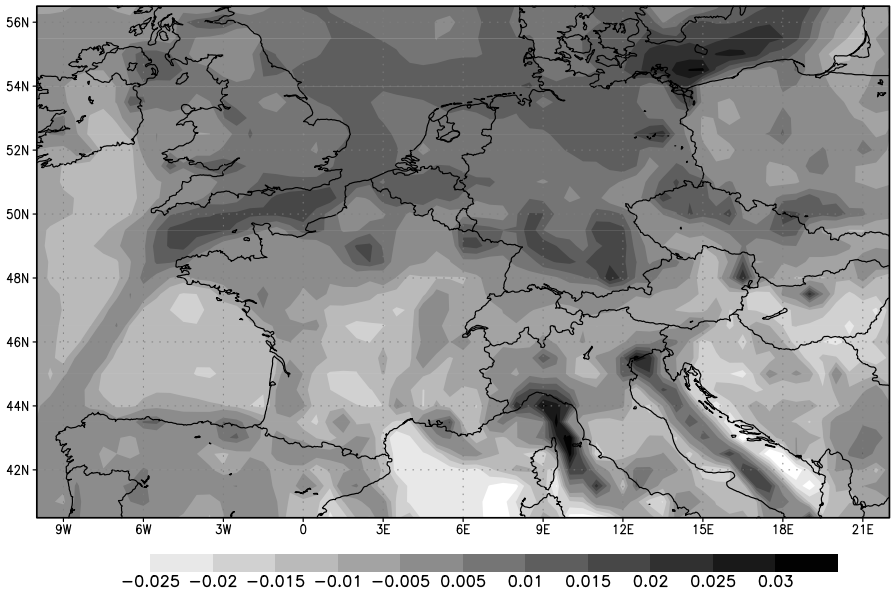

Figure 145: $\frac{mean\,(m_i\ parameterization)\ -\ mean\,(c_i\ parameterization)}{mean\,(c_i\ parameterization)}$ for HO

greater than 5% for NO_2, SO_2, HO and NO. However, as we had seen before on figures 137 and 138, we can see a more important impact on O_3. Indeed, the difference goes to 20% near coasts and reliefs. This was predictable: other species stay near the ground, or are immediately destructed, whereas O_3 is present at all altitudes and is not homogeneous. Figures 146 and 147 confirm that the altitude does make a difference.

6.3 Conclusion

The turbulent diffusion coefficient seems to be the numerical parameter that has the strongest influence on results. The chosen value of 50 000 $m^2 \cdot s^{-1}$ may even be a little too strong. The choice of parameterization for air density is also rather important

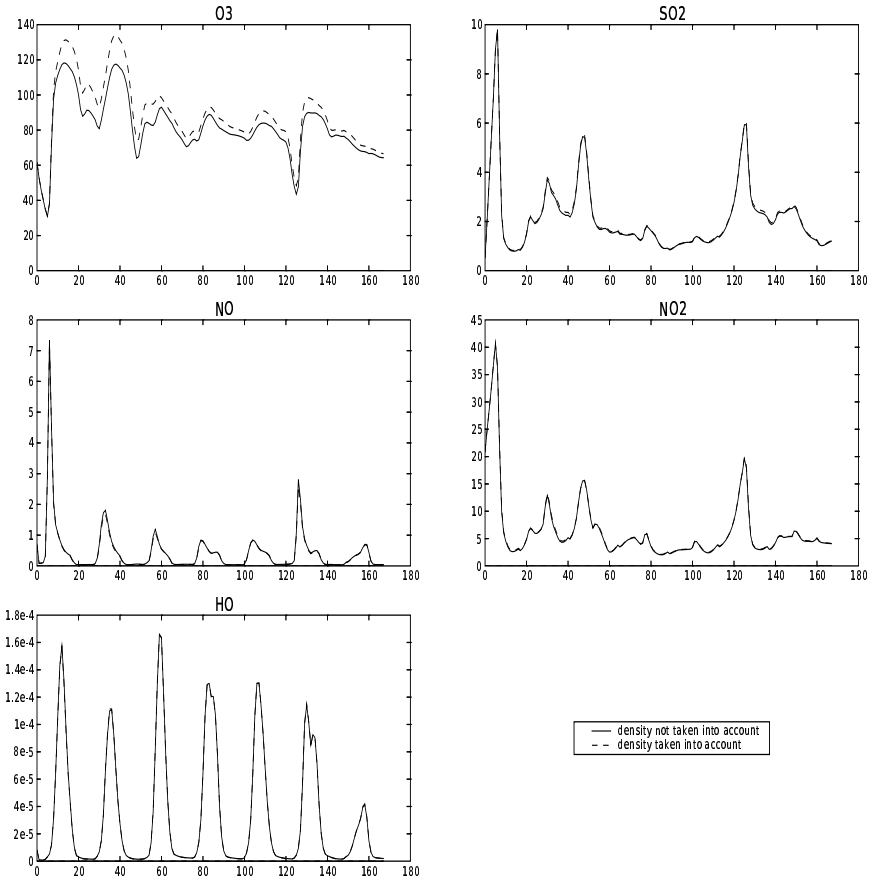

Figure 146: Time evolution of the concentrations ($\mu g \cdot m^{-3}$) over Paris for different parameterizations

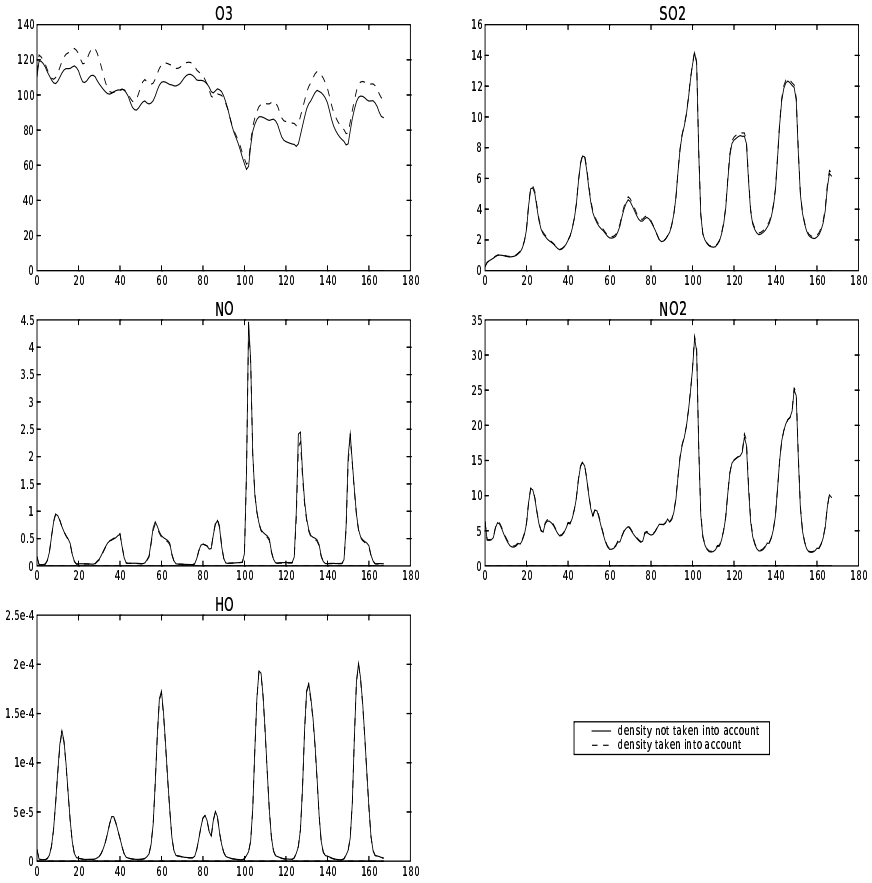

Figure 147: Time evolution of the concentrations ($\mu g \cdot m^{-3}$) over Chamonix for different parameterizations of K_H

Conclusion

We have reviewed in this report the main numerical issues arising in gas-phase Chemistry-Transport Models. The numerical tests have been led in a 3D realistic framework in order to assess the "true" impact of numerical algorithms.

The main conclusions are the following ones:

- As far as splitting methods are concerned, the numerical issues are not so important. However, the sequence of processes does matter, as well as the process in which boundary conditions are taken into account.
- The advection scheme has an impact on the results, besides being determining in terms of CPU.
- The choice of parameterization for air density and the value of K_H are determining.

These results indicate that many species (especially ozone) can be computed without using sophisticated methods. This is, in certain sense, disappointing for an applied mathematician, but this corresponds to our experiments. This has also to be considered in the global framework for all uncertainties: the spread of results related to numerics appears to be much lower than others (input data, physical parameterizations).

A Statistics

Mean

$$\overline{x} = \frac{1}{n}\sum_{i=1}^{n} x_i$$

Standard deviation

$$\sigma_x = \sqrt{\frac{1}{n}\sum_{i=1}^{n}(x_i - \overline{x})^2}$$

Root mean square error

$$\mathrm{RMSE}(x, y) = \sqrt{\frac{1}{n}\sum_{i=1}^{n}(x_i - y_i)^2}$$

Normalized root mean square error

$$\mathrm{NRMSE}(x, y) = \frac{\mathrm{RMSE}(x, y)}{\sigma_x \sigma_y}$$

B Stability function

The scheme is:

$$c_{n+1} = c_n + (3k_1 + k_2)\frac{\Delta t}{2} \tag{49}$$

where

$$\left\{ \begin{array}{lcl} (1-\gamma\Delta t A)k_1 & = & f(t_n, c_n) \\ (1-\gamma\Delta t A)k_2 & = & f(t_{n+1}, c_n + \Delta t k_1) - 2k_1 \end{array} \right. \tag{50}$$

$\gamma = 1+1/\sqrt{2}$ and A denotes an approximation of the Jacobian matrix $A \simeq \partial f/\partial c$.

The stability function $\mathrm{R}(\Delta t k_n)$ is computed with the linearized source term $f(c,t) = -k(t)\cdot c$.

$$\left\{ \begin{array}{lcl} k_1 & = & \frac{F}{1-\gamma\Delta t A} \\ \\ k_2 & = & \frac{\tilde{F}}{1-\gamma\Delta t A} - \frac{2F}{(1-\gamma\Delta t A)^2} \end{array} \right. \tag{51}$$

Since $A = -k_n$ and if we take $\lambda = \Delta t \cdot k_n$, we get:

$$\left\{ \begin{array}{lcl} k_1 & = & \frac{F}{1+\gamma\lambda} \\ \\ k_2 & = & \frac{\tilde{F}(1+\gamma\lambda)-2F}{(1+\gamma\lambda)^2} \end{array} \right. \tag{52}$$

Therefore, c_{n+1} is equal to:

$$\begin{array}{rcl} c_{n+1} & = & c_n + \frac{3\Delta t}{2}\cdot\frac{F}{1+\gamma\lambda} + \frac{\Delta t}{2}\cdot\frac{\tilde{F}}{1+\gamma\lambda} - \frac{\Delta t}{2}\cdot\frac{2F}{(1+\gamma\lambda)^2} \\ & = & c_n - \frac{3\Delta t\, k_n}{2(1+\gamma\lambda)}\, c_n + \frac{\Delta t}{2}\cdot\frac{\tilde{F}}{1+\gamma\lambda} + \frac{\Delta t\, k_n}{(1+\gamma\lambda)^2}\, c_n \end{array} \tag{53}$$

Besides:

$$\begin{array}{rcl} \tilde{F} & = & -k_{n+1}\,(c_n + \Delta t k_1) \\ & = & -k_{n+1}\, c_n - k_{n+1}\Delta t\frac{F}{1+\gamma\lambda} \\ & = & -k_{n+1}\, c_n + k_{n+1}\cdot\frac{\Delta t\cdot k_n}{1+\gamma\lambda} c_n \\ & = & -k_{n+1}\, c_n \cdot \left[\frac{\lambda}{1+\gamma\lambda} - 1\right] \end{array} \tag{54}$$

Hence:

$$c_{n+1} = c_n - \frac{3\Delta t\, k_n}{2(1+\gamma\lambda)}\, c_n + \frac{\Delta t}{2}\cdot\frac{k_{n+1}\, c_n}{1+\gamma\lambda}\left[\frac{\lambda}{1+\gamma\lambda} - 1\right] + \frac{\Delta t\, k_n}{(1+\gamma\lambda)^2}\, c_n$$

$$
\begin{aligned}
&= c_n + \frac{\Delta t\, k_n}{2(1+\gamma\lambda)^2}\, c_n \left\{ -3(1+\gamma\lambda) + 2 + \frac{k_{n+1}}{k_n}\,(1+\gamma\lambda)\, \left[\frac{\lambda - 1 - \gamma\lambda}{1+\gamma\lambda} \right] \right\} \\
&= c_n + \frac{\Delta t\, k_n}{2(1+\gamma\lambda)^2}\, c_n \left\{ -3 - 3\gamma\lambda + 2 + \beta(\lambda - 1 - \gamma\lambda) \right\} \qquad (55)
\end{aligned}
$$

where $\beta = \frac{k_{n+1}}{k_n}$. Therefore, we have:

$$
\begin{aligned}
\frac{c_{n+1}}{c_n} &= 1 + \frac{\lambda}{2(1+\gamma\lambda)^2}\, c_n \left\{ -1 - 3\gamma\lambda + \beta\lambda - \beta - \beta\gamma\lambda \right\} \\
\frac{c_{n+1}}{c_n} &= \frac{1}{2(1+\gamma\lambda)^2} \left[2(1+\gamma\lambda)^2 - \lambda - 3\gamma\lambda^2 + \beta\lambda^2 - \beta\lambda - \beta\gamma\lambda^2 \right] \\
\frac{c_{n+1}}{c_n} &= \frac{\left(2\gamma^2 - (3+\beta)\,\gamma + \beta\right)\lambda^2 + (4\gamma - 1 - \beta)\,\lambda + 2}{2(1+\gamma\lambda)^2} \qquad (56)
\end{aligned}
$$

References

[1] Mark Z. Jacobson. *Fundamentals of atmospheric modeling.* Cambridge University press, Oxford, 1999.

[2] L. Lanser and J.G. Verwer. Analysis of operator splitting for advection-diffusion-reaction problems from air pollution modelling. In *Proceedings 2nd Meeting on Numerical methods for differential equations.* Coimbra, Portugal, February 1998.

[3] G.J. McRae, W.R. Goodin, and J.H. Seinfeld. Numerical solution of the atmospheric diffusion equation for chemically reacting flows. *J.Comp.Phys.*, 45:1–42, 1982.

[4] A. Sandu, J.G. Verwer, J.G. Blom, E.J. Spee, and G.R. Carmichael. Benchmarking stiff ODEs solvers for atmospheric chemistry problems II: Rosenbrock solvers. *Atm. Env.*, 31:3459–3472, 1997.

[5] A. Sandu, J.G. Verwer, M. Van Loon, G. Carmichael, F.A. Potra, D. Dabdub, and J.H. Seinfeld. Benchmarking stiff ODEs solvers for atmospheric chemistry problems I: implicit versus explicit. *Atmos.Environ.*, 31:3151–3166, 1997.

[6] J.H. Seinfeld and S.N. Pandis. *Atmospheric chemistry and Physics.* Wiley-interscience, 1998.

[7] E.J. Spee. *Numerical methods in global transport-chemistry models.* PhD thesis, Univ. Amsterdam, 1998.

[8] B. Sportisse. An analysis of operator splitting techniques in the stiff case. *J. Comp. Phys.*, 161:140–168, 2000.

[9] W.R. Stockwell, F. Kirchner, M. Kuhn, and S. Seefeld. A new mechanism for regional atmospheric chemistry modeling. *J. Geophys. Res.*, 95(D10):16343:16367, 1997.

[10] J.G. Verwer, W.H. Hundsdorfer, and J.G. Blom. Numerical time integration for air pollution models. In *Proceedings of the Conference APMS'98.* ENPC-INRIA, October 26-29 1998.

[11] J.H. Verwer, E.J. Spee, J.G. Blom, and W.H. Hundsdorfer. A second order Rosenbrock method applied to photochemical dispersion problem. *SIAM J. Sc. Comput.*, 20(4):1456–1480, 1999.

[12] Z. Zlatev. *Computer treatment of large air pollution models.* Kluwer Academic Publishers, 1995.

Contents